Recent Research in Physical and Chemical Sciences

Editors

Prof. R.K. Shukla
Dr. Bhuvan Bhasker Srivastava
Dr. Susheel.Kumar Singh

MKSES PUBLICATIONS
LUCKNOW, INDIA

Recent Research in Physical and Chemical Sciences

Prof. R.K. Shukla
Dr. Bhuvan Bhasker Srivastava
Dr. Susheel.Kumar Singh

Recent Research in Physical and Chemical Sciences

Editors

Prof. R. K. Shukla
Professor, Department of Physics,
University of Lucknow, Lucknow, UP India

Dr. Bhuvan Bhasker Srivastava
Associate Professor/HOD
Department of Physics, Shia P. G. College, UP India

Dr. Susheel Kumar Singh
Assistant Professor, Department of Physics,
HLYB PG College, Lucknow, UP India

MKSES Publisher (India)

MKSES Publisher (India)

Publisher Address: Head Office: 1st Floor, Building No-85A, (Nanak Arcade Near Sani Mandir, Parag road, LDA colony, Kanpur Road, Lucknow-226012
Mobile No: +91 9838298016, +91 8299547952 Office Land line No: +91 5223587193
E-mail:mkespublication@gmail.com
Website: www.mksespublications.com

First Published: **September2021**

ISBN: 978-93-91248-18-5

Page No. 1-175

Preface

PhysicalSciences and Chemical Sciences are considered as central science. Currently the scientists in the field Physical Sciences and Chemical Sciences are doing innovative researches. This book presents the premier multidisciplinary forum of the state-of-the-art research, development, and commercial prospective of recent advances inPhysicalSciences and Chemical Sciences. This book will be a useful resource for researchers as well as professionals interested in the highly interdisciplinary field of materials science and engineering.

The present volume is based on the contributions made by various authors on different important topic of "**Recent Research in Physical and Chemical Sciences**" and introduces the subject along the following topics:Medicinal importance of oligosaccharides; Sol-gel Spin Coating method for thin film deposition; Bandgap engineering of the perovskite materials for solar cell applications; Molecular interaction studies of DMSO-Toluene binary mixtures at Different Temperatures by Ultrasonic Technique; An overview of Deep Eutectic Solvents (DESs): An emerging class of green solvents; Preliminary study of 2D-Molybednum Disulphide (MoS_2) using Open Source Quantum Espresso Software; An overview of Computational study of Oligosaccharides; Impact of alky chain length of N-(4-n-Alkyloxybenzalidene) 4′-n-Alkylaniline on dielectric parameters, Kinetic studies of 3-Toluic Acid by Ozonation, Photo-Ozonation, Peroxone and Photoperoxone; Impact of Carbon dioxide on Health and Environmental; Synthesis Characterisation and ^{1}H-NMR Studies of some Bis Polymeric Ligands; Optical analysis of Cadmium doped Selenium-rich Glassy Chalcogenide; Review on Magnetic Nanomaterials Based Metal-Oxide Humidity Sensor; Optical analysis of Cadmium doped Selenium-rich Glassy Chalcogenide and Analysis of Thermoelastic Properties of Materials in the Limit of Infinite Pressure.

We must place on record our sincere gratitude to the authors not only for their effort in preparing the papers for the present volume, but also their patience in waiting to see their work in print. Finally, we are also thankful to our publishers **Mrs. Shweta Singh** M/S MKSES Publishers, Lucknow for taking all the efforts in bringing out this volume in short span time.

Editors

Contents

Chapter No.	Chapter Name	Page No.
1.	Medicinal importance of oligosaccharides *Ratnakar Dutt Shukla, Susheel Kumar Singh and Bhuvan Bhasker Srivastava*	1-12
2.	Sol-gel Spin Coating method for thin film deposition *Nishant Kumar and Anu Katiyar*	13-19
3.	Bandgap engineering of the perovskite materials for solar cell applications *R. K. Shukla, Amrit Kumar Mishra and K.C, Dubey*	20-30
4.	Molecular interaction studies of DMSO-Toluene binary mixtures at Different Temperatures by Ultrasonic Technique *Sunil Dahire*	31-37
5.	An overview of Deep Eutectic Solvents (DESs): An emerging class of green solvents *Byanju Rai and Ratnakar Dutt Shukla*	38-45
6.	Preliminary study of 2D-Molybednum Disulphide (MoS_2) using Open Source Quantum Espresso Software *Ashwini Kumar*	46-50
7.	An overview of Computational study of Oligosaccharides *Arvind Kumar Tripathi and Vikas Tripathi*	51-63
8.	Impact of alky chain length of N-(4-n-Alkyloxybenzalidene) 4′-n-Alkylaniline on dielectric parameters *Ragini Tripathi, Avneesh Mishra, K. N. Singh, P. R. Alapati and Ravindra Dhar*	64-77
9.	Kinetic studies of 3-Toluic Acid by Ozonation, Photo-Ozonation, Peroxone and Photoperoxone *Susmita A. Mandavgane*	78-84

10.	Impact of Carbon dioxide on Health and Environmental *Vikas Tripathi and Arvind Kumar Tripathi*	85-90
11.	Synthesis Characterisation and 1H-NMR Studies of some Bis Polymeric Ligands *Vaishali P. Meshram*	91-100
12.	Ecological and economic considerations of Deep Sea bed Mining Manganese : A Review *Ratna Sarkar*	101-111
13.	Review on Magnetic Nanomaterials Based Metal-Oxide Humidity Sensor *Y. S. Bopche and R. M. Patle*	112-133
14.	Optical analysis of Cadmium doped Selenium-rich Glassy Chalcogenide *Arvind Kumar Verma, R. K. Shukla and Susheel Kumar Singh*	134-141
15.	Analysis of Thermoelastic Properties of Materials in the Limit of Infinite Pressure *A. Dwivedi*	142-151
16.	Quantum chemical calculation s of [(1S, 4R)-4-{2-amino-6-(cyclopropylamino) purin-9-yl} cyclopent-2-en-1-yl] methanol (Abacavir) using Density Functional Theory *Shashi Kumar Gangwar, Susheel Kumar Singh, R.K Shukla and Bhuvan Bhasker Srivastava*	152-159
17.	Dye sensitized solar cells-need of an hour *Priyanka Chawla, Kumari Pooja and Mridula Tripathi*	160-168
18.	Prism based refractometer *Priyanka Srivastava*	169-175

Chapter: 1

Medicinal importance of oligosaccharides

Ratnakar Dutt Shukla[1], Susheel Kumar Singh[2] and [3]Bhuvan Bhasker Srivastava

[1]Department of Chemistry, Pt. DDU Govt. I. College, Bahua, Fatehpur, UP India

[2]Department of Physics, HLYB PG College, Lucknow, UP India

3Department of Physics, Shia P. G. College Lucknow U P India

Email: rdbhuchem09@gmail.com; **susheelsingh489@gmail.com**

Abstract: Oligosaccharides (carbohydrates) are composed from 2 to 10 simple units of monosaccharides. Oligosaccharides possess many crucial functions in biological systems such as cell binding and cell recognition. The biological roles of oligosaccharides demonstrate to span the spectrum from those that are trivial, to those that are necessary for the growth, development, function or survival of an organism. Some general principles have been emerged. First, it is not easy to predict a priori the functions a given oligosaccharide on a provided glycoconjugate might be mediating, or their relative importance to the organism. Second, the sequence of same oligosaccharide may facilitate various functions at different locations within the same organism. Third, the more specific and promising biological functions of oligosaccharides are commonly mediated by unusual presentations of common-terminal sequences, unusual oligosaccharide sequences, or by further changes of the sugars themselves.

Keyword: Oligosaccharides, cell binding and cell recognition, glycoconjugate

Introduction:

Complex carbohydrates are regarded as main source of energy for the living body. Carbohydratessupply the continuous fuel to body requirements for daily living activities, exercise, and even rest. Complex carbohydrates are usually single units (monosaccharides), which are connectedtogether. The oligosaccharides possess two to ten simple units of monosaccharides. Polysaccharides can beconsidered as polymer, and possess hundreds and thousands of monosaccharide units as monomer. Complex carbohydrates contain long sustained energy. The different types of carbohydrates can be classified on the basis of number of sugar units (monomers). They are mainly categorized into three groups and nicely depicted in figure 1.

Carbohydrates play crucial roles in biological system as they areassociatedtonumerous important activitiesregarding the immune system.[1]Moreover, they are often biocompatible, safe and well tolerated, which are intrinsic, favourable properties that make carbohydrate structures attractive targets for the development of vaccine adjuvants and immunomodulators. Considering the aforementioned properties, carbohydrates can be exploited by the scientificcommunity of chemistry.[2]Carbohydrates exhibitseveraladvantageouscharacteristics that make them promising adjuvantcandidates, namely, high biocompatibility and tolerability and a strong safety profile.[3]A variety of naturalcarbohydrate structures, especially MPLA and QS-21, have been clinically assessed as adjuvants and are part of licensed Adjuvant Systems (AS) in human vaccines against HPV (AS04), herpes zoster and malaria (AS01).

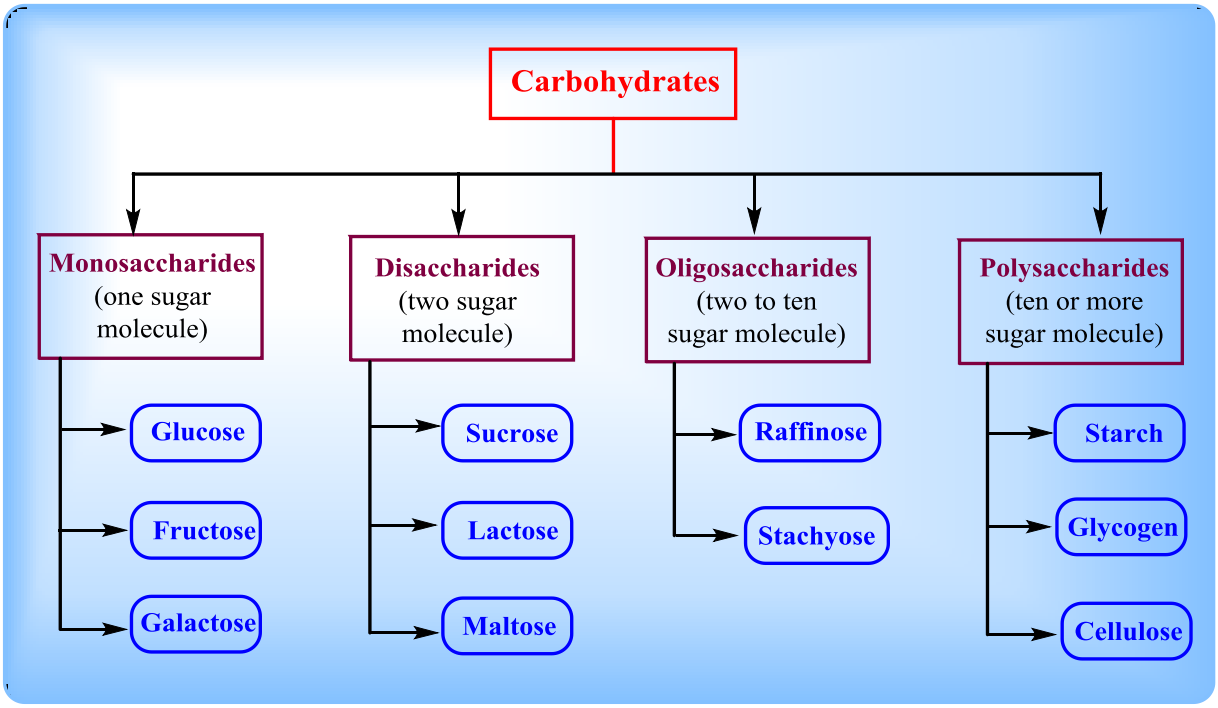

Figure 1.The general classification of carbohydrates

Chemical synthesis is emerging as a powerful approach on this front, offering practical access to homogeneous carbohydrate compounds for adjuvant development, as well as enabling further SAR studies towards improved synthetic analogues. Recently Fernández-Tejada and his group reported the recent advances in natural and synthetic carbohydrate-based adjuvants, including current knowledge of their immunopotentiation mechanisms, in addition to selected

applications in the field of vaccines against infectious diseases and cancer.[4]It is expected that this progress will make it possible for both chemists and immunologists to rationally design and develop novel, carbohydrate-based adjuvants with enhanced efficacy and reduced toxicity for further clinical advancement in human vaccines.

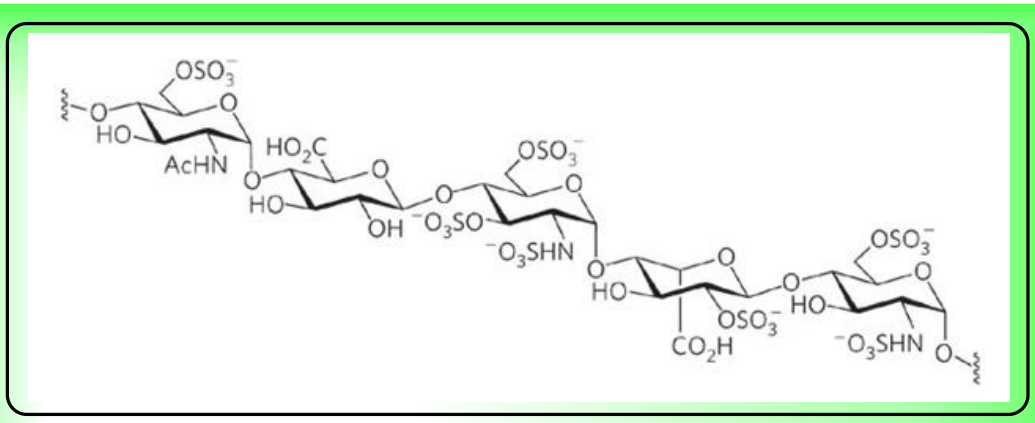

(a) A pentasaccharide sequence of heparin. This sequence is responsible for binding to antithrombin III.

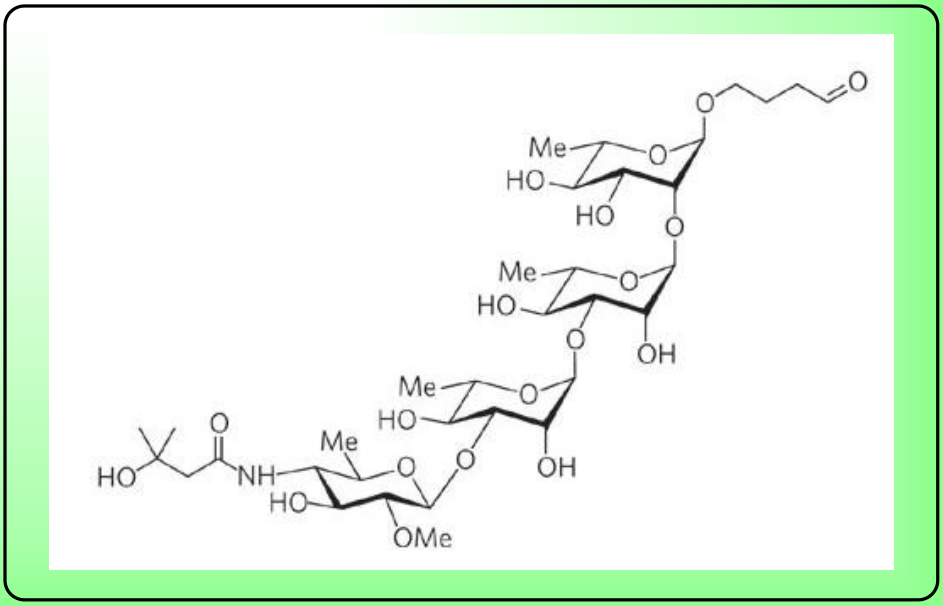

(b) Synthetic spore surface tetrasaccharide of B. anthracis. This molecule was used for the generation of anticarbohydrate antibodies to detect anthrax spores and is currently being used in vaccine development.

Figure 2: Carbohydrates employed in thedevelopmentof medicine and for vaccine

The biological roles of oligosaccharides have not been properly studied in the past in comparison to other biopolymers e.g. proteins and nucleic acids. Although for many years it was known that the antigenic determinants of the ABO (H) blood group and the related Lewis blood groups are carbohydrate structures. Carbohydrate modifications of proteins and lipids are important processes that modulate the structures and functions of these biomolecules and affect intercellular recognition in infection, cancer, and immune response. Most recent efforts in the field are to develop new tools for use to understand the molecular-level carbohydrate recognition and to enable the carbohydrate-based drug discovery process. Agreat deal has been learnt in recent years aboutthe biological role of oligosaccharides, and this has led to anew field named glycobiology.[5-6]Understanding their biological significance and exploring their therapeutic value have driven the advancement of synthetic carbohydrate chemistry, glycobiology, and chemical glycobiology.[7]

Prevalent role of carbohydrates has been provided the in a broad spectrum of biological processes it may seem surprising that there are few carbohydrate-based therapeutics and diagnostics on the market. In addition to monosaccharide-inspired drugs such as the influenza virus treatment Tamiflu[8-9] (oseltamivir phosphate; Roche) two blockbuster drugs, acarbose (Precose, Glucobay; Bayer) and heparin, stand out. Both oligosaccharides were derived by isolation and reached the clinic before a detailed structure-activity relationship had been established. In addition, aminoglycosides naturally occurring pseudo-oligosaccharides have been used clinically to treat infectious diseases induced by a variety of Gram-negative bacteria.[10]The antibiotic activity of aminoglycosides is due to their inhibition of protein synthesis, which results from their binding to bacterial ribosomes.

Heparin

The oldest carbohydrate-based drug is isolated from animal organs and has been used clinically as an antithrombotic agent since the 1940s. Heparin activates the serine protease inhibitor antithrombin III, which blocks thrombin and factor Xa in the coagulation cascade.[11] This drug is a highly heterogeneous mixture of polysaccharides and is associated with severe side effects, including heparin-induced thrombocytopenia, bleeding and allergic reactions. Chemically or enzymatically fragmented heparins (low-molecular-weight heparins, LMWHs) are also

heterogeneous, but are more bioavailable, with a longer half-life, a more predictable anticoagulant activity and fewer side effects *in vivo*.

After the specific pentasaccharide responsible for the anticoagulant property was identified in the early 1980s (Figure 2), a herculean effort lasting more than 10 years was begun to establish a structure-function relationship using synthetic oligosaccharides.[12] As a result of this drug-development effort, a synthetic pentasaccharide known as Arixtra (fondaparinux sodium; GlaxoSmithKline) has been available since 2002.[13] However, Arixtra does have some clinical shortcomings, such as an exceedingly long half-life *in vivo*and little to no dose-dependent activity in certain indications.[14]Thus, LMWHs still have the highest market share of all antithrombotics, and the need for additional synthetic heparin molecules with specific activities persists.

Recent advances in heparin sequencing,[15] heparin synthesis[16-18] andheparin microarray technology[19] have provided the tools to identifyspecific sequences or sequence families that interact with proteins such as chemokines. The chemical synthesis of a broad range of heparin analogues should allow researchers to study the molecular mechanism of angiogenesis and to modulate wound healing and other medically relevant processes.

Acarbose

Carbohydrates such as starch and sucrose are principal components of food, and have to be enzymatically broken down in the intestinal tract. Acarbose,[20] a pseudo-oligosaccharide of microbial origin, is produced by fermentation. This α-glucosidase and α-amylase inhibitor interfereswith and regulates intestinal carbohydrate digestion, controls the rate ofabsorption of monosaccharides and influences the intermediary carbohydratemetabolism. It is used to treat type 2 diabetes.

Carbohydrate-based vaccines

Vaccination is one of the most important scientific inventions in the control and eradication of microbial infections. Vaccines are considered as one of the most cost-effective interventions to prevent morbidity and mortality from infectious diseases.[21] Over the last 50 years, vaccines have greatly contributed to improving human health, by controlling, and in some cases eradicating,

many devastating viral (e.g. smallpox, measles, polio) and bacterial (e.g. diphtheria, tetanus) infectious diseases.The cell surfaces of bacteria, parasites and viruses exhibit oligosaccharides that are often distinct from those of their hosts. Specific types of glycoconjugate are often more highly expressed on the surface of tumours than on normal cells.[22]Such cell-surface carbohydrate markers are the basis for carbohydrate-based detection systems and vaccines. An immune response against the carbohydrate antigens that results in the death of target cells is required for a carbohydrate-based vaccine. Suchvaccines have been widely used against a host of diseases for several decades.[23]The carbohydrate antigens for antibacterial vaccines were isolated from biological sources. Recently, intense efforts focused on the use of defined carbohydrate antigens that are synthesized rather than isolated. A carbohydrate-based approach has also been pursued for anticancer vaccine candidates.[24-25] However, one of the early carbohydrate-based anticancer vaccine candidates recently failed in a Phase III clinical trial.

Antibacterial vaccines

Synthetic advances made possible chemical assembly of complex oligosaccharide fragments of polysaccharide domains on the surface of human pathogenic bacteria. These oligosaccharides may be recognized by antibodies raised against high molecular weight, native, polysaccharides. In addition to their antigenicity, synthetic oligosaccharides can also function as haptens in their protein conjugates that can elicit not only oligo- but also polysaccharide-specific IgG antibodies in animal models and in humans. A major milestone in the development of new generation vaccines was the demonstration that protein conjugates of synthetic fragments of the capsular polysaccharide of Haemophilus influenzae type b are as efficacious in preventing childhood meningitis and other diseases as is the corresponding licensed commercial vaccine containing the bacterial polysaccharide. The lessons learnt in this and other endeavors described herein are manifold. For example, they teach us about the significance of the oligosaccharide epitope size, the number of their copies per protein in the conjugate, the possible effect of the spacer on anti-saccharide immune response, and the proper choice of the carrier protein combined with the selection of the animal model. The H. influenzae b story also teaches us that that the synthetic approach can be commercially viable.[26]

A synthetic carbohydrate conjugate vaccine against *Haemophilus influenzae* type b is now commercially available as Quimi-Hib (made from a tiny fragment of the bacteria's sugar-coat attached to a protein). It is a conjugate of a polyribosylribitol phosphate oligosaccharide and a

carrier protein. Introduction of the conjugate Hib vaccine has reduced carriage rates of the bacteria (Figure 3).[27]

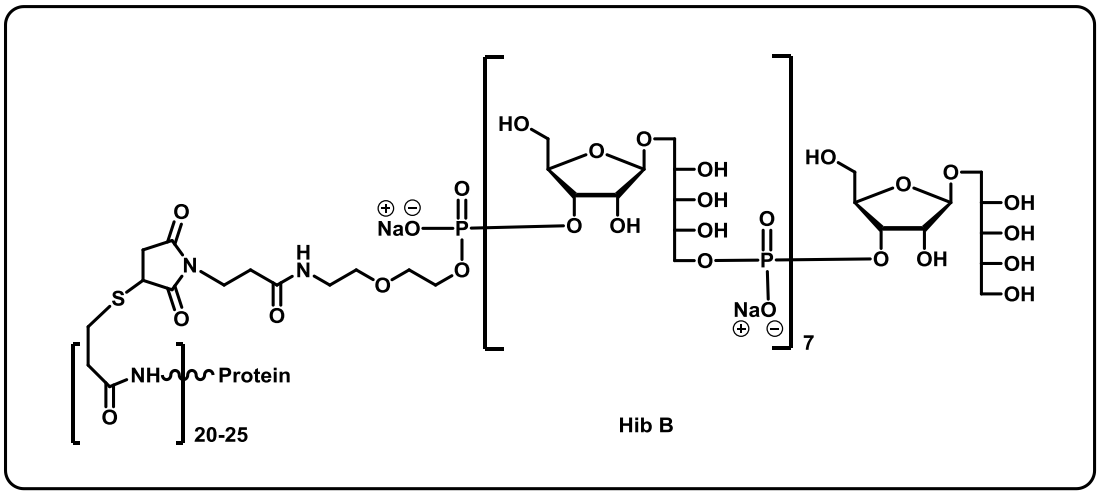

Figure 3: Structure of Quimi-Hib, the vaccine against meningitis.

A tetrasaccharide has been discovered on the surface of spores of the biowarfare agent *Bacillus anthracis*.[28] Once the durable form of the pathogen has been inhaled it will kill most victims if treatment is not commenced immediately. Synthesis of a species-specific tetrasaccharide antigen[29-30] allowed the production of antibodies that specifically recognize B. anthracis in the presence of the closely related opportunistichuman pathogen *Bacillus cereus*.[31] Challenge experiments to create a conjugate vaccine against anthrax are ongoing.

Antiparasite vaccines

Like bacteria, many parasites have unique glycoconjugates on their surfaces. The specific carbohydrates may serve as a starting point for the creation of conjugate vaccines, but efforts towards this goal have beenhampered by the fact that the parasites are very difficult to culture and because glycoconjugates cannot be obtained in pure form or sufficient quantity by isolation.[32]

Malaria

Plasmodium falciparum is the most pathogenic of the single-celled parasites of the genus Plasmodium that are responsible for malaria. Malaria infects 5-10% of humans worldwide and kills more than 2 million people each year. Infected mosquitoes transmit the parasite, which leads to the common symptoms of chills and fever. Drug resistance is a growing problem at a time when there is still no effective vaccine. *P. falciparum* expresses a large amount of GPI on

its cell surface.[33]This glycolipid triggers an inflammatory cascade that is responsible for much of malaria's morbidity and mortality. When a protein conjugate of a synthetic hexasaccharide GPI malaria toxin was administered to mice before infection, this resulted in a highly reduced mortality rate of only 10–20%, compared with 100% without vaccination.[34] Cross-reactivity of the antibodies with human GPI structures was not observed owing to the differences between human and *P. falciparum* GPI. Immunization of mice did not alter the infection rate or overall parasitaemia, indicating that the antibody against the GPI neutralized toxicity without killing the parasites.

Preclinical studies involving protein conjugates of synthetic GPI antigens are currently underway. To support such vaccine development efforts, methods for the large-scale synthesis of oligosaccharide antigens have been developed by taking advantage of the latest advances in carbohydrate synthesis technology. Very small amounts of synthetic antigen (10–9–10–7 g per person) are required, and the production of several kilograms of antigen per year will suffice.

Leishmaniasis

Leishmaniasis, which is caused by another protozoan parasite, is transmitted by sandflies and affects more than 12 million people worldwide. *Leishmania* resides in macrophages, making them difficult to treat. In a search for a potent vaccine, the lipophosphoglycans (LPGs) that are ubiquitous on the cell surfaces of the parasites and are composed of a GPI anchor, a repeating phosphorylated disaccharide and different cap oligosaccharides became a target. The cap tetrasaccharide has been the focus of efforts towards a conjugate vaccine based on a synthetic antigen.

The branched tetrasaccharide was assembled by automated solidphase synthesis[35] and conjugated to a virosomal particle to enhance immunogenicity. These highly immunogenic conjugates yielded antibodies that selectively recognize parasite-infected livers.[36] Challenge studies in an animal model are currently underway.

Recent advances and future development

In last decades, the lack of tools for studying glycobiology prevented biologists and medical researchers from addressing research problems that involve carbohydrates. During the past decade, sequencing and synthesis technologies that are commonly used to study nucleic acids and proteins have become available for glycomics as well. Now, carbohydrate sequencing of glycoconjugates is often possible even though sample preparation is complicated by

carbohydrate micro heterogeneity and the absence of amplification procedures. Automated solid-phase synthesis, improved methods for solution-phase oligosaccharide assembly, enzymatic methods and the use of engineered cells have complemented each other, allowing oligosaccharide synthesis to take a big step forward by granting access to different classes of glycoconjugate. In turn, these methods have helped procure oligosaccharides and their non-natural analogues for the creation of high-throughput screening methods such as carbohydrate arrays. The identification of specific oligosaccharides, by sequencing followed by comparison with synthetic oligosaccharides, has yielded insight into the interactions of carbohydrates and proteins. Oligosaccharide involvement at key positions of signalling pathways is beginning to emerge and a molecular understanding of carbohydrate binding to proteins is evolving. Detailed structural studies-including studies of protein-carbohydrateinteractions-using X-ray crystallography will become commonplace in the near future. Further improvements in the methods by which oligosaccharides are sequenced and synthesized will be needed to make their routine use possible for non-specialists.

A better understanding of the biological roles of carbohydrates and improved sequencing and synthesis techniques are beginning to influence the design of diagnostic and therapeutic approaches. Carbohydrate arrays help to define new disease markers by screening the sera of patients. Bacterial and viral detection and typing can be achieved using carbohydrate microarrays. Synthetic access to oligosaccharides of infectious agents that are hard to culture and isolate (for example, *B. anthracis* and *P. falciparum*) facilitates antibody production for specific detection of these pathogens. These anti-carbohydrate antibodies may become important for passive immunization. The first conjugate vaccine candidates containing synthetic oligosaccharide antigens arereaching preclinical and clinical trials against bacterial (for example, Hib), viral (for instance, HIV) and parasitic (for example, malaria and leishmaniasis) infections. The trend to produce defined vaccine antigens using chemical and enzymatic methods, as well as engineered cells, is likely to increase, and synthetic vaccines are expected to complement already existing vaccines containing purified polysaccharides.

Conclusion

As our understanding of carbohydrate involvement in signaling cascades in particular of those that involve glycosaminoglycans expands, carbohydrate-mediated processes will become the target of drug-development efforts using small organic molecules. Glycomics has just gone

beyond the initial proof-of-principle studies for diagnostics and therapeutic candidates. Improved tools and a better molecular understanding should convince those biologists and medical researchers who previously avoided carbohydrates to address questions involving this class of molecule. The excitement of glycomics is just beginning, with many discoveries to be made and applications to be developed.

Present chapter covers the basic concept as well as classification of carbohydrates. We have covered the fundamental understanding ofmedicinal importance of oligosaccharides. In addition, we have also discussed carbohydrates/oligosaccharide based vaccines, one of the most successful tools of medical sciences.

References

1. Y. van Kooyk and G. A. Rabinovich, *Nat. Immunol*.,2008, **9**, 593-601.
2. A.Fernández-Tejada, F. J. Cañadaand J. JiménezBarbero, *ChemMedChem*., 2015, **10**, 1291-1295.
3. N. Petrovsky and P. D. Cooper, *Expert Rev. Vaccines*,2011, **10**, 523-537.
4. C.Pifferi,R.Fuentes and A. Fernández-Tejada *Nature Reviews Chemistry*, 2021, **5**, 197-216.
5. T. Feizi, *Nature*, 1985, **314**, 53-57.
6. S. Hakomori, *Ann. Rev. Biochem*., 1981, **50**, 733-764.
7. X.Li, T.Lowary, P.-A.Driguez, N. L. Pohl andJ. Zhu, *J. Org. Chem*.,2020, **85**, 24, 15770-15772.
8. E. De Clercq, *Nature Rev. Drug Discov*.,2006, **5**, 1015-1025.
9. V. Farina and J. D. Brown, *Angew. Chem. Int. Ed*.,2006, **45**, 7330-7334.
10. H. Weizman and Y. Thor, In Carbohydrate-Based Drug Discovery (ed. C.-H.Wong) 661-684 (Wiley-VCH, Weinheim, 2003).
11. I. Capilaand R. J. Linhardt, *Angew. Chem. Int. Ed*.,2002, **41**, 390-412.
12. M.Petitou, B. Casuand U. Lindahl,*Biochimie*,2003, **85**, 83-89.
13. M. Petitou and C. A. A. van Boeckel, *Angew. Chem. Int. Ed*.,2004, **43**, 3118-3133.
14. P. L. F. Giangrande, *Int. J. Clin. Pract*.,2002, **56**, 615-617.
15. L. Chi, E. M Munoz, H. S. Choi, Y. W. Ha, Y. S. Kim, T. Toida and R. J Linhardt. *Carbohydr. Res*.,2006, **341**, 864-869.
16. J. D. C. Codée,B. Stubba,M. Schiattarella,H. S. Overkleeft,C. A. A. van Boeckel,J. H. van Boomand G. A. van der Marel, *J. Am. Chem. Soc*.,2005, **127**, 3767-3773.
17. J.-L. de Paz, et al. *ChemBioChem*.,2001, **2**, 673-685.
18. J.-C. Lee, et al. *J. Am. Chem. Soc*.,2004, **126**, 476-477.
19. J. L.de Paz, C. Noti and P. H. Seeberger, *J. Am. Chem. Soc*.,2006, **128**, 2766-2767.
20. E. Truscheit, et al. *Angew. Chem. Int. Ed. Engl*.,1981, **20**, 744-761.
21. A. J.Pollard and E. M. Bijker*Nature Reviews Immunology*,2021, **21**, 83-100.
22. S. Hakomori, *Adv. Exp. Med. Biol*.,2001, **491**, 369-402.
23. DGoldblatt,*J. Med. Microbiol*.,1998, **47**, 563-567.
24. S. J.Danishefsky and J. R. Allen, *Angew. Chem. Int. Ed*., 2000, **39**, 836-863.
25. S. F.Slovin, S. J.Keding and G. Ragupathi, *Immunol. Cell Biol*.,2005, **83**, 418-428

26. V. Pozsgay, *Current Topics in Medicinal Chemistry*, 2008, **8**, 126-140.
27. V.Verez-Bencomo, V.Fernández-Santana, E.Hardy, M. E.Toledo, M. C.Rodríguez, L.Heynngnezz, A.Rodriguez, A.Baly, L.Herrera, M.Izquierdo, A.Villar, Y.Valdés, K.Cosme, M. L.Deler, M.Montane, E.Garcia, A.Ramos, A.Aguilar, E.Medina, G.Toraño, I.Sosa, I.Hernandez, R.Martínez, A.Muzachio, A.Carmenates, L.Costa, F.Cardoso, C.Campa,M.Diaz andR. Roy, *Science*, 2004, **305**, 522-525.
28. J. M. Daubenspeck, et al. *J. Biol. Chem*., 2004, **279**, 30945-30953.
29. D. B.Werz and P. H. Seeberger, *Angew. Chem. Int. Ed*., 2005, **44**, 6315-6318.
30. R.Adamo, R.Saksena and P. Kováč, *Carbohydr. Res.*, 2005, **340**, 2579-2582.
31. M. Tamborrini, et al. *Angew. Chem. Int. Ed*.,2006, **45**, 6581-6582.
32. J. A.Jaurigue and P. H. Seeberger, *Front. Cell. Infect. Microbiol*., 2017, **7**, 248.
33. S.Berhe, L.Schofield, R. T.Schwarz and P. Gerold, *Mol. Biochem. Parasitol*., 1999, **103**, 273-278.
34. L. Schofield, et al. *Nature*, 2002, **418**, 785-789.
35. M. C.Hewitt and P. H. Seeberger, *Org. Lett*.,2001, **3**, 3699-3702.
36. X. Liu, et al. *ACS Chem. Biol*.,2006, **1**, 161-164.

Chapter: 2

Sol-gel Spin Coating method for thin film deposition

Nishant Kumar[1*] and Anu Katiyar[2]

[1]Department of Physics, School of Science,

Maharishi University of Information Technology, Lucknow, UP, India

[2]Department of Physics, University of Lucknow, Lucknow, UP, India

[*]E-mail:nishant1986lu@gmail.com

Any sample with one of its dimensions very much less than other two may be called a thin film [1]. They are thin layers of material ranging from fractions of nanometers to several micrometers. Thin films are benefiting the electronic semiconductor devices, photonic devices and optical coatings etc. Thin film properties are strongly dependent on the method of deposition, substrate material, the rate and angle of deposition and the ambient atmosphere. The specific applications demand specific film properties such as high optical transmission/reflection, adhesion, hardness, porosity, high resistivity or conductivity, chemical inertness towards corrosive environments and stability with respect to temperature, stoichiometry and orientation in single and polycrystalline films. Amorphous films are also found to be useful e.g. in optical sensors [2-4], lasing materials [5] etc.

Deposition of thin films

Obtaining a thin film of any material on a substrate surface with proper adherence is thin film deposition. Deposition techniques can be broadly classified as physical and chemical deposition methods.

The deposition process of a film can be divided into three basic phases:

1. Preparation of the film forming particles (atoms, molecules, cluster)
2. Transport of the particles from the source to the substrate
3. Adsorption of the particles on the substrate and film growth

Physical Deposition Methods

Physical deposition methods require maintenance of vacuum of 10^{-6} Torr or more. They include several methods such as sputtering, thermal evaporation, pulsed laser deposition, cathodic arc

deposition etc. Besides these, other methods like reactive sputtering, molecular beam epitaxy, atomic layer deposition, liquid phase epitaxy etc. are also used for obtaining improved quality of films by precisely controlling the deposition parameters. Rate of deposition, substrate temperature, ambient conditions, residual gas pressure in the system, purity of the material to be deposited, inhomogeneity in the films, structural or compositional varieties of the films in localized or wider areas determine the electrical, optical, magnetic and surface properties of the deposited films [6].

Chemical Deposition Methods

Chemical deposition methods include electroplating, chemical vapour deposition, plasma enhanced chemical vapour deposition, organometallic solutions etc. A non-vacuum technique, for producing thin optical films, is the use of organometallic solutions that are applied to a substrate's surface either by dipping or by spinning or by spraying. The film is then dried and baked in the furnace. Thermal decomposition takes place and the film is converted to pure oxide while the organic constituents evaporate. Thickness control is achieved by adjusting the temperature, viscosity and other properties of the solution. This technique besides being continuously used in materials related research has been used successfully to coat high power laser optical components with antireflection design that have extremely high damage thresholds. In the present chapter we will discuss sol-gel spin coating using organometallic solutions. The thickness of the films obtained from sol-gel spin coating; lie in the range of few hundreds of nanometers. There are several methods for producing ZnO based films e.g. chemical vapor deposition, spray pyrolysis, dip coating, sol-gel, etc. Out of these methods sol-gel is simpler besides producing good quality films.

Sol-gel process

In chemical deposition process, sol-gel process is widely used for the deposition of thin films, nanostructures, nanorods etc. The sol-gel preparation of any metal oxide involves combining reactants and the subsequent solidification of the resultant solution into an amorphous oxide gel [7]. The porous oxide is then heated to give densified glasses and polycrystalline solids [8]. Incorporation of dopant and formation of composites is easy [9]. The sol-gel method is an alternative to vacuum deposition techniques. Use of solution based process to form metal oxide semiconductor films for optoelectronic and microelectronics devices may improve the mass

production throughput and reduce cost, since it enables maskless processes including micro contact printing, inkjet printing, and roll printing technology etc. [10].

Sol-gel process consists essentially of three steps [11]-

a. Formation of low viscosity solutions of suitable precursors i.e. metal derivatives (organic/inorganic) which could finally yield the oxides or metal oxides themselves. Low viscosity ensures homogenation.

b. Formation of a uniform sol and causing it to gel to endow chemical homogeneity on the ceramic product during desiccation.

c. Shaping during or after gelation into the final form fibers, surface coating etc. before annealing.

The temperature, pH of the medium and anions/complexing agents present in the solution are the main factors [12] affecting the sol-gel process. The sol-gel process is used in developing thin film transistors [13,14], excitonic devices working at high temperatures [15], antireflection coatings, solar reflecting glass, transparent conducting films [16], magnetic films [17], protective coatings, films for sensors [4] etc.

Sol and precursors

The starting chemicals are called ‘precursors’ which are compounds of relevant components acting as solutes in sol-gel process [18] and they should be able to form reactive inorganic monomers or oligomers. Precursors should be soluble in the reaction media and should be reactive enough to participate in the gel forming process. The reactivity of precursor depends on its chemical nature and applied reaction conditions.

In the sol-gel method the metal oxides or metal hydroxides generally remain in the solution rendering it directly coatable on the substrates. The thickness of the film can be adjusted by changing the concentration or viscosity of the solution. When metal is not available in a soluble form, its organic compound can be taken as a precursor in a suitable solvent and then is made to undergo slow and controlled hydrolysis till it provides a metal-oxygen-metal network in a sol state maintaining most of the time the solubility and transparency of the solution.

In case of metal oxide precursors, the product can be easily freed [19] from the carbonaceous residue. Alkoxides [11] of group I and II metals are non-volatile solids and often depict low solubility in organic solvents. As an alternative [11], metal salts - which are soluble in

organic solvents and can be converted easily to the oxide by thermal or oxidative decomposition are used.

Gelation

The transformation of fluid sols to solidified gel [20] depends on the rheology of the sols [6]. Gelation reduces the distance between the colloidal particles and bonds are formed. The transformation [21] of the solution into a semi-rigid wet gel can be done by

a. by water evaporation or extraction using tray drying, spray drying or dispersion in an immiscible fluid.
b. by removal or neutralization of anions or
c. by polymerization of organometallic compounds.

The network forming components, monomers or colloids react into active form after the preparation of a solution or homogeneous colloidal sol [18]. For stable colloids the neutralization of surface charges, aggregation and further condensation by reactive surface groups leads to gelation.

To deposit thin film, sol or precursor state is used while for fabricating fibers gel-state is used. Gels allow for a high degree of control of the crystallization and formation of different porous and dense microstructures [22].

Sol-gel spin coating

Sol-gel spin coating is a simple cost-effective and useful process for film deposition using solution type reagents. In this process the substrate is made to spin around an axis perpendicular to the coating area. The method includes four distinct stages.

i. In the first step a controlled amount of the precursor is poured over the substrate which wets substrate uniformly. If needed, sub-micron filter is also used to eliminate larger particles from the precursor.
ii. The second step involves spinning of substrate with desired rotation speed to remove the excess fluid. The top of the fluid layer exerts inertia while the substrate rotates at a faster speed. These two forces result in twisting motion which may lead to formation of spiral vortices. But in normal cases the precursor is thin enough so that it keeps co-rotating with the substrate and any evidence of thickness difference is absent. Ultimately the substrate reaches

its desired speed and the viscous shear drag is exactly balanced by the rotational acceleration.

iii. In the third stage viscous forces dominate the thinning behavior of the fluid. The fluid thinning tends to formation of uniform films. However, in few cases edge effects are also seen. The fluid which is rotating flows uniformly outside. If the fluid is in excess, then the drops must be formed at the edges so that they may fling off. Thus the thickness at the ends may be slightly greater than that at the central portion of the substrate leading to edge effect.

iv. In the fourth step and final stage fluid starts evaporating and dominates its own thinning behavior. It is the step in which the solvent phase gets removed and the sol is converted to dense ceramic. As the fluid rotates at a high speed, its temperature rises and leads to evaporation of the fluid. Thus the viscosity of the remaining solution increases leading to the 'gel-state' of the coating. The resulting film usually has an amorphous structure. Although the third and fourth stages i.e. viscous flow and evaporation occur simultaneously, the viscous flow effect dominates initially and evaporation dominates later.

The sol should be kept in an air tight flask to maintain its viscosity otherwise it gets converted into gel and cannot be used for the deposition of films.

The film thickness can be controlled by adjusting the solution viscosity and other coating conditions like rotation rate, annealing temperature and time duration of coating etc. [10, 23]. The sol gel spin coating method has been extensively used for the deposition of oxide films [24, 25-28,10, 13-16,30, 31].

The advantages of sol-gel process are

- Ultra homogenation due to atomic scale mixing,
- High degree of uniformity,
- Control of thickness,
- Possibility of multilayer coating,
- Control over the microstructure of the film i.e. pore volume, refractive index, pore size, surface area etc. and
- No restriction on shape and size of the substrate.
- Also the substrate can be simultaneously coated on both sides.

References

1. Joy George, 'Preparation of Thin Films' Pub. Marcel Dekker NY(**1992**).
2. S. Dixit, A. Srivastava, A. Srivastava and R. K. Shukla, J. Appl. Phys. 102. 113114 (**2007**).
3. S. K. Shukla, G. K. Parashar, A. P. Mishra, P. Misra, B. C. Yadav, R. K. Shukla, A. Srivastava, A. Srivastava, F. Deba, G. C. Dubey, Chemical Sensors, 20, Supplement B 546 (**2004**).
4. S. Dixit, A. Srivastava, A. Srivastava, R. K. Shukla, Jpn. J. of Appl. Phys. 47(7A) 5613 (**2008**).
5. H. Dong, D. Wang, K. Chen, J. Huang, H. Sun, W. Li, J. Xu, and Z. Ma, Appl. Phys. Lett. 94, 161101(**2009**).
6. Ph.D. Thesis, "Structural and Optical Properties of Zinc Oxide and Barium Titanate Based Thin Films" by Kamakhya Prakash Misra, University of Lucknow, **2010**.
7. J. D. Mackenzie and D. R. Ulrich, Proc. of SPIE Conf. on Sol-gel Optics, 1328 (**1999**) 2-13.
8. B. D. Fabes et al, Proc. of SPIE conf. on Sol-gel Optics, 1328 (**1990**) 319-328.
9. J. D. Mackenzie, Proc. of SPIE conf. on Sol-gel Optics, 878 (**1988**)128.
10. C. Y. Tsay, H. C. Cheng, C. Y. Chen, K. J. Yang and C. K. Lin, Thin Solid Films 518, (**2009**) 1603.
11. R. C. Mehrotra, History of Precursors, Proc. of the Winter School on Glasses and Ceramics from Gels; Sao Carlos (SP) Barzil 14-19 Aug **1989**, Ed. M. A. Aegerter, M. Jafelicci Jr, D. F. Souza and E. D. Zanotto, Utopia Press, Singapore pp. 1-12.
12. E. Matijevic, Accounts of Chem. Res. 14 (**1981**) pp. 22.
13. H. C. Cheng, C. F. Chen, C. Y. Tsay, Appl. Phys. Lett. 90, 012113 (**2007**).
14. W. J. Park, H. S. Shin, B. D. Ahn, G. H. Kim, S. M. Lee, K. H. Kim and H. J. Kim, Appl. Phys. Lett. 93, 083508(**2008**).
15. Y. Zhang, B. Lin, X. Sun, and Z. Fu, Appl. Phys. Lett 86, 131910(**2005**).
16. A. Jain, P. Sagar and R. M. Mehra, Materials Science-Poland, 25, 233(**2007**).
17. S. -Y. Bae, C. –S. Kim and Y. –J. Oh, J. of App. Phy. 85(8) 5226(**1999**).

18. Helmut Schmidt, 'Chemical Processing up to Gelation' Proc. of The Winter School on Glasses and Ceramics from Gels; Sao Carlos (SP) Barzil 14-19 Aug **1989**, Ed. M. A. Aegerter, M. Jafelicci Jr, D. F. Souza and E. D. Zanotto, Utopia Press, Singapore pp. 62.
19. I. Thomas, US Patent 3, 799, 754, March 26, **1974**; I. Thomas, 'Multicomponent Glasses from the Sol-gel Process' in Sol-gel Technology for Thin Films, Fibers, Preforms Electronics and Speciality Shapes, Ed. L. C. Klein, Noyes Publications, New Jersey, **1988**.
20. Sumio Sakka, Rheology of Sols in the sol-gel processing, Proc. of the Winter School on Glasses and Ceramics from Gels; Sao Carlos (SP) Barzil 14-19 Aug **1989**, Ed. M. A. Aegerter, M. Jafelicci Jr, D. F. Souza and E. D. Zanotto, Utopia Press, Singapore pp. 76.
21. Jerzy Zarzycki, New Methods in Sol-gel Synthesis, Proc. of the Winter School on Glasses and Ceramics from Gels; Sao Carlos (SP) Barzil 14-19 Aug **1989**, Ed. M. A. Aegerter, M. Jafelicci Jr, D. F. Souza and E. D. Zanotto, Utopia Press, Singapore pp. 257-269.
22. G. Westin, M. Wijk and A. Pohl, J. of Sol-gel Sci. and Tech. 31, 283 (**2004**).
23. Sumio Sakka, Rheology of Sols in the sol-gel processing, Proc. of the Winter School on Glasses and Ceramics from Gels; Sao Carlos (SP) Barzil 14-19 Aug **1989**, Ed. M. A. Aegerter, M. Jafelicci Jr., D. F. Souza and E. D. Zanotto, Utopia Press, Singapore pp. 346-374.
24. N. Kumar, A. Srivastava, Journal of Alloys and Compounds 706, (**2017**) 438-446
25. K. P. Misra, R. K. Shukla, A. Srivastava, A. Srivastava, Appl. Phys. Lett. 95 (**2009**) 031901.
26. A. Srivastava, N. Kumar, K. P. Misra, S. Khare, Mater. Sci. Semicond. Process. 26(**2014**)259–266
27. R. K. Shukla, A. Srivastava, A. Srivastava, and K. C. Dubey, J. Cryst. Growth 294 (**2006**) 427-431.
28. Nishant Kumar, A. Srivastava, Opto-Electronics Review 26 (**2018**) 1–10.
29. A. Srivastava, N. Kumar, and S. Khare, Opto−Electron. Rev. 22(**2014**) 68-76.
30. Y Natsume, H Sakata, Thin Solid Films, 372 (**2000**) 30–36.
31. Y. Cao, L. Miao, S. Tanemura, M. Tanemura, Y. Kuno, Y. Hayashi, Appl. Phys. Lett. 88, (**2006**) 251116.

Chapter: 3

Bandgap engineering of the perovskite materials for solar cell applications

[1]R. K.Shukla, [2]Amrit Kumar Mishra and [3]K. C. Dubey

[1]Department of physics, University of Lucknow, Lucknow - 226007, U.P. (India)

[2]Department of physics, University of Lucknow, Lucknow - 226007, U.P. (India)

[3]Department of physics, Shia P. G. College Lucknow U. P. (India)

E-mail: amritmishra.mishra154@gmail.com; rajeshkumarshukla_100@yahoo.co.in

Abstract: Nowadays, Perovskite materials are frequently used in the application of solar cells. We are using organic-inorganic halide like $CH_3NH_3PbI_3$, $CH_3NH_3PbCl_3$ and$CH_3NH_3PbBr_3$ in which CH_3NH_3 is organic part, Pb is the inorganic part and I, Cl, Br is the halide atom. In all types of solar cells, I have worked on the perovskite solar cell nowadays which is frequently used in the energy harvesting materials for Solar cell applications. The perovskite solar cells have a rapid enhancement in the power conversion efficiency from 3.8% in 2009 to 23% in 2020. The good efficiency, large diffusion length, good photon absorption capacity, good mobility, low cost, and easy fabrication process motivated me to research perovskite solar cells. Photovoltaic systems combined with tandem solar cells have been successfully investigated to generate high power conversion efficiencies. Nevertheless, this fascinating concept has not yet been adequately applied to solar cells based on perovskite.In this chapter, we assess the feasibility of using perovskite semiconductors with different bandgaps for tandem concentric solar cell applications in combination with different bandgap for tandem concentric solar cell applications in combination with conventional crystalline silicon. We evaluate the device performance of tandem perovskite concentrator solar cells.

Keywords: perovskite, diffusion length, band gap, efficiency.

1. Introduction:

Nowadays, perovskite material is frequently used in solar cell devices as an active layer. The crystal structure of perovskite material ABO_3, A stands for an organic part (CH_3NH_3), B stands for the inorganic part (Pb) of the material, and O stands for the halide atom (like Cl, Br, I)

terminology used in the perovskite ($CH_3NH_3PbI_3$) photovoltaic material. The phase transitions occur in the perovskite ($CH_3NH_3PbI_3$) at 160 K from orthorhombic structure to tetragonal structure and at 327 K tetragonal to cubic structure obtain [1]. The ABO_3 crystal structure of the Perovskite materials is shown in figure 1.

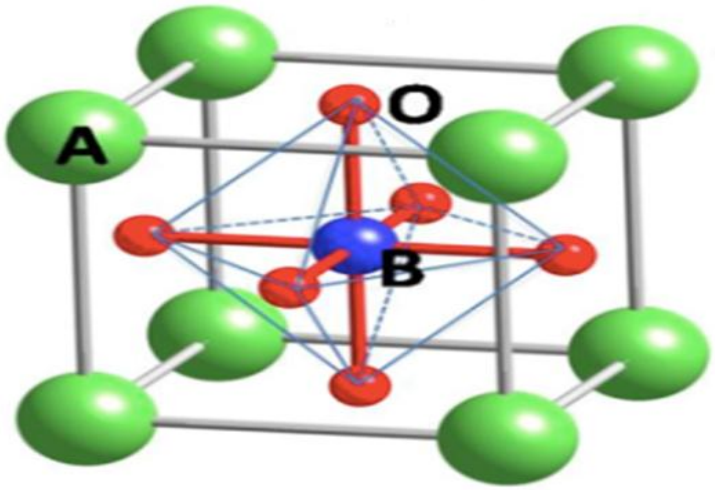

Figure 1: TheABO_3 crystal structure of the Perovskite materials

The extraordinary material properties of the perovskite solar cell have a major role for the frequently used perovskite material in the device physics; T perovskite material has a long charge carrier diffusion length, high absorption coefficient, low exciton binding energy, and tuneable band gap [2-7]. However, Lab-scale device efficiency is higher than the commercially available solar cells, The stability issue exists in the perovskite solar cells since perovskite solar cell degradation concerning time, and degradation occurs due to air, UV light exposure, thermal stress (heat). light soaking, electric fields, humidity, and many other factors [8-10].due to this factor, we could not achieve the market requirement. Hence, we focused on the detailed degradation study of the perovskite solar cell for the improvement of device stability. The stability enhancement is done by adding UV filters, device encapsulation, and suppressing trap states (degradation caused by air and humidity), UV light, and electric fields, respectively [11-14]. During the operation of the perovskite solar cell thermal stress degradation occurs due to this, we will first focus on the structural change of perovskite material with a temperature change of the device. The device consists of many layers and this study specifically highlights the

intrinsic degradation mechanisms of the perovskite absorber layer, including chemical, optical and morphological degradation.

2. Device Fabrication

The solar cell fabrication technique was done by a spin coating method which is shown in Figures 2(a), 2(b), 2(c), and figure 3.

We are using patterned fluorine-doped tin oxide substrates (FTO) etched by Zn metal powder and dilute hydrochloric acid. The cleaning of etched FTO was done by sequential sonication technique into the soap solution, deionized water, and isopropanol for 15 min each. And next, coat TiO_2 (hole blocking layer) on it by using the spin coating method with 5000 rpm for 45 sec and heated at 450^0 C for 25 minutes, which is prepared by the mixture of 0.5 ml Ti (IV) isopropoxide (Sigma Aldrich), 7.25 ml of ethanol and 75 microlitersof concentrated HCl. A TiO_2 Mesoporous layer is made by using a dilute solution of Dyesol 18 N-RT paste (1:3.5 w/w in ethanol) at 4000 rpm for 30 seconds and heated at 500^0C for 30 minutes and the film thickness to be formed 360 nm.

2.1 Preparation of perovskite:

For the perovskite deposition, TiO_2 films were transformed into the glove box. The perovskite layer was deposited.

2.2 $TiCl_4$ Treatment:

First, we take 2M $TiCl_4$ (1 ml) in 100ml D.I. water and put TiO_2 film's into the solution, and heat at 80^0C in the oven. After that, the film is wash with water, ethanol, and dry Ar gas, and then heated at 500^0C at 30 minutes and again we take 1M PbI_2 (462 mg) solution in DMF (1 ml) and steering at 40^0C up to dissolve, after that spin-coated at 6000 rpm for 5 sec. Heated for 25 min at 70^0C on a hot plate, drop into MAI (8mg/ml) in isopropanol after that dip the PbI_2 film into the above solution for 15 min, and then washed with isopropanol and then heated at 70^0C for 15 min.

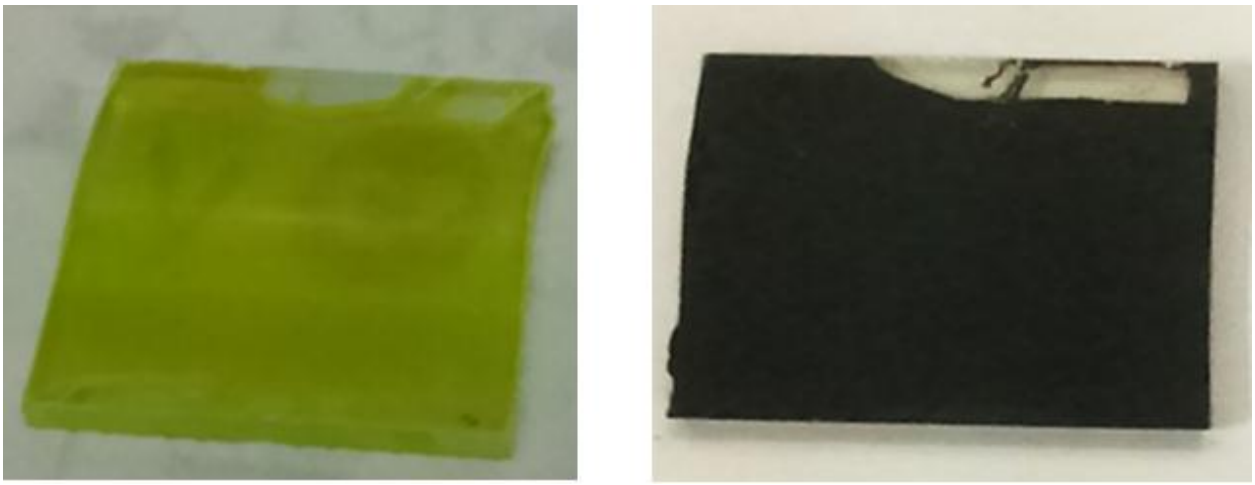

Figure 2(a): PbI_2 layer deposition onthe FTO glass;(b): $CH_3NH_3PbI_3$ layerdeposition on FTO glass.

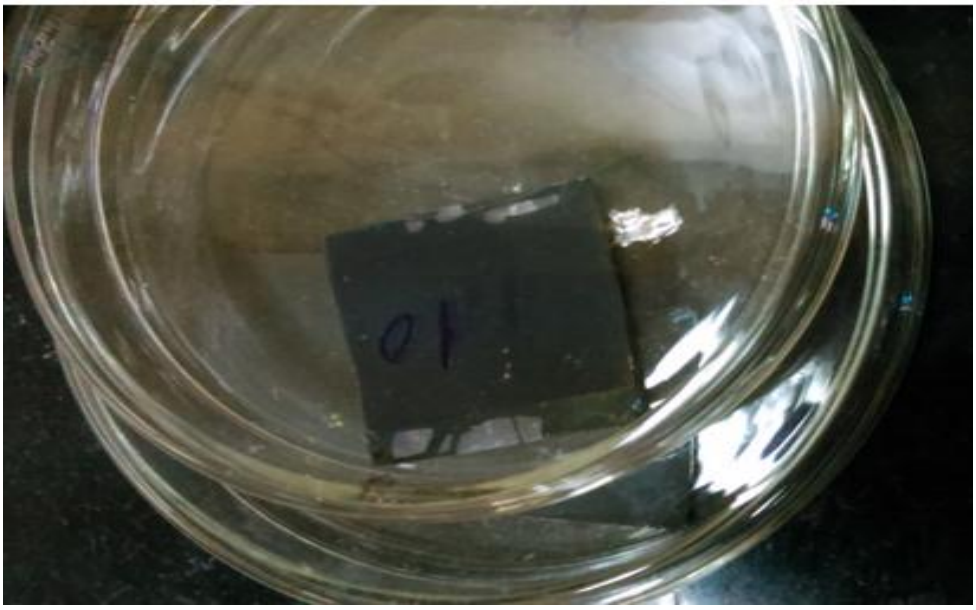

Figure 2(c): perovskite film in the desiccator

2.3 Spiro-MeOTAD Layer Deposition:

First, we take 100 mL of Spiro-MeOTAD in 1 mL chlorobenzene 28.5 microliters of TBP (Tursary butyl pyridine) + Li salt solution (17.5 microliters) using spin coater at 4000 rpm for 30 sec and finally gold deposition on Spiro-MeOTAD layer by the thermal evaporator.

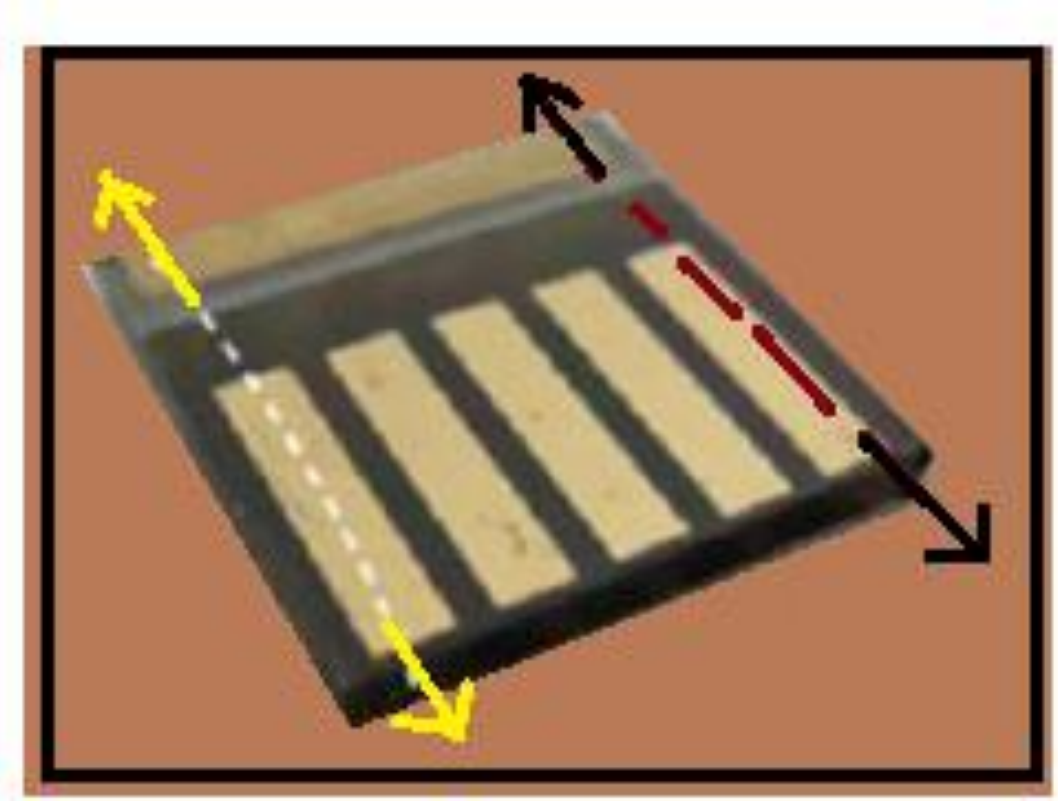

Figure 3: The perovskite solar cell (the region under the Arrow showed the active area of the device)

3.0 Electrical characterization of the perovskite solar cell:

- J-V Characteristics
- C-V Characteristics
- C-f Characteristics
- I-Rh (%), Current – Relative humidity spectra.
- I-t, Current – Time spectra
- Noise spectroscopy

3.1 J-V Characteristics

J-V measurements of the perovskite solar cell done by using Keithley 2450 source - measure unit under the AM1.5G 100 mW/cm^2 solar spectrum and light intensity measured by PM -100 A compact power meter. The applied potential across the DUT (device under test) was +5 V to -5 V and the scan rate was 200 mV/s.

3.2 C-V Characteristics

The apparatus used for the capacitance-voltage measurements of the perovskite solar cell were 4 MHz DSP Lock-in amplifier, Stanford Research System SR 865 A, and key sight 33621 A waveform generator.

3.3 C - f Characteristics

The C - f measurements of the perovskite solar cell by using the SR 865 A, SR 560 voltage pre-amplifier, 4 MHz DSP Lock-in amplifier, and 33621 A waveform generator.

3.4 Current - Relative humidity I-Rh (%), Curve

The electrical current versus relative humidity spectrum was observed in the perovskite solar cell by applied +5 V to -5 V DC source to the DUT (device under test) by Keithley 2450 source - measure unit under the AM1.5G 100 mW/cm^2 solar spectrum. Humidity control is done by sending wet nitrogen, dry nitrogen, humid air, or dry airflow to the humidity control chamber.

3.5 I-t, Current -Time spectra

The electrical current versus time spectrum was observed at a fixed humidity level in the perovskite solar cell by applied +5 V to -5 V DC source to the DUT (device under test) by Keithley 2450 source - measure unit under the AM1.5G 100 mW/cm^2 solar spectrum.

3.6 Noise spectroscopy

The study of noise allows the explanation of the electrical parameters of the defect states, charge carrier dynamics which are the major factors to explain the quality of the heterojunction solar cells and photovoltaic modules [4-5]. 1/f noise spectrum observed in the typical perovskite solar cells which are a powerful tool to the explanations of charge carriers injection, mobility of the photovoltaic material, defect states, and how 1/f noise spectrum shift after degradation of the perovskite solar cells. 1/f noise is the dominant noise in the Low-Frequency range and its spectral density is proportional to 1/f. Low-frequency 1/f noise is used to the model fluctuation of the device parameter with time.

4.0 Structural, Morphological and simulation of the perovskite solar cell

4.1 X-Ray diffraction

In the field of material science, condensed matter physics XRD investigation is a very important tool for the understanding of the crystal structure of bulk solids, thin films including lattice

constant, the orientation of polycrystalline films, geometry, identification of unknown materials, defects, stress, determination of the particle size, etc. The electrons, neutrons are also used for diffraction studies from materials.

Mathematically, Bragg's law is bellowed.

$$2d\sin\theta = n\lambda$$

Where d is the inter planer spacing of the atoms, n is the order of diffraction, λ is the wavelength of light used during the XRD investigation and θ is the glancing angle of X-rays. The pattern can then be compared with JCPDS (Joint committee on power diffraction standards) database cards or any other reported research work. Thus identification of given by Figure 4.

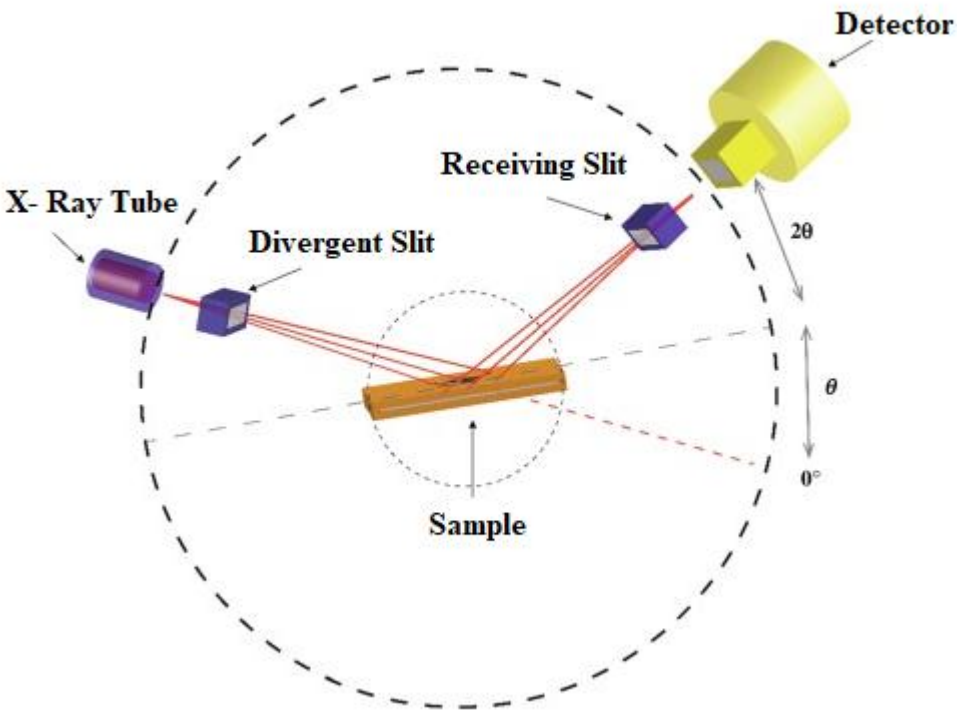

Figure 4: The schematic diagram of the X-Ray Diffractometer

4.2 Scanning electron microscope (SEM)

The application of SEM is explored in the field of material science for the understanding of the surface morphology of the sample. The SEM is a type of electron microscope in which an image of a sample is taken by scanning the surface of the sample with a focused beam of electrons. The

interaction of electrons with atoms in the sample creates various signals that contain information about the surface morphology, composition of the sample, and other properties such as electrical conductivity. The scanned electron beam develops a pattern, and the position of the beam is combined with the intensity of the detected signal to produce an image**.**

SEM of the transverse cross-section of a homogeneous sample can indicate the thickness of the films. The most common or standard detection mode is secondary imaging where the scanning electron micrograph can produce a very high-resolution image of a sample surface revealing details about less than 1 nm in size. The very narrow electron beam facilitates a large depth of field yielding a characteristic three-dimensional appearance useful for understanding the surface structure of a sample**.** The schematic diagram of the image formation system of SEM is shown in Figure 10.

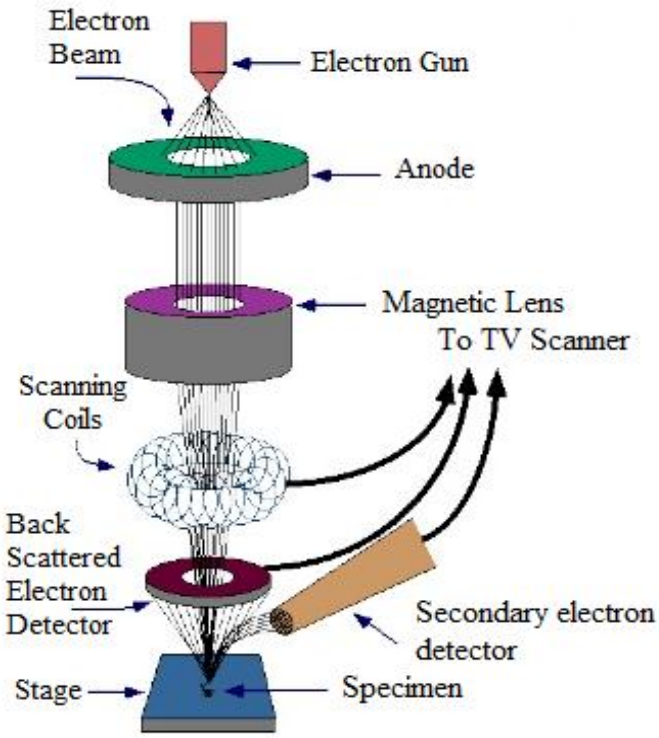

Figure 10: The schematic diagram of the image formation system of SEM

Conclusion

We explained the basic physics of the solar cell and types of solar cell why perovskite is suitable for the energy harvesting material in the material science field and the history of the perovskite solar cell, bandgap engineering, and the different experimental characterization techniques for the explanation of the physical and chemical properties of the perovskite solar cell. Currently, crystalline silicon solar cells are dominant in the commercial and private PV market. The efficiency of these devices is high (>25%). However, these solar cells are thicker, heavier, and rigid when compared to thin-film PV technologies. Thin-film photovoltaics have already been implemented in the specific market such as extra-terrestrial solar panels. However, highly efficient (>25%) thin-film solar cells often use highly toxic or very expensive materials.

Reference

[1] Tanzila Tasnim Ava, Abdullah Al Mamun, Sylvain Marsillac and Gon Namkoong**.** A Review: Thermal Stability of Methylammonium Lead Halide Based Perovskite Solar Cells. Appl. Sci. **2019**, 9, 188; doi: 10.3390/app9010188.

[2] Hao, F.; Stoumpos, C.C.; Cao, D.H.; Chang, R.P.; Kanatzidis, M.G. Lead-free solid-state organic–inorganic halide perovskite solar cells. Nat. Photonics **2014**, 8, 489. [CrossRef]

[3] Lin, Q.; Armin, A.; Nagiri, R.C.R.; Burn, P.L.; Meredith, P. Electro-optics of perovskite solar cells. Nat. Photonics **2015**, 9, 106. [CrossRef]

[4] Miyata, A.; Mitioglu, A.; Plochocka, P.; Portugall, O.; Wang, J.T.W.; Stranks, S.D.; Snaith, H.J.; Nicholas, R.J. Direct measurement of the exciton binding energy and effective masses for charge carriers in organic-inorganic tri-halide perovskites. Nat. Phys. **2015**, 11, 582–587. [CrossRef]

[5] Stranks, S.D.; Eperon, G.E.; Grancini, G.; Menelaou, C.; Alcocer, M.J.; Leijtens, T.; Herz, L.M.; Petrozza, A.; Snaith, H.J. Electron-hole diffusion lengths exceeding 1 micrometer in an organometal trihalide perovskite absorber. Science **2013**, 342, 341–344. [CrossRef]

[6] Xing, G.; Mathews, N.; Sun, S.; Lim, S.S.; Lam, Y.M.; Grätzel, M.; Mhaisalkar, S.; Sum, T.C. Long-range balanced electron-and hole-transport lengths in organic-inorganic CH3NH3PbI3. Science **2013**, 342, 344–347.[CrossRef]

[7] Noh, J.H.; Im, S.H.; Heo, J.H.; Mandal, T.N.; Seok, S.I. Chemical management for colorful, efficient, and stable inorganic–organic hybrid nanostructured solar cells. Nano Lett. **2013**, 13, 1764–1769. [CrossRef] [PubMed]

[8] Niu, G.; Guo, X.;Wang, L. Review of recent progress in chemical stability of perovskite solar cells. J. Mater. Chem. A **2015**, 3, 8970–8980. [CrossRef]

[9] Grätzel, M. The light and shade of perovskite solar cells. Nat. Mater. **2014**, 13, 838. [CrossRef] [PubMed]

[10] Li, X.; Tschumi, M.; Han, H.; Babkair, S.S.; Alzubaydi, R.A.; Ansari, A.A.; Habib, S.S.; Nazeeruddin, M.K.; Zakeeruddin, S.M.; Grätzel, M. Outdoor performance and stability under elevated temperatures and long-term light soaking of triple-layer mesoporous perovskite photovoltaics. Energy Technol. **2015**, 3, 551–555. [CrossRef]

[11] Han, Y.; Meyer, S.; Dkhissi, Y.; Weber, K.; Pringle, J.M.; Bach, U.; Spiccia, L.; Cheng, Y.B. Degradation observations of encapsulated planar CH3NH3PbI3 perovskite solar cells at high temperatures and humidity. J. Mater. Chem. A **2015**, 3, 8139–8147. [CrossRef]

[12]. Leijtens, T.; Eperon, G.E.; Pathak, S.; Abate, A.; Lee, M.M.; Snaith, H.J. Overcoming ultraviolet light instability of sensitized TiO2 with meso-superstructured organometal tri-halide perovskite solar cells. Nat. Commun.**2013**, 4, 2885. [CrossRef]

[13] Chen, W.; Wu, Y.; Yue, Y.; Liu, J.; Zhang, W.; Yang, X.; Chen, H.; Bi, E.; Ashraful, I.; Grätzel, M.; et al. Efficient and stable large-area perovskite solar cells with inorganic charge extraction layers. Science **2015**, aad1015.

[CrossRef]

[14] Shao, Y.; Yuan, Y.; Huang, J. Correlation of energy disorder and open-circuit voltage in hybrid perovskite solar cells. Nat. Energy **2016**, 1, 15001.

Chapter: 4

Molecular interaction studies of DMSO-Toluene binary mixtures at Different Temperatures by Ultrasonic Technique

Sunil Dahire

Department of Chemistry, Dada Ramchand Bakhru Sindhu Mahavidyalaya, Nagpur, India.

E-mail: drsunildahire@gmail.com

Abstract: Ultrasonic is an effective Technique to study the molecular interactions of binary liquid mixtures. In this work ultrasonic velocity, viscosities and densities of Dimethyl Sulphoxide (DMSO) and Toluene at 293K, 298K, 303K, 308K and 313K are measured. The Acoustical parameters such as adiabatic compressibility (β), Free length (L_f), Free volume (V_f), Acoustic impedance (Z), etc. are calculated. The variations of these acoustical parameters with different compositions and at different temperatures are studied.

Keywords: Molecular interactions, ultrasonic study, DMSO-Toluene binary mixture

1. Introduction:

Investigations on being binary mixtures of non-electrolytes by calculating acoustical parameters are found to be highly useful in understanding the solute-solvent interactions in these mixtures. Ultrasonic wave propagation affects the physical properties of the medium and hence, can furnish information on the physics of the liquid and liquid mixtures. The measured ultrasonic parameters are being extensively useful to study intermolecular processes in liquid systems. The sign and magnitude of the non-linear deviations from ideal values of velocities and adiabatic compressibilities of liquid mixtures with composition are attributed to the difference in molecular size and strength of interaction between unlike molecules The present investigation related on acoustical properties of binary liquid mixtures of containing dimethylsulphoxide (DMSO), which is aprotic, strongly associated due to highly polar S=O group molecule and large dipole moment and dielectric constant (μ = 3.96 & €=46.68 at 298 K). The study of DMSO is important because of its utilization in a broad range of applications in medicines. Also, well established is the use of DMSO as an anti-inflammatory agent which commonly has been used for arthritic conditions. DMSO has also been utilized as a free radical scavenger for various cancer treatments. The unique properties of DMSO also give rise to its wide use as a solvent. In

view of the importance mentioned, an attempt has been made to elucidate the molecular interactions in the mixtures of DMSO + toluene at different temperature range. Further, acoustical parameters namely adiabatic compressibility (β), free length (Lf), free volume (Vf), internal pressure (πi), and acoustic impedance (Z) have been evaluated. Also, the values of some of the acoustical parameters have been calculated from the measurements of ultrasonic velocity, density and viscosity of the mixtures .The binary liquid system taken is DMSO+ Toluene.

2. Materials and Methods:

The liquid mixtures of various concentrations in mole fraction were prepared by taking AR grade Chemicals. In all systems, the mole fractions were varied so as to have the mixtures of different compositions. The density of liquid mixtures was determined using a Digital Densitometer (Rudolf). An Ostwald's viscometer (10ml capacity) was used for the viscosity measurements with efflux time was determined using a digital chronometer to within ±0.01s. An ultrasonic interferometer having the frequency of 2 MHz (Mittal Enterprises, New Delhi, Model -F-81) with overall accuracy of 3 ms^{-1} has been used for velocity measurements. An electronically digital operated constant temperature has been used to circulate water through the double walled measuring cell made up of steel containing the experimental solution at the desired temperature. The accuracy in the temperature measurement is ± 0.1K.

3. Formulae to calculate acoustical parameters

$$\beta = 1/U^2 . \rho$$

$$Lf = K. \beta^{½}$$

$$V_f = (M_{eff} . U/K.\eta)^{3/2}$$

$$Z = U. \eta$$

$$\Delta G = KT \ln(KT\zeta/h)$$

4. Table I

Values of Density, Viscosity and Ultrasonic velocity of the binary liquid system DMSO and Toluene at 293K, 298K, 303K, 308K and 313K

Temp.	Mole Fractions of DMSO	Density $\rho/(Kg/m^3)$	Viscosity $\eta(*10^{-3}NSm^{-2})$	Velocity U(m/s)
20	1	1100.3	0.002589926	1498.933
	0.857291104	1058.4	0.001758891	1456.6
	0.692565641	1007.6	0.001242287	1418.4
	0.500302802	962.4	0.000951265	1383.3
	0.272967579	915.3	0.000774064	1348.4
25	1	1095	0.00232263	1481.733
	0.857291104	1053.4	0.001469159	1438.66
	0.692565641	1003	0.001128061	1400.6
	0.500302802	957.7	0.000894279	1364.53
	0.272967579	910.4	0.000894279	1329.6
30	1	1089.8	0.002163828	1472.933
	0.857291104	1048.3	0.001318399	1405.33
	0.692565641	998.2	0.001046671	1382.93
	0.500302802	952.7	0.000867961	1344.8
	0.272967579	905.5	0.000675483	1309.86
35	1	1084.6	0.001924734	1451.6
	0.857291104	1043	0.001191273	1406.26
	0.692565641	993.2	0.000963122	1367.73
	0.500302802	947.7	0.000778815	1330.93
	0.272967579	900.5	0.000627798	1292.4
40	1	1079.2	0.001692748	1437.733
	0.857291104	1037.7	0.001120852	1390.8
	0.692565641	987.9	0.000923323	1350.4
	0.500302802	942.4	0.000751726	1313.73
	0.272967579	895.2	0.000597938	1273.6

5. Table II

Values of acoustical parameters at different parameters

Temp		Mole fractions			
		0.857291104	0.692565641	0.5003028	0.272967579
20	Lf	1.33157E-08	1.40148E-08	1.4704E-08	1.54678E-08
	Vf	6.10269E-08	1.03094E-07	1.555E-07	2.15428E-07
	β	4.45317E-10	4.93304E-10	5.4301E-10	6.00896E-10
	Z	1541665.44	1429179.84	1331287.92	1234190.52
	π	649082921.2	517796710	428832022	363234400.6
25	Lf	1.35137E-08	1.42254E-08	1.4943E-08	1.57287E-08
	Vf	7.847E-08	1.16907E-07	1.6714E-07	2.38903E-07
	β	4.58659E-10	5.08242E-10	5.608E-10	6.21335E-10
	Z	1515484.444	1404801.8	1306810.38	1210467.84
	π	605197932.7	503493774.8	424409398	355650846.2
30	Lf	1.38678E-08	1.44418E-08	1.5202E-08	1.60089E-08
	Vf	8.91183E-08	1.28337E-07	1.7102E-07	2.5302E-07
	β	4.83012E-10	5.2382E-10	5.804E-10	6.43668E-10
	Z	1473207.439	1380440.726	1281190.96	1186078.23
	π	587911212.3	494699084.7	426763493	353502335.8
35	Lf	1.38938E-08	1.4639E-08	1.5401E-08	1.62701E-08
	Vf	1.03861E-07	1.43003E-07	1.981E-07	2.76761E-07
	β	4.84824E-10	5.38223E-10	5.9569E-10	6.64848E-10
	Z	1466729.18	1358429.436	1261322.36	1163806.2
	π	565985759.3	483443125.4	411628504	347479987.1
40	Lf	1.40841E-08	1.48666E-08	1.5646E-08	1.65591E-08
	Vf	1.7071E-07	2.18448E-07	2.8533E-07	3.83928E-07
	β	4.98194E-10	5.55088E-10	6.1483E-10	6.88674E-10
	Z	1443233.16	1334060.16	1238059.15	1140126.72
	π	403407516.7	359708709.5	318982539	279301801.4

6. Plot of Mole fraction Vs. Gibb's free energy

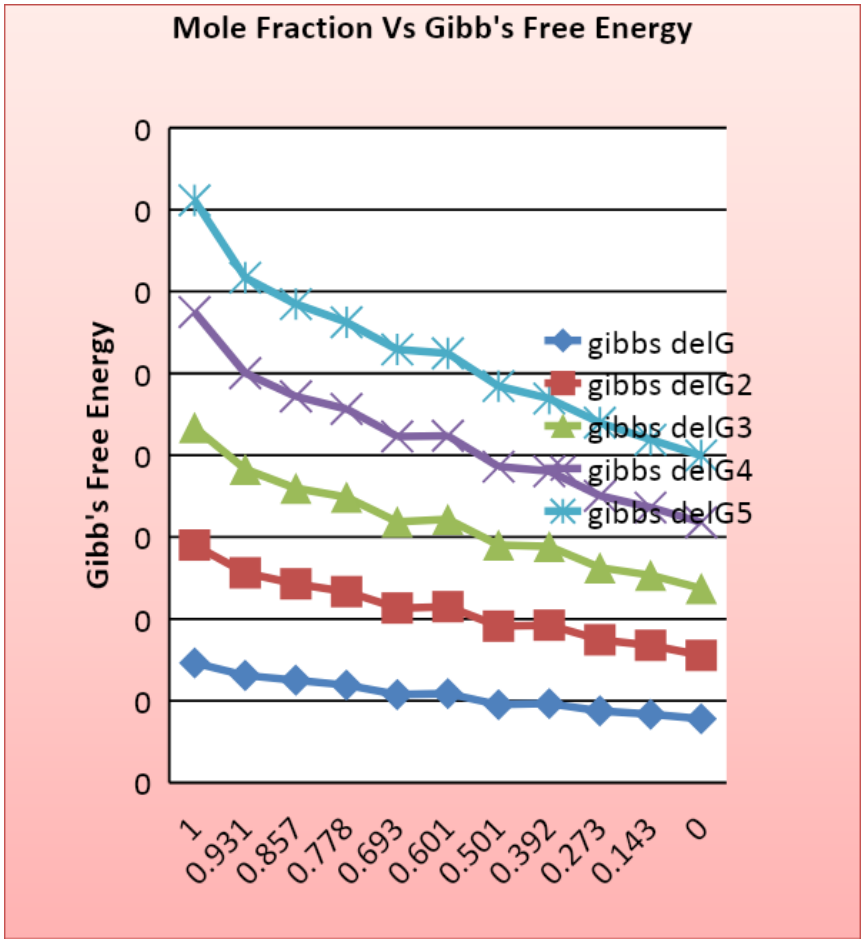

7. Results and Discussion

The experimentally determined values of density (ρ), viscosity (η) and ultrasonic velocity (U) of the binary liquid mixture at different temperature range are presented in Table 1. The values of adiabatic compressibility (β), free length (L_f), free volume (V_f), internal pressure (π) and acoustic impedance (Z) for the binary liquid mixture at all the temperature are reported in Table 2. It is evident from the Table 1 that the density (ρ), viscosity (η) and ultrasonic velocity (U) decreases with decreasing molar concentration of DMSO in the binary liquid mixture of DMSO +Toluene. The pronounced increase or decrease in these parameters with composition of mixtures indicates the presence of interactions between the component molecules in the binary mixture. When DMSO is associated with Toluene the mixture formed by this combination have not only dipolar-dipolar interaction between DMSO molecules, but also the interaction of dipolar-induced dipolar between DMSO molecules and Toluene molecules. The interaction

between unlike molecules seems to be stronger than the intra-molecular interactions and it leads to decrease of interaction of molecule.

When DMSO is in association with toluene, DMSO tends to break DMSO-DMSO dipolar association releasing several DMSO dipoles. Consequently, the free dipoles of DMSO would induce moments in the neighboring molecules of toluene, resulting in dipolar induced dipole interaction leading to contraction in volume. This leads to subsequent increase in adiabatic compressibility (β), free volume (V_f) and as well as in intermolecular free length (Lf) is observed in the binary mixture of DMSO +Toluene, with the decreasing molar concentration of DMSO, which is evident further, in this binary mixture, the values of acoustic impedance (Z) is found to be decreased, which are listed in Table 2. When an acoustic wave travels in a medium, there is a variation of pressure from particle to particle. The ratio of the instantaneous pressure excess at any particle of the medium to the instantaneous velocity of that particle is known as 'specific acoustic impedance' of the medium. It is important to examine specific acoustic impedance in relation to concentration and temperature. In the present investigation, it is observed that these acoustic impedance (Z) values increase with increasing concentration of DMSO. Such an increasing values of acoustic impedance (Z), further supports the possibility of molecular interactions between the unlike molecules.

8. Conclusion

From the observed experimental values of ultrasonic velocity, density and viscosity, related Acoustical parameters for the binary liquid mixtures of toluene with dimethyl sulphoxide (DMSO) at different temperature range. It is very obvious that there exists a molecular association between the components of the liquid mixtures. When DMSO is associated with toluene, mixtures formed by this combination have not only dipolar-dipolar interaction between the DMSO molecules, but also the interaction of dipolar-induced dipolar between the DMSO and Toluene molecules. Such an interaction between unlike molecules seem to stronger than the intra-molecular interactions which will lead to decrease of interaction. Hence, it is very obvious that weak dipole –dipole and dipole-induced dipole forces dominate resulting in existence of weak interactions in the present study.

References

1. S. Thirumaran and M. Rajeswari, *Archives of Physics Research*, **2011**, 2 (2), pp. 149.
2. R. Palani & K. Meenakshi, *Ind. J. Chem*., Vol. 46A, February **2007**, pp. 252.
3. S. Prabhakar and K. Rajagopal, *J. Pure Appl. Ultrason*. Vol. 27,**2005**, pp.3.
4. D Sravana Kumar & D Krishna Rao, *Ind. J. of Pure & Applied Physics*, Vol.45, March **2007**, pp. 210.
5. Narendra K, Tulasi K B, Baburao K, *J. Pharma. And Chem. Sci*., Vol. 2, Dec.**2011**, pp.916.

Chapter: 5

An overview of Deep Eutectic Solvents (DESs): An emerging class of green solvents

Byanju Rai[1] and Ratnakar Dutt Shukla[2]

[1]Assistant Manager, R& D, HPL AdditivesLimited, Faridabad, Haryana

[1]Department of Chemistry, Pt. D. D. U. Govt. Model I. College, Bahua, Fatehpur, UP

E-mail: byanju.rai25@gmail.com; rdbhuchem09@gmail.com

Abstract: Deep eutectic solvents (DESs) have been emerged as novel green and sustainable solvent and characterized by remarkable depressions in melting points in comparison to those of the neat constituent components. DESs are considered as cost effective "designer" solvents exhibiting a host of tunable physicochemical properties. The comprehensive study of the recent literature demonstrates the lack of predictive understanding of the microscopic mechanisms that execute the structure-property relationships in this class of solvents. The principal cause of the melting point depressions as well as physicochemical properties of DESs is the extensive hydrogen bonding. It is imperative to understand these systems as dynamic entities using both simulations as well as experiments. The present chapter covers the basic knowledge and recent research progresses regarding DES. It also focus on the recent progresses in the field of DES research, frames excellent scientific understanding, and recognizes potential research areas associated with the progress of the field toward predictive models and basic knowledge of these solvents.

Keywords: Deep Eutectic Solvent (DES), Green solvent, Hydrogen bonding

Introduction:

In viewpoint of green chemistry, solvents play a crucial role in the field of organic synthesis. To be considered as a sustainable solvent, solvents should possess the various salient features like easy availability, biodegradability, recyclability, non-toxicity, and cost effective in comparison to others. Up to the date, the availability of green solvents is rather limited in number. In this context, Deep Eutectic Solvents, a novel class of ionic liquids, are now rapidly emerging as a green and sustainable solvent in the field of synthetic chemistry.[1-2] A DES is a fluid generally

composed of two or three easily available, cost effective and benign components that has potential for self-association, often via hydrogen bond interactions and consequently form a eutectic mixture exhibiting a melting point lower than that of each individual component.[3] DESs are commonly in liquid state at temperatures lower than 100 °C. These DESs show identical physico-chemical properties to the conventionally employed ionic liquids, while being much cost effective and environmentally benign. Considering to these aforementioned advantages, DESs have attracted the great interest in many areas of research. In this chapter, we compile the fundamental understanding and significant applications of DESs. All contributions covered in this chapter aim at demonstrating that DESs not only offer the design of sustainable processes but also open a straightforward access to novel chemicals and materials.

In last two decades, room temperature ionic liquids (RTILs) have attracted considerable attention especially in the field of catalysis, electrochemistry, material chemistry, and more recently for the pre-treatment of biomass.[4-5] At the early stages of these research studies, scientists particularly focused on the preparation of ionic liquids by mixing metal salts, mostly aluminium, zinc, tin and iron chlorides, with quaternary ammonium salts. However both salts exhibit very high melting points, their proper mixing leads to the formation of a liquid phase which is known as eutectic mixture. These eutectic mixtures are commonly characterized by a very large depression of freezing point, generally higher than 150 °C. With the emergence of the concept of green chemistry, the preparation of metal-free ionic liquids (ILs) is highly desirable. In this regard, numerous efforts were attempted to the design of ILs by mixing an organic cation (usually imidazolium-based cations) with a large variety of anions, the most common ones being Cl^-,BF_4^-, PF_6^-, NTf_2^-. From that time, ILs have emerged as a new class of potential solvents. The possibility to chemically transform the cationic moiety almost infinitely in combination with a very large choice of anions provides chemists a broad range of ILs possessing different physical properties like density, melting point, viscosity, solubility, conductivity, and refractivity, among others. For example, in 2009, Seddon and co-workers have reported that 1018 different ILs can be theoretically prepared, 250 of them being already commercialized.[6-7] Considering to their high boiling point and low vapour pressure, which enables their recycling, ILs were qualified as green solvents. Although, the ‘‘green affiliation’’ of these novel solvents is now greatly contested in the current literature.[8]

Indeed, many reports pointed out the hazardous toxicity and the very poor biodegradability of most ILs.[9] ILs with high purity is also needed because impurities, even in trace amounts, exert influence on their physical properties. In addition, for the synthesis of ILs often needs a large amount of salts and solvents to completely exchange the anions, therefore the preparation of ILs is not considered as environmentally friendly. These shortcomings along with the high price of common ILs unfortunately hamper their industrial success. Therefore new concepts are now strongly required in order to exploit these systems in a better logical way.

To overcome the toxicity and high price of ILs, a new generation of solvent, called as Deep Eutectic Solvents (DES), has emerged at the beginning of this century. Preparation of these DESs can be obtained by simply mixing together two safe components (cheap, biodegradable and renewable), which are capable of generating a eutectic mixture. One of the most common components employed for the preparation of these DESs is choline chloride (ChCl). ChCl is a non-toxic, very cheap, and biodegradable quaternary ammonium salt which can be either extracted from biomass or smoothly synthesized from fossil reserves via a very high atom economy process. In combination with safe hydrogen bond donors such as urea, renewable carboxylic acids (e.g. oxalic, citric, succinic or amino acids) or renewable polyols (e.g. glycerol, carbohydrates), ChCl is capable of expeditiously generating a DES. However most of DESs are composed from ChCl as an ionic species, DESs cannot be treated as ILs because:

(1) DESs are not completely made up of ionic species

(2) DESs can also be obtained from non-ionic species.

In comparison to the conventional ILs, DESs derived from ChCl possess numerous advantages such as (1) low price, (2) chemical inertness with water (i.e. easy storage), (3) easy to prepare since DESs are obtained by simply mixing two components, thus by-passing all problems of purification and waste disposal often encountered with ILs and (4) most of them are biodegradable,[10] Biocompatible[11] and non-toxic,[12] reinforcing the greenness of these media.[13]

Physico-chemical properties of DESs (chemical inertness, viscosity, density, refractive index, conductivity, surface tension, etc.) are very close to those of common ILs. For this reason, DESs derived from ChCl are also intimately named “biorenewable” or “biocompatible” or ionic liquids in a few studies. Regards to their low ecological footprint and attractive price, DESs have now become of growing interest both at academic and industrial levels and the number of publications

dedicated to the use of DESs is now expeditiously increasing in the current literature, further expressing the attractiveness of these media.

2. Definition of DESs

A DES is often composed of two or three cheap and safe components which are capable of associating with each other, via hydrogen bonding, to form a eutectic mixture. The resulting DES is characterized by a melting point lower than that of each individual component. Generally, DESs are featured by a very large depression of freezing point and are liquid at temperatures lower than 150 °C. Notably most of them are liquid between room temperature and 70 °C. Mostly, a DES is produced by mixing a quaternary ammonium salt with metal salts or a hydrogen bond donor (HBD) that has the potential to generate a complex with the halide anion of the quaternary ammonium salt. Figure 1 and figure 2 summarizes the different quaternary ammonium salts that are widely employed in combination with various HBDs in the preparation of DESs.

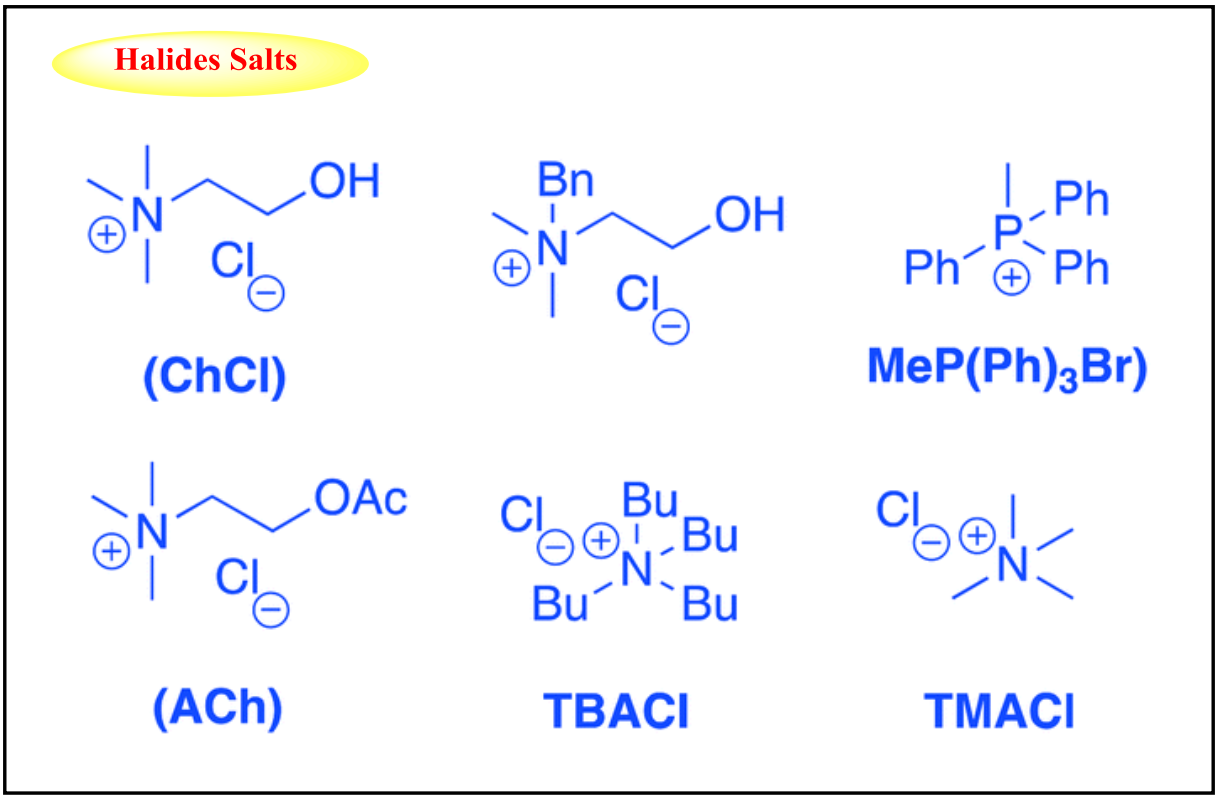

Figure 1: Representative example of the halide salts explored for the preparation of DES

In 2007, Abbott and co-workers defined DESs using the general formula $R_1R_2R_3R_4N^+X^-Y^-$.12

Type I DES Y = MClx, M = Zn, Sn, Fe, Al, Ga

Type II DES Y = MClx.yH2O, M = Cr, Co, Cu, Ni, Fe

Type III DES Y =R_5Z with Z = -$CONH_2$, -COOH, -OH

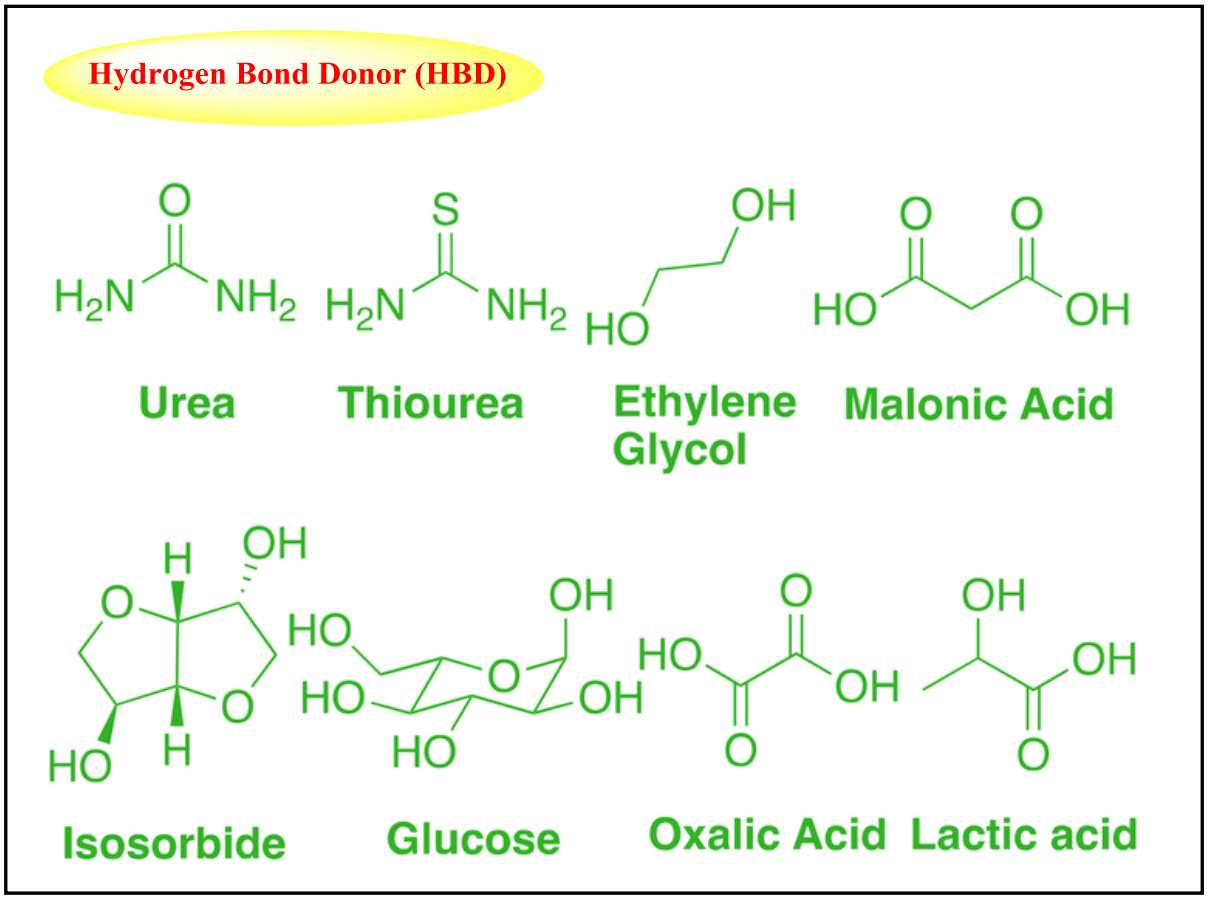

Figure 2: Selective example of hydrogen bond donors employed for the syntheses of DES

Note that the same group also defined a fourth type of DES which is composed of metal chlorides (e.g. ZnCl2) mixed with different HBDs such as urea, ethylene glycol, acetamide or hexanediol (type IV DES). Owing to its low cost, biodegradability and low toxicity, ChCl was widely used as an organic salt to produce eutectic mixtures generally with cheap and safe HBDs such as urea, glycerol, carbohydrate-derived polyols or renewably sourced carboxylic acids. These DESs are attractive since they exhibit similar physico-chemical properties to traditional imidazoliumbased ILs and thus can advantageously replace them in many applications. As compared to traditional organic solvents, DESs are not considered as volatile organic solvents

and not flammable, making their storage convenient. From the view point of green chemistry, these DESs are even more attractive since some of them have been proven to be biodegradable and compatible with enzymes further increasing their interest. Additionally, synthesis of DESs is 100% atom economic, easy to handle and no purification is required, thus making their large-scale use feasible.

From the above discussion, it is clear that DESs possess close physico-chemical properties (density, viscosity, conductivity, among others) to those of conventional ILs. Moreover, like ILs, the physico-chemicals properties of DESs can be tuned almost infinitely by changing the nature of the quaternary ammonium salt and the hydrogen-bond donor, making possible the generation of task-specific DESs. As compared to ILs, DESs have however notable advantages stemming from (1) their convenient synthesis (100% atom economy), (2) their very low price since most of DESs can be prepared from readily accessible chemicals and (3) their low toxicity, especially DESs derived from ChCl and renewable chemicals. Clearly, these notable ecological and economic advantages of DESs now open alternative routes for the emergence of ionic fluids at a larger scale. It should also be noted that although components of DESs are potentially reactive chemicals, their auto-association by a hydrogen bond drastically limits their reactivity, allowing their use in many fields of research. In the field of catalysis and organic synthesis, it is clear that DESs will definitely contribute to the design of eco-efficient processes. In particular, the possibility to (1) selectively and conveniently extract products of the reaction from the DESs phase, (2) adjust the pH of DESs, (3) dissolve not only organic and inorganic salts but also transition metal-derived complexes or nanoparticles and (4) recycle these media is among the most promising advantages of DESs. It is our opinion that development of DESs in the field of catalysis will also be drastically boosted by the need to urgently design innovative processes for the catalytic conversion of biomass. Indeed, imidazolium-based ILs have the unique ability to dissolve large amounts of cellulose and more largely lignocelluloses opening promising routes for the saccharification of biomass. However, it is also clear that the price and toxicity of ILs represent two serious drawbacks that hamper the scale-up of these processes. We are fully convinced that the recent progress made in the field of DESs for the catalytic conversion of carbohydrates will definitely open soon new methodologies for converting lignocellulosic biomass in a more rational way. In the field of material chemistry, it is also apparent that ILs can be advantageously replaced by cheap and safe DESs for the ionothermal synthesis of a wide

range of inorganic materials with different textures and structures. Although a proper selection of the exactly required DESs still remains a big challenge, the above described works have clearly demonstrated that very important materials, from microporous zeotypes to carbon materials, can be synthesized in DESs. The very recent use of DESs for material synthesis demonstrates the exceptional potential of these media for the generation of novel structures and engineered materials. In these syntheses DESs may play different roles such as solvent, structure-directing agent, water inhibitor, reactant for structure crystallization, etc.

Besides excellent dissolution properties for CO2, inorganic salts, and organic molecules, many DESs can also selectively dissolve different metal oxides, which thus provide great potential for the selective recovery of pure metals, especially in electrochemistry. In the particular field of metal electrodeposition, similar results to those reported in conventional ILs were obtained in DESs.

3. Conclusion

Despite all these promising applications, much effort is still required to broaden the exploration of DESs in chemistry. For example, the instability of DESs during electrochemical processes still causes an important concern that requires to be addressed in the future. Viscosity of DESs can also be considered as a serious challenge, especially for heterogeneously-catalyzed processes. In this regard, it makes no doubt that future research will especially focus on DESs with low viscosity. Finally, a specific focus should also be provided to the reactivity of DESs that can, in many cases, lead to generation of undesirable side-products. More than a green medium, DESs can also be considered as a poorly toxic and biocompatible lipotropic agent, thus opening a new strategy for the vectorisation of pharmaceutical ingredients in the human body. This is exciting by the fact that several DESs are suspected to be prepared in living systems and responsible for unexpected mechanisms. However, DESs cannot replace ILs in all fields of chemistry. We are completely assured that low ecological footprint and attractive price will definitely contribute to the industrial emergence of this new medium in a close future.

References

1. B. B. Hansen, S. Spittle, B. Chen, D. Poe, Y. Zhang, J. M. Klein, A. Horton, L. Adhikari, T. Zelovich, B. W. Doherty, B. Gurkan, E. J. Maginn, A. Ragauskas, M. Dadmun, T. A. Zawodzinski, G. A. Baker, M. E. Tuckerman, R. F. Savinell, and J. R. Sangoro, *Chem. Rev*., 2021, **121**, 3, 1232-1285
2. T. E. Achkar, H. G.-Gerges and S. Fourmentin, *Environmental Chemistry Letters*, 2021, **19**, 3397-3408.
3. Q. Zhang, K. D. O. Vigier, S. Royer and F Jerome, *Chem. Soc. Rev*., 2012, **41**, 7108-7146.
4. J. P. Hallett and T. Welton, *Chem. Rev*., 2011, **111**, 3508-3576.
5. J. L. Bideau, L. Viau and A. Vioux, *Chem. Soc. Rev*., 2011, **40**, 907-925.
6. Q. Zhang, S. Zhang and Y. Deng, *Green Chem*., 2011, **13**, 2619-2637.
7. M. J. Earle, S. P. Katdare and K. R. Seddon, *Org. Lett*., 2004, 6, 707-710.
8. M. Deetlefs and K. R. Seddon, *Green Chem*., 2010, **12**, 17-30.
9. N. V. Plechkova and K. R. Seddon, *Chem. Soc. Rev*., 2008, **37**, 123-150.
10. Y. Yu, X. Lu, Q. Zhou, K. Dong, H. Yao and S. Zhang, *Chem.-Eur. J*., 2008, **14**, 11174-11182.
11. K. D. Weaver, H. J. Kim, J. Sun, D. R. MacFarlane and G. D. Elliott, *Green Chem*., 2010, **12**, 507-513.
12. F. Ilgen, D. Ott, D. Kralish, C. Reil, A. Palmberger and B. Konig, *Green Chem*., 2009, **11**, 1948-1954.
13. D. Reinhardt, F. Ilgen, D. Kralisch, B. Konig and G. Kreisel, *Green Chem*., 2008, **10**, 1170-1181.

Chapter: 6

Preliminary study of 2D-Molybednum Disulphide (MoS_2) using Open Source Quantum Espresso Software

Ashwini Kumar

Department of Physics and Electronics

Dr. Rammanohar Lohia Avadh University, Ayodhya, UP

Email: ashwini.physics@gmail.com

Abstract: Two-dimensional (2D) transition metal dichalcogenides(TMDCs) have been attracting a wide range of research interests. Among these, Molybdenum disulfide (MoS2) is one of the most typical TMDCs as the direct band gap of MoS_2 makes it important for research investigations. It has recently gained scientific interests because its 2- dimensional form exhibits great optoelectronic and electrical properties. In this article, a simulation study has been carried to investigate the electronic properties of 2D MoS_2 by using the density functional theory based Quantum Espresso simulation framework. The calculations are performed using self-consistent plane wave pseudopotential total energy method. The convergence study is performed as based on density functional technique implemented in Quantum Espresso simulation code. The atomic positions and cell parameters were fully relaxed. The geometrical structure of MoS_2 was optimized by converging total energy with respect to the Brillouin-zone (BZ) sampling, wave energy cut off, lattice parameters etc. Further, these preliminary results has been presented and discussed.

Keywords– Quantum Espresso, Molybdenum disulfide (MoS_2), Stability curve, electronic properties, density of states (DOS).

Introduction

In recent years, a lot of attention is laid on graphene-like 2D materials to overcome the shortage of graphene and broadening its range of applications for scientific programmes and industrial uses. MoS_2 largely compensate the weakness of gapless graphene, making it potential 2D material to be used in the next generation switching and optoelectronic devices. Recent findings suggest that MoS_2 is a useful material in various fields, including energy conversion, energy storage and hydrogen evolution reaction. Furthermore, its applications in powering nano devices,

solar cell and stretchable electronics are quite promising for future researches in advance science and technology [1-4]. Computational methods are becoming popular to study such molecular structure and their properties. *Ab-initio* methods on typical density functional theory (DFT) offer suitable means for the calculation and characterization of the material's ground-state properties such as atomic configuration and total energies. The density-functional theory (DFT) based simulations of molecules is being widely used as powerful tool for the studying the properties of such materials. These simulation methods are based upon the "plane-wave pseudo potential method", often using ultra softpseudo potentials [5] or the projector augmented wave method (PAW) [6]. DFT-based techniques has been proved to provide the availability of robust and efficient software implementations [7], as is the case for Quantum ESPRESSO, which is an open-source software distribution for electronic-structure calculations based on DFT or many-body perturbation theory, and using plane-wave basis sets and pseudopotentials [8]. MoS_2 belongs to the group-VI transition metal dichalcogenides (TMDC). It consists of hexagonal sheets of chalcogens surrounding an inner layer of metal. It is a layered material and a single layer consists of an S-Mo-S sandwich. In this article, the simulation study of 2D MoS_2isperformed using QE software simulation package in various steps alongwith convergence test. The research article is organized in following manner: Sec. II describes the computational method, Sec. III discusses convergence results with different parameters, Sec. IV contains a summary and conclusions of the research findings.

II. Computational Details:

Quantum ESPRESSO [9, 10] is an open-source implementation of DFT techniques and related codes are available under the GNU General Public License. The 6.4.1 version of Quantum ESPRESSO package is installed on Linux based Ubutnu 14.0 operating system and the calculations were carried out in various steps. The central component of QE is the PWscf module, which performs the self-consistent calculations which is further utilised for further calculations at advanced steps.

Core electrons of the atom are hardly involved in a chemical interaction and are not significantly changed during the process. Thus, if the state of a core electron is considered passive and potential can be approximated by considering only valence electrons. By this, computing resources can be used with minimal effect on the accuracy of the calculation. Due to this fact,

thepseudo potential files are used Core electrons, unlike valence electrons, are hardly involved in a chemical interaction and are not significantly changed during the interaction. Thus, if the state of a core electron is considered as chemically inert, then we can approximate the potential by expressing only for valence electrons. By this, you can efficiently use computing resources with minimal effect on the accuracy of the calculation. The potential created in this process is called pseudo potential. Pseudo potential contains various informations necessary for simulating a system. The complete electronic configuration of Mo is [Kr] $4d^5$ $5s^1$ and S is [Ne] $3s^2$ $3p^4$. The general gradient approximation (GGA) in the Perdew-Burke-Ernzerhof (PBE) form has been used for the exchange-correlation energy. Pseudopotentials files for Mo and S are taken from Pslibrary and has been utilised for calculations. These Pseudopotential file replaces the effects of the core electrons with an effective potential so that the valence states are made smoother for the computational purpose. Atomic positions in the periodic unit cell were allowed to relax and the self-consistency tolerance was set to using Pwscf code. For the claculation purpose, the integration of the Brillouin zone was made on a Monkhorst-Pack grid of k-points in the reciprocal space [11].The aim of this article is to reveal the structural and electronic properties of MoS_2 using Density Functional Theory (DFT) within generalized gradient approximation (GGA) implemented in Quantum ESPRESSO (QE). Further, XCrySDen software was used as a crystalline and molecular structure visualization program to display isosurfaces and contours. It can simultaneously superimpose on crystalline structures. It can also be interactively rotated and manipulated as per requirements.

Results: Performing convergence test calculation prior to principal calculation is a basic requirement of any DFT calculation using DFT code. Proper convergence for the MoS_2 system was investigated by varying wavefunction cutoff, lattice parameter, k-point mesh, and convergence test was performed to quantify their effects on the total calculated energy. The results presented below represent the convergence testes with respect to plane wave kinetic energy cut-off, k-points mesh, lattice parameters.

i. <u>Convergence w. r. t. kinetic energy cutoff:</u>

In Fig. 2, the MoS_2 system was investigated by varying kinetic energy cutoff in order to quantify the effects on the total calculated energy. The optimal value was used for further calculation of the properties of the system.

ii. Convergence w.r.t. k-points:

In Fig. 3, one other convergence parameter is computed for DFT calculations of the MoS_2 crystals as the Brillouin zone sampling K POINTS. Convergence test is performed using k-point meshes ranging from 2×2×2 to 20×20×20 and calculate the total energy for the different k-point meshes is calculated.

iii. Convergence w.r.t. lattice parameter:

In Fig. 4, the equilibrium lattice parameter is obtained by changing lattice parameters with total energy and finding the minima of the curve.

Summary and Conclusions:

In summary, we have investigated the stability study for electronic properties of 2D MoS_2 within the framework of density functional theory by using Quantum Espresso software package. PWscf code was used to perform total energy calculations and convergence study was made with kinetic energy cut off, BZ sampling (k-points) and lattice parameters. Based on these convergence studies, our aim is to study electronic properties of 2D MoS_2 for future research applications.

References:

1. Wi S, Kim H, Chen M, Nam H, Guo LJ, Meyhofer E, et al. Enhancement of photovoltaic response in multilayer MoS_2 induced by plasma doping. *ACS Nano* **2014**; 8: 5270e81.
2. Ding S, Zhang D, Chen JS, Lou XW. Facile synthesis of hierarchical MoS2 microspheres composed of few-layered nanosheets and their lithium storage properties. *Nanoscale* **2012**; 4: 95e8.
3. Li Y, Wang H, Xie L, Liang Y, Hong G, Dai H. MoS2 nanoparticles grown on graphene: an advanced catalyst for the hydrogen evolution reaction. *J Am Chem Soc* **2011**; 133: 7296e9.
4. Wu W, Wang L, Li Y, Zhang F, Lin L, Niu S, et al. Piezoelectricity of single-atomic-layer MoS_2 for energy conversion and piezotronics. *Nature* **2014**; 514: 470e4.
5. A. Dal Corso, Pseudopotentials periodic table: From H to Pu, *Comput. Mater. Sci.* 95, 337 (**2014**).
6. M. Topsakal and R. M. Wentzcovitch, Accurate projected augmented wave (PAW) datasets for rare-earth elements (RE=La–Lu), *Comput. Mater. Sci.*95, 263 (**2014**).
7. D. Vanderbilt, *Phys. Rev. B*41, 7892(R) (**1990**).
8. P. E. Blöchl, Projector augmented-wave method, *Phys. Rev. B*50, 17953 (**1994**).
9. Giannozzi, P.; Andreussi, O.; Brumme, T.; Bunau, O.; Nardelli, M.B.; Calandra, M.; Car, R.; Cavazzoni, C.; Ceresoli, D.; Cococcioni, M. Advanced Capabilities for Materials Modelling with Quantum ESPRESSO. *J. Phys. Condens. Matter***2017**, 29, 465901.
10. https://www.quantum-espresso.org/
11. Evarestov, R.A.; Smirnov, V.P. Modification of the Monkhorst-Pack Special Points Meshes in the Brillouin Zone for Density Functional Theory and Hartree-Fock Calculations. *Phys. Rev*. B **2004**, 70, 233101.

Chapter: 7

An overview of Computational study of Oligosaccharides

Arvind Kumar Tripathi[1] and Vikas Tripathi[2]

[1]Chemist, Uttar Pradesh Rajya Vidyut Utpadan Nigam Limited, UP, India

[2]Research Scientist, FMCG Industry, Gurugram, Haryana, India

E-mail: arvindbhuchem@gmail.com; vikaschembhu@gmail.com

Abstract: Computational chemistry deals with the generation of data which correlate the experimental data on the structures as well as properties of substances. It delivers not only the numerical computation of molecular electronic structures but also molecular interactions. It is one of the most explored mathematical approaches that can be simply designed for execution on a computer. Recent advances in synthetic and analytical techniques have enabled the study of carbohydrates at the molecular level. Recurrent structural features were identified as responsible for particular biological activities or material properties. Here, we discuss the recent achievements in the structural characterization of carbohydrates, enabled by systematic studies of chemically defined oligosaccharides. These findings can guide the development of more potent glycomimetics. Synthetic carbohydrate materials by design can be envisioned. Computational study assists the synthetic chemists in authenticating the presumptions before performing the actual reactions. DFT has been gained the significant exposure towards the successful prediction of numerous molecular properties. Notably DFT provides the better results in comparison to that of traditional correlation strategies.

Keywords: Computational study, glycomimitics, Density Functional Theory (DFT)

Introduction

In nature, carbohydrates are considered as one of the most important member ofbiomoleculefamily. Carbohydrates exist as simple or complex form both, often found individually but sometimesthey are covalently linked to lipids or proteins. Previously the studies on carbohydrates were focused mainly on plant polysaccharides, for example starch,cellulose, pectins, etc., due to their broad applications indaily life. After extensive researches, the

biological importance of carbohydrates in has been well recognized.[1-3] Consequently the emergence of glycobiology as an innovative and challenging research fieldwhich works as the interface of biology as well as chemistry exerting a significant impact on drug development program. The presence of glycoconjugates, such as glycoproteins,glycolipids, and glycosaminoglycans at the surface of cell, expressesmiscellaneous glycosylation exemplars between species which appear to be to be governed by evolutionary selection pressures[4]. Transformations of cell glycosylation are also observed during inflammation, cell activation, and cancer.

Oligosaccharides are considered tohavestructural as well as physical applications.Notably, the oligosaccharides are involved in recognition processes whichdeliver a role in significant biological eventsdue to cell-cell interaction for example cell growth, fertilization, inflammatory processes,bacterial infection, etc. Investigation of the three-dimensional structural framework of oligosaccharides as well asknowledge regarding the molecular basis of their potential towards property of recognition by receptors is highly desirable in the research field of structural glycobiology. Characterization of the three-dimensional structures and understanding ofphysiologicalroles of oligosaccharides is thenecessary conditionto knowmore insightabout the biochemistry of recognition processes which may assist the oligosaccharide-derived drugs design. X-ray crystallography is one of the most authentic techniques for structural elucidation.But this technique is not well applicable for structure determination of oligosaccharides because their crystallization is not so easy.[6]In solution, the flexibility of glycosidic linkages generatesnumber of conformations and they usually coexist in equilibrium. Exploration of other spectroscopic techniques, having suitable time resolution, is required for investigation of the conformational behavior of these molecules.[7-8]Thereforethe concept of molecular modeling of oligosaccharides have been emerged as an salient tool for structural determinations of these molecules.Prof. Lemieux and co-workers have pioneered thefield of molecular modeling.[9] They enriched the area of molecular modeling by developing numerous methodologies[10]which have beenemployed for the characterization of oligosaccharide conformations.

Brief overview ofComputational techniques

As mentioned above, the difficulty of getting proper crystals of carbohydrates beyond a particular size, molecular modelling has proven to be very useful for the elucidation of their structural and conformational characteristics, either alone or in combination with experimental techniques, usually solution state NMR spectroscopy methods. In fact, the combination of modelling/NMR protocols has been extremely useful to deduce the conformational and dynamic properties of free and bound carbohydrate molecules.[11-13]

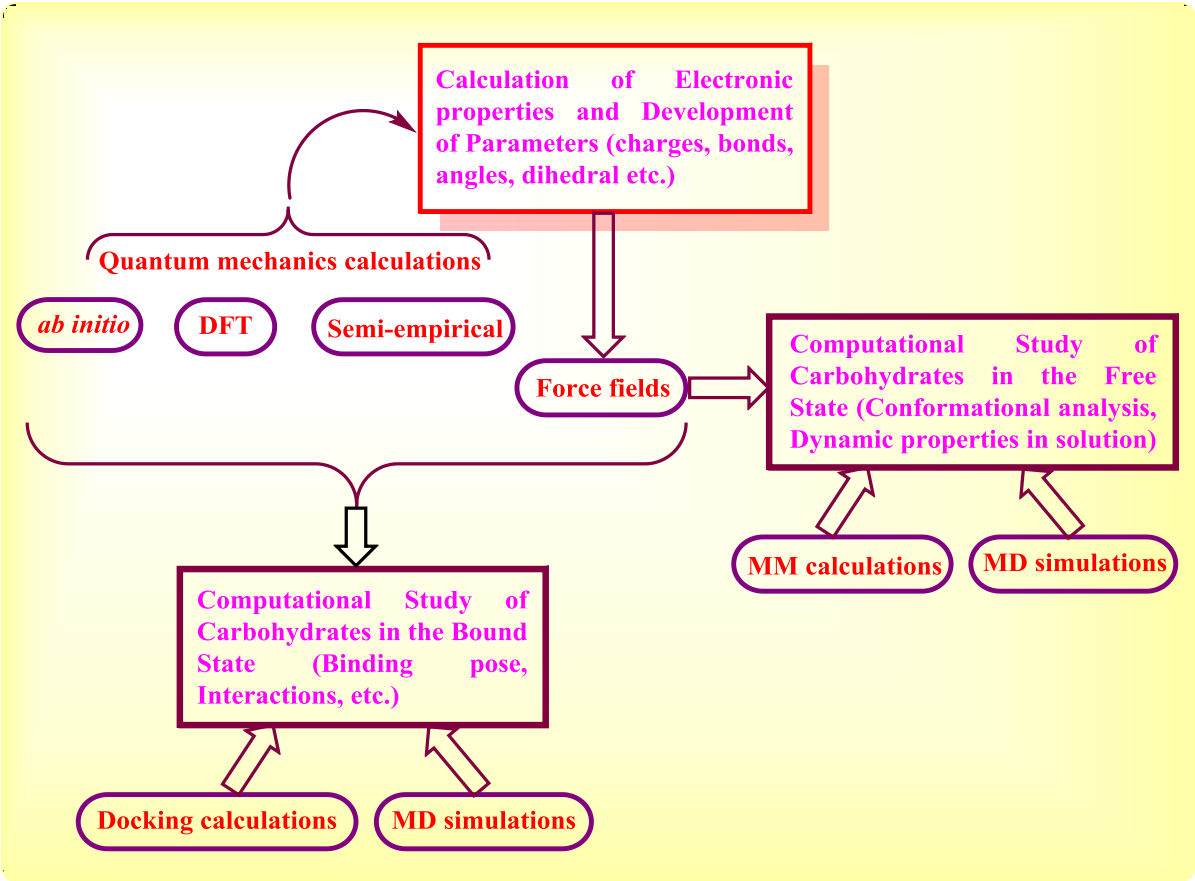

Figure 1: Computational methodologies employed for the study of carbohydrates

Molecular modelling of carbohydrates can be performed at different levels of complexity. Specific structural properties of carbohydrates can be extracted from quantum mechanics (QM) methods, especially those related to electronic features, to study chemical reactions (for instance, by using hybrid quantum mechanics/molecular mechanics QM/MM approaches), and to calculate force constants and atom charges to be used as force field parameters.[14-16] These methods can nowadays be employed even to deal with molecular recognition details. The most

employed protocols for the study of carbohydrates are based on force fields, to perform molecular mechanics (MM) and molecular dynamics (MD) simulations (Figure 1). Research in force field development has been very active in recent years, yielding several high quality force fields able to reproduce dynamic and electronic properties of carbohydrates. In particular, MD simulations are one of the most useful tools to have insights into the conformational dynamics of the system, combined, if available, with NMR experimental information. The interaction of carbohydrates with their receptors can also be performed at different levels of complexity, also using force-field based methods (MM and MD simulations) or quantum mechanics (QM) methods (Figure 1).[17-18]Choosing the appropriate computational method is a key decision in a given study, and it will depend on the properties under investigation, and also on the starting experimental information we have in our hands.

1. *Ab initio* calculations and semi-empirical approaches

Ab initio quantum mechanical (QM) calculation is a very useful tool to investigate molecular properties or describe chemical reaction. This calculation is not based on experimental data but it takes information from the electronic properties of each atom. Depending on the size of a molecule or a system (receptor-ligand) this type of calculation has a very high computational cost, reason why with this technique it is not possible to analyse system with more than few hundred atoms. QM calculations are based on the solution of Schrödinger equation.

Quantum Monte Carlo (QMC) is a very time consuming method, which avoids HF limitations. This method explicitly correlates wave functions and evaluates integrals numerically using a Monte Carlo integration. QMC is probably the most accurate method known today.[19]

Density Functional Theory (DFT) is another QM method, in which the total energy is related to the total electron density instead of the wavefunction. In the Chemical Biology field, DFT methods are very widely used since they combine low computational cost with high accuracy.[20]

2. Docking

Molecular docking is the most common method applied in structure-based design. It provides a model of interaction between two proteins or between a small molecule and a protein

at the atomic level. Computational docking protocols are usually adopted to explore the possible binding poses (and therefore the putative ligand-receptor interactions) of a given ligand within a particular receptor, and to estimate the binding affinity of the resulting complex. The availability of the 3D structure of the receptor (by means of, commonly, X-ray crystallography, NMR spectroscopy, electron microscopy or homology modelling) is required and previous information about the binding site is preferable. The knowledge of the binding site could be deduced by comparison of other related target proteins or through complementary computational studies. For decades, the interaction between protein and ligand has been thought as key-lock system. This model is very easily reproducible with a rigid docking in which both ligand and protein are treated as rigid. With the advent of the induced-fit theory by Koshland, in which a mutual conformation change of both ligand and protein occurs at the moment of the interaction, the global vision of this model evolved.[21] However, these two theories are now better substituted by the concept of conformational ensembles. In a dynamic context, a biomolecule indeed does not have only a fixed conformation. The real three-dimensional structure will be represented by an ensemble of structures which interconvert through dynamic processes. Thus, the study of dynamics and its impact in conformation and molecular recognition is of paramount importance within this field.

3 Molecular Mechanics and Molecular Dynamics Simulations

Molecular Mechanics (MM) or classical mechanics describes molecules as a set of bonded atoms whose interactions can be modelled using standard Newton mechanics instead of QM. The interactions between atoms are modelled with simple parameterized functions based on experimental values or *ab initio* calculations. These functions define the so-called force fields, which are used to easily calculate the energetic function of a system. The molecules are described as an ensemble of spheres representing the atoms and the nuclei positions have a fixed electron distribution, thus simplifying the complexity of the calculations.

4. MM-PBSA/MM-GBSA

Molecular Mechanics-Poisson-Boltzmann Surface Area (MM-PBSA) and the Molecular Mechanics-Generalized Born Surface Area (MM-GBSA) are methods designed to quantitative estimate the binding free energy associated to a complex with implicit solvent. MM-PBSA uses

the Poisson-Boltzmann equation to compute the electrostatic contribution to the free-energy; MM-GBSA uses the Generalized Born approximation, which is an approximate and faster treatment of the Poisson-Boltzmann equation.[22]

5. Virtual Screening

Virtual screening (VS) is a technique used in ligand-based and structure-based drug discovery field to search hits for a specific target or to find new lead compounds. In this Thesis, we have used a receptor-based virtual screening (RBVS) approach, where the availability of the 3D coordinates of the target is mandatory, either from X-ray crystallography, NMR or homology modelling. Prior knowledge about the ligand binding site may help in the identification of proper binders although, in some approaches, the search for novel binding pockets can be an additional interesting -and challenging-element in the drug discovery process.[23-24] Virtual screening aims to reduce the number of compounds that are experimentally screened and to increase the probability to find new active hits. In a structure-based virtual screening there is a sensor which reflects the likelihood of a ligand to bind in the binding site. Than the chemical structures are compared to the sensor and a scoring function is applied to rank them. The comparison of the sensor and the structures can be based on chemical similarity, on pharmacophores and on shape. FLAP and Glide programs have been used to carry out the virtual screening of fragments data base.

6. Conformational analysis

Molecular properties are deeply linked with the three-dimensional structure, or conformation. So the conformational analysis is very important to determine the characteristic related to a molecule. Especially in carbohydrate field this technique helps to understand sugar behaviour in water solution or in complex with a protein. This method could be used either alone or in combination with experimental techniques, usually solution state NMR spectroscopy methods. In fact, the combination of modelling/NMR protocols has been extremely useful to deduce the conformational and dynamic properties of free and bound carbohydrate molecules. In this sense, very useful are carbohydrate databases that collect available NMR data and X-ray experiment of particular dihedral angles, chair conformations and glycosidic linkages.

The conformational search aims to find the minima local energy for a given molecule in order to correlate a molecule with its behaviour. The conformations are usually defined as a

rearrangement of the atoms in space simply rotating single bonds. So the minimization of energy is a crucial step in this protocol. Different techniques can be used to achieve the lowest energy conformer from *ab initio* calculations, semi-empirical methods or MD simulations. Moreover, this technique is also applied for docking studies; in fact it represents the first step of the docking protocol. In this Thesis all the three methods were used. In particular, for *ab initio* calculation DFT methods were applied either in combination with semi-empirical method (in most of the cases MM3*) or/and MD simulation.

7. Homology modelling

The availability of the 3D structure of a given protein is a limiting step in the drug design and development process. Usually, the 3D structures of the macromolecules are elucidated by NMR or X-ray crystallography techniques, and they are deposited in the public database Protein Data Bank (PDB).[25] When the 3D structure for a protein of interest has not been resolved by experimental techniques, homology modelling is very powerful to predict the structure of a protein. In order to build a homology model, the availability of the experimental 3D structure (template) or multiple structures is required. Starting from the protein sequence (target) available on the Universal Protein Resource database (UNIPROT),[26] a sequence alignment with the template is performed. This procedure is online accessible by means of Basic Local Alignment Search Tool (BLAST).[27] The scoring of BLAST provides to estimate the quality of the sequence alignment using the BLOSUM62 (BLOck SUbstitution Matrix).[28] In the score assignment, different parameters are taken into account such as the percentage of identity between the searched protein and the template (a good model has minimum 30% of the percentage identity)[29] and the percentage of query cover. To build a homology model three different protocols can be applied: *ab initio*calculations, fold recognition and comparative modelling. With *ab initio* is possible to build small peptides. Fold recognition (or threading) protocol recognizes specific sequences whose folding motif is already know from experimentally elucidated 3D structures. With comparative modelling, the templates from the PDB are assumed to be homologous to the target and the templates guide the building of the three-dimensional model. In this Thesis, we uses the Phyre2 web server,[30] which uses an ensemble fold recognition method with an in-house algorithm.[31] Once the model is built, a subsequent refinement step, especially for the side chain, is necessary. This step can be carry out by MD simulation, restraining the Cα of the backbone.

The novel innovations in computational power now offers for the simulation of carbohydrates in their original conditions, i.e., solvated in water or in organic solvent, in concentrated solution, or in the binding site of a protein receptor.

The last two decades have witnessed tremendous advances in the elucidation and understanding of the conformations and dynamics of oligosaccharides thanks to the technical developments in nuclear magnetic resonance (NMR), X-ray diffraction, and computer modeling methods. It is the aim of the present paper to review the significant contributions in the field, restricting the examples to some carbohydrate molecules that are considered to possess a significant biological function. We focus essentially on molecules belonging to the class of histo-blood group antigens and to the glycosaminoglycan family for which a range of conformational characterizations has been reported, in turn providing a consistent understanding of the conformation and conformational changes that these molecules undergo as a function of their chemical and biological environment. Obviously other biologically active oligosaccharides and glycoconjugates have been reported. But none of these has been sufficiently well characterized, in terms of conformation, to be included, thus avoiding the risk of transforming this paper into a catalog. As for the different concepts and tools underlying the assessment of the structural and dynamics features of oligosaccharides, they will be presented using the most significant scientific contribution, whether the studied molecules belong to the classes of biologically active oligosaccharides defined above.

Theoretical aspect of DFT (Density Functional Theory)

Density functional theory (DFT) is a type of electronic structurecalculation that has rapidly gained popularity.[32] DFT is a computational quantum mechanical modelling method used in physics, chemistry and materials science to investigate the electronic structure (or nuclear structure) (principally the ground state) of many-body systems, in particular atoms, molecules, and the condensed phases. Using this theory, the properties of a many-electron system can be determined by using functionals, i.e. functions of another function. In the case of DFT, these are functionals of the spatially dependent electron density. DFT is among the most popular and versatile methods available in condensed-matter physics, computational physics, and computational chemistry.

Electronic structure calculations serve an important role in the understanding of chemical structure and reactivity. The release of user-friendly, commercial electronic structure programs has led to increased access to the techniques of computational chemistry by undergraduate students. Unfortunately, these programs have been both a boon and a curse to the understanding of electronic structure theories by students. The programs have become so easy to use that novice users may misuse and over extrapolate the output of these programs. Novice chemists may not appreciate that fact that approximate computations can give useful insight into experimental results if you understand what a particular computation tells you and what it does not. Density functional theory (DFT) is a type of electronic structure calculation that continues to gain popularity. A deep understanding of DFT is possible for junior and senior undergraduates in physical chemistry courses as well as beginning graduate students. To the best of our knowledge, all modern physical,[33] quantum,[34] and computational[35] chemistry texts lack clear illustration of the implementation of density functional theory by specific examples. In general, quantum concepts are best understood by examining the full treatment of simple systems by hand. This technique can give clear insight into the manner in which the theory is implemented in programs. This Journal has published a number of articles that give step-by step details of Hartree-Fock calculations on small atoms and molecules[36] as well as articles on a range of other aspects of computational chemistry.[37-38]Some important types of modern calculations are Hartree-Fock (HF), Møller-Plesset perturbation theory (MP) and configuration interaction (CI), and density functional theory (DFT) calculations.[34,39] The main practical difficulty for all electronic structure theories is the proper treatment of electron-electron interactions in species that contain two ormore electrons. HF, MP, and CI calculations rely on the computation of the atomic or molecular wave function, whereasDFT requires computation of the total electron density andtechnically does not require a wave function. In practice,however, DFT generally uses a wave function to compute some parts of the energy and the electron density to compute other parts of the energy. The total electron density and the normalized wave function can be interrelated because the total electron density is the absolute value of the square of the normalized wave function divided by the number of electrons. Hartree-Fock treats the electron−electron interactions in a very approximate way and, therefore, is the least accurate of these four methods. HF theory has a number of well-established shortcomings and this method alone is generally not accurate enough to study most chemical reactions.[34] MP and CI, which build upon the HF

calculation, provide very accurate electronic energies for small atoms and molecules when using very large basis sets, but the methods are too computationally expensive to apply to larger atoms and molecules. Modern implementations of DFT can provide much higher accuracy than HF calculations at a lower computational cost. The low computational cost of DFT has led to a steady increase in the use of density functional theory for the study of larger molecules.[35,39]

Conclusion

In the past few years we have seen that theoretical and experimental studies are becoming mutually reliant for the elucidation of structural and dynamical data in the oligosaccharide field. The next frontiers will most likely focus on the problems associated with hydration. Molecular dynamics simulations of carbohydrates with the inclusion of explicit water molecules has proven to be a powerful tool for reconciling theoretical and experimental conformational data.64 Furthermore, calculation of free-energy perturbations is a promising approach for the prediction of oligosaccharide- receptor binding affinities.243-244 Detailedanalyses of hydration patterns for carbohydrates in water245 or in aqueous solvent mixtures246 can now be undertaken. Understanding the role of water as a structural but dynamic element of the solvated oligosaccharide will allow modeling of the interaction between charged carbohydrates and counterions and for this new and improved experimental and theoretical procedures will be needed. It is only by the merging of theory and experiment that understanding of the role of water in the conformation and dynamics and ultimately the biology of many oligosaccharides will be achieved.

References

1. A. Kobata, *Eur. J. Biochem*., **1992**, 209, 483.
2. A. Varki, *Glycobiology*, **1993**, 3, 97.
3. R. A. Dwek, *Chem. Rev*., **1996**, 96, 683.
4. P.Gagneux and A. Varki, *Glycobiology* **1999**, 9, 747.
5. H.Lis, and N. Sharon, *Chem. Rev*., **1998**, 98, 637.
6. S.Perez, C.Gautier, A. Imberty, In Oligosaccharides in Chemistry and Biology: A Comprehensive Handbook; Ernst, B., Hart, G., Sinay, P., Eds.; Wiley/VCH: Weinheim, **2000**, 969-1001.
7. T.Peters and B. M. Pinto, *Curr. Opin. Struct. Biol*. **1996**, 6, 710.
8. K. G.Rice, P.Wu, L.Brand, Y. C. Lee, *Curr. Opin. Struct. Biol*. **1993**, 3, 669.
9. R. U.Lemieux, K.Bock, L. T. J.Delbaere, S.Koto and V. S. R. Rao, *Can. J. Chem*. **1980**, 58, 631.
10. R. J. Woods, In Reviews of Computational Chemistry; Lipkowitz, K., Boyd, D. B., Eds.; VCH Publishers: New York, **1996**; 9, 129-165.
11. P.Vidal, V.Roldos, C.Fernandez-Alonso Mdel, B.Vauzeilles, Y.Bleriot, F. J.Cañada, S.André, H.-J.Gabius, J.Jiménez-Barbero, J. F.Espinosa and S.Martin-Santamaria, *Chem. Eur. J.*, **2013**, 19 (43), 14581-14590.
12. S.Martin-Santamaria, J.Jiménez-Barbero, H.-J.Gabius, *Pure Appl. Chem*., **2012**, 84 (1), 49-64.
13. N.Sapay, A.Nurisso, A.Imberty, *Methods Mol. Biol*., **2013**, 924, 469-483.
14. K. N.Kirschner, A. B.Yongye,S. M.Tschampel, J.González Outeiriño, C. R.Daniels, B. L.Foley, R. J.Woods, *J. Comput. Chem*. 2008, 29 (4), 622-655.
15. O.Guvench, E.Hatcher, R. M.Venable, R. W.Pastor, A. D.MacKerell, *J. Chem. Theory Comput*., **2009**, 5 (9), 2353-2370.
16. R. D.Lins and P. H.Hunenberger, *J. Comput. Chem*., **2005**, 26 (13), 1400-1412.
17. T.Ishida, *J. Phys. Chem. B* **2010**, 114 (11), 3950-3964.
18. M. C.Miller, J. P.Ribeiro, V.Roldos, S.Martin-Santamaria, F. J.Cañada, I. A.Nesmelova, S.André, M.Pang, A. A.Klyosov, L. G.Baum, J.Jiménez-Barbero, H.-J.Gabius and K. H. Mayo,.*Glycobiology* **2011**, 21 (12), 1627-1641.

19. B. L.Hammond, W. A.Lester, P. J.Reynolds, Monte Carlo methods in ab initio quantum chemistry. World Scientific: **1994**; Vol. 1.
20. E. K.Gross, R. M.Dreizler, Density functional theory. Springer Science & Business Media: **2013**, Vol. 337.
21. D. E.Koshland, The key-lock theory and the induced fit theory. *Angew. Chem. Int. Ed*. **1995**, 33, 2375-2378.
22. T. Hou, J. Wang, Y.Li and W.Wang, *J. Chem. Inf. Model.* **2011,** *51* (1), 69-82
23. L. Pérez-Regidor, M. Zarioh, L. Ortega, S. Martín-Santamaría, *Int. J. Mol. Sci*. **2016**, 17 (9), 1508.
24. J. H.Haga, K.Ichikawa and S. Date, *Curr. Pharm. Des*. **2016**, 22 (23), 3576-3584.
25. Protein Data Bank. http://www.rcsb.org (accessed March 29, **2017**).
26. Universal Protein Resource (UNIPROT). http://www.uniprot.org.
27. Basic Local Alignment Search Tool (BLAST). https://blast.ncbi.nlm.nih.gov.
28. S. F. Altschul, T. L.Madden, A. A.Schäffer, J. Zhang, Z. Zhang, W. Miller and D. J. Lipman, *Nucleic Acids Res*. **1997**, 25 (17), 3389-3402.
29. L.Bordoli, F.Kiefer, K.Arnold, P.Benkert, J.Battey and T.Schwede, *Nat. Protoc*., **2009**, 4 (1), 1-13.
30. L. A.Kelley, S. Mezulis, C. M. Yates, M. N.Wass and M. J. E. Sternberg, *Nat. Protocols* **2015**, 10 (6), 845-858.
31. R. M. Bennett Lovsey, A. D.Herbert, M. J. Sternberg and L. A. Kelley, *Proteins: structure, function, and Bioinformatics* **2008**, 70 (3), 611-625.
32. K. A. Baseden and J. W. Tye, *J. Chem. Educ*. **2014**, 91, 12, 2116-2123.
33. A. Cooksy, Physical Chemistry: Quantum Chemistry and Molecular Interactions; Prentice Hall: Upper Saddle River, NJ, **2013**.
34. P. W.Atkins and R. S. Friedman, Molecular Quantum Mechanics, 5th ed.; Oxford University Press: New York, NY, **2005**.
35. A. Hinchliffe, Molecular Modelling for Beginners, 2nd ed.; John Wiley & Sons Ltd: West Sussex, United Kingdom, **2008**.
36. A. M.Halpern, E. D. Glendening, Exploring the Nature of the H_2 Bond. 2. Using *Ab Initio* Molecular Orbital Calculations to Obtain the Molecular Constants. *J. Chem. Educ*. 2013, 90, 1459-1462.

37. T.Simeon, C. M.Aikens, B.Tejerina and G. C. Schatz, *J. Chem. Educ*. **2011**, 88, 1079-1084.
38. C. D. Montgomery, *J. Chem. Educ*. **2013**, 89, 1396-1400.
39. D.Sholl and J. ASteckel, Density Functional Theory: A Practical Introduction; John Wiley & Sons, Inc.: Hoboken, NJ, 2009.

Chapter: 8

Impact of alky chain length of *N*-(4-n-Alkyloxybenzalidene) 4′-n-Alkylaniline on dielectric parameters

Ragini Tripathi[1], Avneesh Mishra[2], K. N. Singh[3], P. R. Alapati[4] and Ravindra Dhar[5]

[1]Department of Physics, Sunbeam Women's College Varuna-221002, Varanasi India

[2]Dept. of Applied Sciences & Humanities, Future Institute of Engineering and Technology, Bareilly-243202, India

[3]Department of Physics, Manipur College, Imphal-795001, India

[4]Ghani Khan Choudhury Institute of Engineering and Technology, West Bengal- 732141, India

[5]Soft Material Research Laboratory, Centre of Material Sciences, Institute of Interdisciplinary Studies, University of Allahabad, Allahabad-211002, India.

Abstract: Impact of alkyl chain length on Schiff's base liquid crystalline compounds of N-(4-n-Pentyloxybenzalidene) 4′-n-Alkylaniline, 5O.m (m = 5 and 6), series have been measured with the help of thermodynamic, optical and dielectric studies. The dielectric properties have been studied by the impedance spectroscopy in the frequency range of 1 Hz to 10 MHz and results explained on the basis of Maier and Maier equation. Relaxation frequencies corresponding to the fluctuation of molecules about their short axes lie below 10 MHz and obey the Arrhenius law. The effect of odd-even alkyl chain on relaxation frequency is also defined. Effect of tilt angle on relaxation frequencies and pretransitional effect is also compared. Role of alkyl chain length on variation of ionic conductivity is also determined.

Keywords: Dielectric spectroscopy, dielectric anisotropy, relaxation frequency, odd-even effect, pretransitional effect, ionic conductivity.

Introduction

The physical properties of liquid crystals (LCs) are very much affected with a slight variation in molecular structure. Spectacular effects on the polymorphism of LCs are observed with the minor changes in the rigidity or flexibility of the molecules [1-3].Therefore, in order to observe the effect of variation of alkyl chain length on dielectric parameters, a comparative low frequency dielectric study of two Schiff's base nO.m liquid crystalline compounds: Pentyloxy

benzylidene pentylaniline (5O.5) and Pentyloxy benzylidene hexylaniline (5O.6) has been made.Both the compounds are having negative dielectric anisotropy ($\Delta\varepsilon<0$); it means the transverse dipole moment (μ_t) is of course markedly greater than the longitudinal (μ_l) one [4].If the constituting molecules of a LC compound possess a dipole moment, then the rotational dynamics of the molecules can be very well understood with the help of dielectric spectroscopy. The dielectric studies provide the valuable information regarding the response of dipoles to the external stimulus. The frequency- and temperature- dependent dielectric studies are very valuable tools to get information not only about bulk properties but also about molecular parameters, their mutual association, and rotation under applied electric field [5-7].

Generally, the achiral rod-like LC molecules possess two principal relaxation processes: the rotation of the molecules around its short axis (the low frequency process) and the rotation around long molecular axis (the high frequency process). Both these relaxation process resultswith thenon-zero projection of the dipole moment on the principal inertia moment axes [8]. There are several factors that affect the dielectric properties of LC materials, such as the position and the value of the dipole moment in the molecule, the ratio between the longitudinal to transverse dimensions of molecule and the type of molecular arrangements in a LC phase. Moreover, the lengths and flexibility of the terminal groups and the rigidity provided by the molecular cores are found to be the most important structural factors [9]. The influence of increasing alkyl chain length on physical properties and molecular dynamics of LC compounds is given importance in this paper.

In literature, the dielectric studies of nO.m are scarce, that too of 5O.m series. Bata et al. have reported the study of static dielectric permittivity and relaxation process in different phases of 5O.6 [10]. Also, in one of the paper Benguigui have reported the dielectric relaxation studies of three members of 5O.m series (m = 6, 7 and 8) based upon the nematic long-range parameter [11]. Whereas in another study Benguigui had measured the dielectric anisotropy of two members of 5O.m series (m = 7 and 8) and interpret their behaviors with the help of dipole-dipole correlations [12].

Urban et al have reported the dielectric studies of three members of nAOB (4,4’-di-*n*-alkyl-azoxybenzenes) and nOAOB (4,4’-di-*n*-alkoxyazoxybenzenes), n = 5, 6 and 7. They found that with the increase in chain length of all substances the permittivity component decreases

systematically [4]. Such results were also reported by J. Czub et alwhen studied for few smectogenic members of nCB(4′-alkyl-4-cyanobiphenyl) homologous series [13]. While discussing about the compounds that belongs to similar homologous series, the odd-even effect play a significant role.With the increase in the end chain length, the physical properties (e.g., nematic-isotropic transition temperatures (T_{NI}), order parameter, the transition entropy and relaxation frequency) show a pronounced change [14-15].Marcelja has made a qualitative calculation of the contribution of the end-chain to the ordering and suggested that axial polarizabilities play a dominant role in explaining odd-even effect. The *cis*- and *trans*-like alternating dipole configuration projected onto the length of the molecule with increasing end chain length seems to be responsible for odd-even effect in a homologous series [16].

Experiment techniques

The compounds 5O.5 and 5O.6 was synthesized following the procedure described earlier [17] from the condensation of n-pentyloxybenzaldehyde and respective n-alkylaniline in absolute ethanol.The LC compounds were filled in the dielectric cells by capillary effect at a temperature higher (~10°C) than the nematic-isotropic (N-I) transition temperature. The cells consisted of two glass substrates coated with conducting ITO layers. To obtain planar alignment of the composite the conducting layers were treated with silane and polymide nylon 6/6. The homeotropic alignment of the composite was obtained by covering the ITO layers with HTAB solution. In these cells spacer of 25 µm were used. The thermodynamical study of both the compounds has been carried out with the help of DSC of NETZSCH model-200-F3-Maia. Optical textures were examined using a polarizing thermal microscope (PTM) of Censico (model 9660). Dielectric measurements were made using a Newton's Phase Sensitive Multimeter (model PSM 1735) in combination with an Impedance Analysis Interface (IAI model-1257). The temperature was controlled with the help of a temperature controller of Instec (model mK1000) attached with a hot stage (model HS-1) having an accuracy of ±0.1°C and a temperature resolution of 3mK. The complex dielectric function of the pure and dispersed samples (*='-iε") were measured in the frequency range 1 Hz-10 MHz.

Results and Discussions

The presence of five different phases (i.e. N, SmA, SmC, SmF and SmG) in 5O.5 and six phases (i.e. N, SmA, SmC, SmB, SmF and SmG)in 5O.6 has been confirmed with the help of optical

and thermodynamical studies. The corresponding phase sequences and transition temperatures obtained with the help of differential scanning calorimetry (DSC) at the scan rate of 2.5 °C/min are mentioned in Table 1.The values are found to be in good agreement with that mentioned in literatures [18,11]. The molecular structure of 5O.m (m = 5 and 6) is shown in Figure 1. Both the compounds consist of two regions: one is the mesogenic core formed by two phenyl rings along with –C(H)=N– linkage and another is the alkyl segments constituted by two terminal alkyl chains. The only difference between the molecular structures of both compounds is an addition CH_2group in terminal alkyl chain of 5O.6. Since, the apparent difference between them is very minimal but, its impact is not easier to understand. The variation in terminal chain lengths shows its effect on phase sequences exhibited by the compound, thermodynamic parameters (such as latent heat, specific heat, etc.) and different dielectric parameters (such as permittivity, loss, relaxation frequency, etc.). For instance, just by increasing one CH_2 group in the terminal alkyl chain of 5O.5 results in an orthogonal phase (SmB) in between two tilted phases (SmC and SmF) [19]. Singh et al reported that with an increase in alkoxy chain length from n=6 to n=7 in nO.m series, the dielectric anisotropy switches from negative to positive [20].

The experimentally measured permittivity and loss data are fitted with the help of generalized form of Cole-Cole equation [21]. Variations of the dielectric permittivities (' and '), with the measuring electric field parallel and perpendicular to the director, respectively, for 5O.5 and 5O.6 as a function of temperature are shown in Figure 2. The data presented are at 100 kHz (they do not represent the static values), as they are free from parasitic affects.It can be observed from Figure 2that both parallel and perpendicular components of permittivity are marginally less in 5O.6 than 5O.5.The studies conducted on 5O.7 and 5O.8 by Benguigui also shows that the permittivity components in 5O.8 are less than 5O.7 [12]. Thus on the basis of previous reported values and our present studies it can be concluded that with the increase in alkyl chain length of 5O.m series the permittivity components decreases. Figure 3 shows the variation of dielectric anisotropy ($\Delta\varepsilon$) with temperature for both compounds. It is evident from Figure 3that with the increase of alkyl chain length the value of dielectric anisotropy decreases (in terms of magnitude) up to a particular temperature (~51.0°C) and then increases in a certain temperature range (~50.0°C to 40.0°C) and then the anisotropy again decreases.The major decrease in dielectric anisotropy was noticed in nematic phase and slight decrease was observed in SmA and SmC

phases. The results obtained for N phase can be explained with the help of Maier and Maier theory [22],

Δε=NHFΔα-F2kT21-3cos2S(1)

whereN is the number density of LC molecules (the number of molecules per unit volume) and S is the order parameter. Δ is the anisotropy of the polarizability, is the resultant dipole moment of the molecules and is the angle between the dipole moment and long axis of the molecule.F is the feedback factor and H=3(0)/(20+1). From equation (1), it is evident that as number of molecules per unit volume decrease, the value of dielectric anisotropy also decreases. With the elongation of alkyl chain length the number of molecules per unit volume decreases and hence dielectric anisotropy decreases in the N phase [23].

However, for smectic phases no such generalized theory has yet been developed. The dielectric data of the SmA phase are sometimes explained (at least qualitatively) by few authors [24-26] with the extension of Maier and Maier theory [22]. For SmA and SmC phase, the dielectric permittivities (' and ') can be written as [24-26],

'-'=3⟨'0⟩2⟨'0⟩+⟨'⟩N2cos20kT1+g (2)

and,

'-'=3⟨'0⟩2⟨'0⟩+⟨'⟩N2sin22ε0kT1+g(3)

whereg=glS22cos2kT and g=gtS232sin22kT, and is the angle between net dipole moment (μ) and the long axis of the molecule.

From equations (2) and (3), dielectric anisotropy (Δε) can be written as:

Δ'='-'=3⟨'0⟩2⟨'0⟩+⟨'⟩N20kT1+gcos2β-121+gsin2 (4)

It can be observed from above equation (4) that as number of molecules per unit volume decreases in SmA and SmC phase, dielectric anisotropy decreases. Therefore, due to the elongation of the chain length, the number of molecules per unit volume decreases and so dielectric anisotropy also decreases similar to nematic case.

Variation of relaxation frequencies (f_R) with inverse of temperature are shown in Figure 4 for 5O.5 (mode M2) and 5O.6. The inset of Figure 4 shows that 5O.5 exhibits three different modes of relaxation. Whereasfrom Figures 4 it can be observed that 5O.6 exhibits only one mode of relaxation. The relaxation frequency corresponding to different modes of relaxation shows the common behavior. With the increase of temperature the relaxation frequency increases for both members of the homologous series. Relaxation frequencies (f_R) follow Arrhenius behavior. In 5O.5 the three observed modes of relaxation i.e. M1, M2 and M3 are related with three different phenomenons. The presence of mode M1 has been attributed to be due to interfacial polarization effect, whereas M3 is related with tilt fluctuations of the cluster of molecules that forms cybotactic clusters. The common mode M2 that has been observed in both the compounds is characteristic of the mode due to the fluctuation of director about short axes. The detail explanation of modes observed in 5O.5 has been reportedearlier [17].

Let us first discuss the effect of increasing alkyl chain length on the relaxation process occurring due to the fluctuation of director about short axes (mode M2). It can be observed from Figure 4 (inset) that the value of $f_R$of mode M2 in N, SmA and SmC phases of 5O.5 falls in the range of 1.81 kHz-9.86 kHz, 10.5 kHz-9.19 kHz and 8.96 kHz-8.57 kHz, respectively. However, Figure 4again shows that in case of 5O.6 the range is 2.35 MHz-1.05 MHz, 729.54 kHz-370.33 kHz and 326.95 kHz-350.36 kHz for the same mode M2 in N, SmA and SmC phases respectively. Therefore, with these mentioned values it is clear that with the increase in the alkyl chain length, relaxation frequency corresponding to mode M2 increases.In most of the cases, particularly in the N phase, with the increase of molecular length in a homologous series the f_R is expected to decrease, since a larger orienting force is experienced by a longer molecule due to increasing value of nematic potential with increasing molecular length. Such a strong dependence of the f_R on the length of the molecules corresponding to the rotation around short axis is a common known phenomenon for LCs [27-29]. Padmajarani et al have reported that with the increase of alkyl flexible chain in 8O.m and 10O.m relaxation frequency decreased in SmA and SmC phases. Also, they reported that even members of nO.m series were found to exhibit relaxation frequencies almost three times stronger than the other compounds [15]. Therefore, the odd-even effect as detailed by Marcelja [16] seems to be the supportive explanation for the major difference observed in the relaxation frequencies (of mode M2) in N, SmA and SmC phases of 5O.5 and 5O.6.

Further explanation of our findings can be given on the basis of molecular theory proposed by Edwards and Madden for the dielectric permittivity of the nematic liquid crystals [31].According to the theory, f_R corresponding to rotation about the short axes of the molecules is given by:

fR=fDg'⟨'0⟩-1'-1(5)

wherefD is the usual Debye relaxation frequency, g' is the retardation factor introduced by Maier and Maier, which is a consequence of nematic potential, ' is the static dielectric permittivity parallel to the director, and ⟨'0⟩ is the mean dielectric permittivity.As observed from Figure 4 the value of f_R (mode M2) in N phase increases with an increase of the alkyl chain.In our previous discussion it has been explained that with an increase in the molecular length (due to increase in the chain length), the number of molecules per unit volume decreases (*N*), hence ' also decreases (see equation (2)).Therefore, due to this fact f_R seems to increase with an increase in the alkyl chain length, as evident from equation (5).Here one question arises that due to the decrease of *N*, ⟨'0⟩ will also decrease and that will cancel the effect of '. But, as the studied compounds have negative dielectric anisotropy so ⟨'0⟩>'. Therefore, numerator component in equation (5) will be less dominating as compared to denominator and hence a marginal increase in f_R with increasing chain length is expected and the same is clear from Figure 4.

Aboveequation (5) can be employed in case of SmA phase also [31-32].Due to the layering of molecules in SmA phase the anti-parallel dipole correlations between the longitudinal components of the dipoles increase and thus g' decreases while going from N to SmA phase. Hence, because of this fact the relaxation frequencies of the SmA phase are found to be lower than that of the N phase of the same compound.As SmC resembles more alike SmA, so the explanation for increase in f_R (mode M2) of SmC phase can be given in similar way as above.

Figure 5(inset) shows the variation of dielectric strength '='0-' with temperature for 5O.5. Also Figure 5 shows the variation of dielectric strength with temperature for 5O.6 along with mode M2 of 5O.5. After comparing the dielectric strength of common mode between both compounds (mode M2), it can be viewed that the value of dielectric strength decreases with the increase in the alkyl chain length.For 5O.6 it is observed that in the vicinity of SmA-N transition, ' decrease with increase of the temperature, however in SmA and SmC phase, ' is almost

independent of the temperature.A slight variation of ' with temperature was observed in SmB, SmF and SmG phases. Whereas in case of 5O.5, ' shows strong dependency on temperature.

Now, in the following part the absence of relaxation modes M1 and M3 in 5O.6 shall be discussed.The presence of modes M1 and M3 in 5O.5 was already explained. The mode M1 was apparently observed in 5O.5 due to Maxwell-Wagner-Sillars (MWS) effect [33]which is mainly associated with ionic conduction and interfacial polarization.The understanding of this phenomenon is important from application point of view, for example an enhanced dielectric tunability could be achieved due to interfacial polarization [34-35]. This effect is basically a thermally activated process that arises due to thermal generation of ionic charges at each interfacial layer.Figure 6 shows that the ionic conductivity and hence the concentration of ions in 5O.6 is less than that in 5O.5. Therefore, due to low concentration of ions in 5O.6 the interfacial polarization relaxation (mode M1) does not appear.

The pre-transitional phenomenon and also the presence of cybotactic clusters were reported in both of the two compounds.But their magnitude is not known. In the SmC phase of 5O.5 a large variation of tilt angle (0° to 23°) was reported within a temperature range of ~ 4.0 °C [18].Due to this wide variation of tilt angle within a small temperature range, the molecules seem to be tilted to some extent in SmA (de Vries character) and also in N phases (due to pre-transitional effect).Thus, mode M3 in 5O.5 originates due to the tilt fluctuation of the cluster of molecules, which is already discussed in detail.On the other hand, the reported tilt angles in SmC phase of 5O.6 are ~14° within a temperature range of ~1.5°C [18]. Consequently, due to the less tilt fluctuation of molecules the relaxation process corresponding to mode M3 does not appear in 5O.6.The increased molecular length of 5O.6 further hinders the tilting of the molecules.Moreover, the order of N-SmA transition in 5O.5 is second order while it is weakly first-order in 5O.6 [18].Therefore, it can be assumed that in 5O.5 the smectic like ordering in N phase is stronger than in 5O.6.

In 5O.5, the relaxation mode M2, which is due to rotation of molecules around short axes, appears in N phase only few degrees before transition to SmA and continues till the lowest temperature of study in SmG phase.This is so because in N phase the relaxation process corresponding to mode M1 and M3 dominates over the relaxation process related to mode M2 [9].As soon as mode M1 disappears in low temperature of N phase and the dielectric strength of

mode M3 decreases, M2 appears in N phase of 5O.5. Whereas in 5O.6, relaxation mode M2 is the only process that exists, therefore it appears just after the transition to N phase. It can be seen from Figure 3.13 that a pronounced jump appears in f_R at SmC-SmB transition in 5O.6. Whereas, in 5O.5 no such jump was observed during the SmC-SmF transition. As both SmC and SmF are tilted and 2D phases due to which molecules experienced less potential barrier. While, during the SmC-SmB transition in 5O.6, the arrangement of molecules get transformed from a 2D-tilted phase to a 3D-orthogonal phase [36]and the ordering is changed within the layers.

Conclusions

The effect of alkyl chain length on dielectric studies of two members of 5O.m series in the isotropic and different LC phases can be concluded in these few points:

1. The interfacial polarization relaxation is observed in isotropic and N phase of 5O.5, however due to the low concentration of ions in 5O.6 this relaxation process does not appear.
2. In every phase (N, SmA, SmC, SmB, SmF and SmG) of 5O.6 only one relaxation process related to the molecular rotations around the short axes was observed. Whereas, in 5O.5 three different relaxation process of different origins was observed.
3. The increase of alkyl chain length by just one CH_2 group results in an increase of relaxation frequency and decrease of dielectric strength.
4. Variations of relaxation frequency with alkyl chain reveal an odd-even effect. Even numbered 5O.m members are found to bear stronger relaxation frequencies than odd members.
5. The SmA phase of 5O.5 exhibit de Vries character, but no such effect was observed in 5O.6. The increase of alkyl chain length decreases ionic conductivity.

Acknowledgments

PRA acknowledeges the funding provided by SERB, Ministry of Science and Technology, Government of India (Sanction order No. SB/52/CMP-093/2013), Dated: 10/09/2014.

References

1. G. W. Gray,Molecular Structure and the Properties of Liquid Crystals **(**Academic Press Inc., New York) (1962)
2. G. W Gray, Advances in Liquid crystals, (Academic Press Inc., New York) Vol. **2** (G.H. Brown, Ed.) (1976)
3. G. W. Gray, Liquid Crystals and Plastic Crystals (Ellis Harwood, Chichestor, England) Vol.1, Chapter.4.1 (G W Gray and PA. Winsor, Eds.)(1974)
4. S. Urban, J. Czub, and B. Gestblom, Comparison of Dielectric Properties of Three Alkyl and Alkoxy Azoxybenzenes (nAOBs and nOAOBs, n = 5, 6, 7) in the Isotropic and Liquid Crystalline Phases, Z. Naturforsch. 59a, 674 (2004)
5. G. Maier, K. Sackmann, and J. G. Gragmaier, Applications of Liquid Crystals (Springer) p. 150 (1975)
6. G. W. Gray, Advances in Liquid Crystal Materials for Applications, BDH Monograph (1978)
7. W. H. De Jeu, Dielectric Permittivity of Liquid Crystals, Solid State Physics Suppl., 14, 109 (1978)
8. J. Jadżyn, G. Czechowski, R. Douali, and C. Legrand, On the molecular interpretation of the dielectric relaxation of nematic liquid crystals, Liq. Cryst. 26 (11), 1591-1597 (1999)
9. D. Demus, Handbook of liquid crystals, (Wiley- VCH: Verlag),J.W. Goodby, G.W. Gray and H.W. Spiess, Eds., (1998)
10. L. Bata, and A. Buka, Mol. Cryst. Liq. Cryst., 63, 307 (1981)
11. L. Benguigui, Phy. Rev. A, 29, (1984)
12. L. Benguigui, J. Physique, 41, 341 (1980)
13. J. Czub, U. Gubernat, B. Gestbloma, R. Dabrowski, and S. Urban, Z. Naturforsch. 59a, 316 (2004)
14. S. Chandrasekhar, Liquid Crystals, (Cambridge University Press, Cambridge, U. K.) (1992), 2nd ed
15. G. Padmajarani, D. M. Potukuchi, and V. G. K. M. Pisipati, Frequency shifts in smectic multiple relaxations and the effect of flexible chain, Liq. Cryst. 1998;25:589–595. doi:10.1080/026782998205877
16. S. Marcelja, J. Chem. Phys., 60, 3599 (1974)

17. R. Dubey, A. Mishra, K. N. Singh, R. Dhar, P. R. Alapati, Dielectric properties of a highly polar liquid crystalline material showing various types of layered structures, Liq. Cryst., 43, 1 (2016)
18. Alapati PR, Potukuchi DM, Rao NVS, et al, Phase transition and structural investigations in 5O.5, 5O.6 & 5O.7. Liq. Cryst.1988; 3:1461–1479.doi:10.1080/02678298808086688
19. A. Bhattacharjee, P. R. Alapati, and A. L. Verma, Liq. Cryst., 29, 725 (2002)
20. K. N. Singh, B. Gogoi, R. Dubey, N. M. Singh, H. B. Sharma, and P. R. Alapati, Indian J. Phys. (communicated)
21. K.S. Cole, and R.H. Cole, Dispersion and absorption in dielectrics,Phys. 1941; 9: 341–351. doi:10.1063/1.1750906
22. W. Maier and G. Maier, Z. Naturforsch, 16A, 262 (1961)
23. R. Dhar, M. Gupta, V. K. Agarwal, and M. K. Singh, Phase Transitions, 81, 341 (2008)
24. W. H. de Jeu, W. J. A. Goossens, and P. Bordewijk, J. Chem. Phys., 61, 1985 (1974); W. H. de Jeu, and T. W. Lathouwers, Phys. Rev. Lett., 32, 40 (1974)
25. L. Benguigui, J. Physique, 40, 705 (1979); Phy. Rev. A, 28, 1852 (1983)
26. S. L. Srivastava, and R. Dhar, Indian J. Pure & Appl. Phys., 37, 891 (1999)
27. W. H. de Jeu, Physical properties of Liquid Crystalline Materials, edited by G. W. Gray (Gordon and Breach, 1980), Chap. 5, p. 49
28. G. Williams, The Molecular Dynamics of Liquid Crystals, (Kluwer Academic Press, 1994) edited by G. R. Luckhurst and C. A. Veracini, p.431
29. H. Kresse,Advances in Liquid Crystals, (Academic Press, New York) edited by G. H. Brown, Vol. 6, p. 109 (1983)
30. D. M. F. Edwards, and P. A. Madden, Mol. Phys. 48, 471 (1983)
31. N. V. Madhusudana, B. S. Srikanta, and M. S. R. Urs, Mol. Cryst. Liq. Cryst., 108, 19 (1984)
32. B. S. Srikanta, and N. V. Madhusudana, Mol. Cryst. Liq. Cryst., 108, 39 (1984)
33. J. M. Czerwiec, R. Dabrowski, M. Zurowska, D. Ziobro, and S. Wrobel, Acta Phys. Pol. A, 117, 553 (2010)
34. C. C. Wang, M. He, F. Yang, J. Wen, G. Z. Liu, and H. B. Lu, Appl. Phys. Lett., 90, 192904 (2007)

35. Guo- Zhen Liu, C. Wang, C. C. Wang, J. Qiu, M. He, J. Xing, K. J. Jin, H. B. Lu, and G. Z. Yang, Appl. Phys. Lett., 92, 122903 (2008)
36. W. Helfrich, and G. Heppke, Liquid Crytals of One- and two-dimensional order, (Springer Science and Business Media) (2012)

Table 1: Phase sequence showing the transition temperatures of 5O.5 and 5O.6 measured by DSCwith scan rate 2.5°C/min in cooling cycle.

Compound	Phase sequence
5O.5	Iso 74.8℃→ N 51.0℃→ SmA 48.0℃→ SmC 44.1℃→ SmF 41.9℃→ SmG -→ Cr
5O.6	Iso 72.5℃→ N 59.9℃→ SmA ----→ SmC 50.2℃→ SmB 42.8℃→ SmF 38.6℃→ SmG -→ Cr

Figure 1: Molecular structure of N-(4-n-Pentyloxybenzylidene) 4′-n-alkylaniline (5O.m, m=5 and 6)

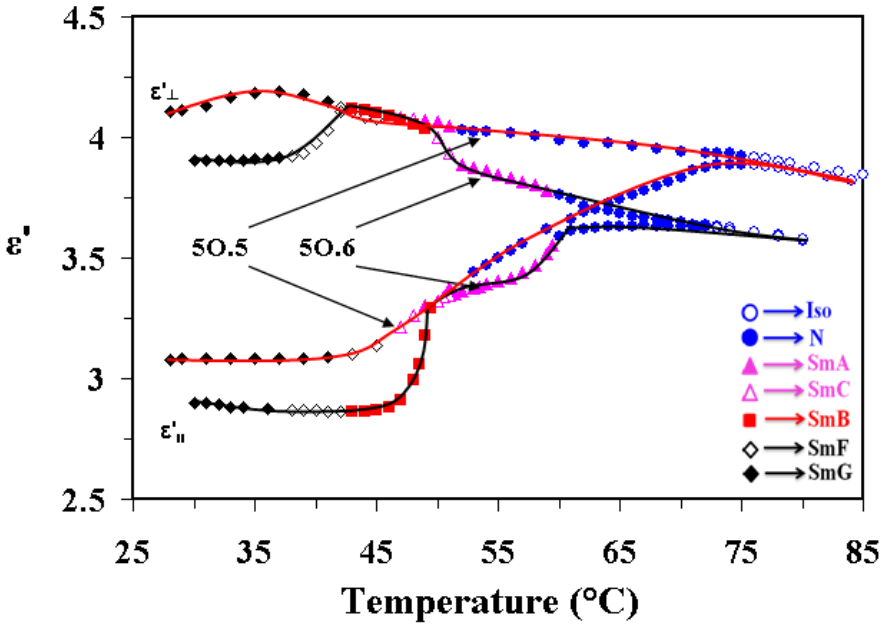

Figure 2: Permittivity (ε') as a function of temperature for 5O.5 and 5O.6 at a frequency of 100 kHz.Red line (5O.5) and black line (5O.6) on data point's isguide to the eye.

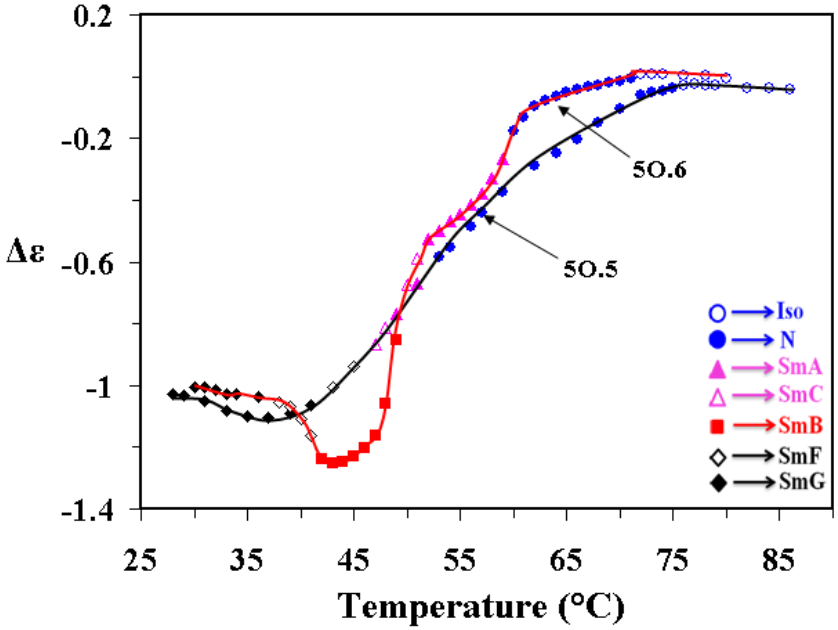

Figure 3: Dielectric anisotropy (Δε) as a function of temperature for 5O.5 and 5O.6 at a frequency of 100 kHz.Red line (5O.5) and black line (5O.6) on data points is guide to the eye

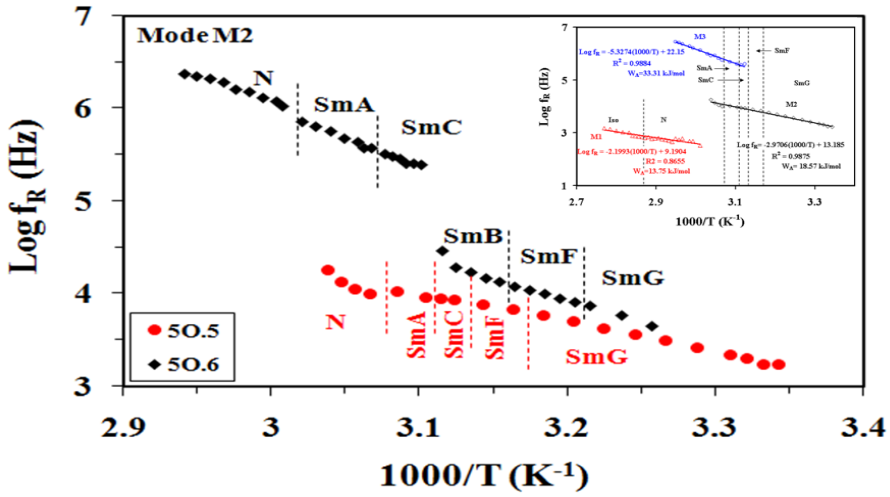

Figure 4: Variation of relaxation frequencies (f_R) with inverse of temperature of mode M2 in 5O.5 (filled circle) and only mode (M2) in 5O.6 (filled rhombus). The inset shows the variation off$_R$with inverse of temperature of different modes (M1, M2 and M3) in 5O.5.

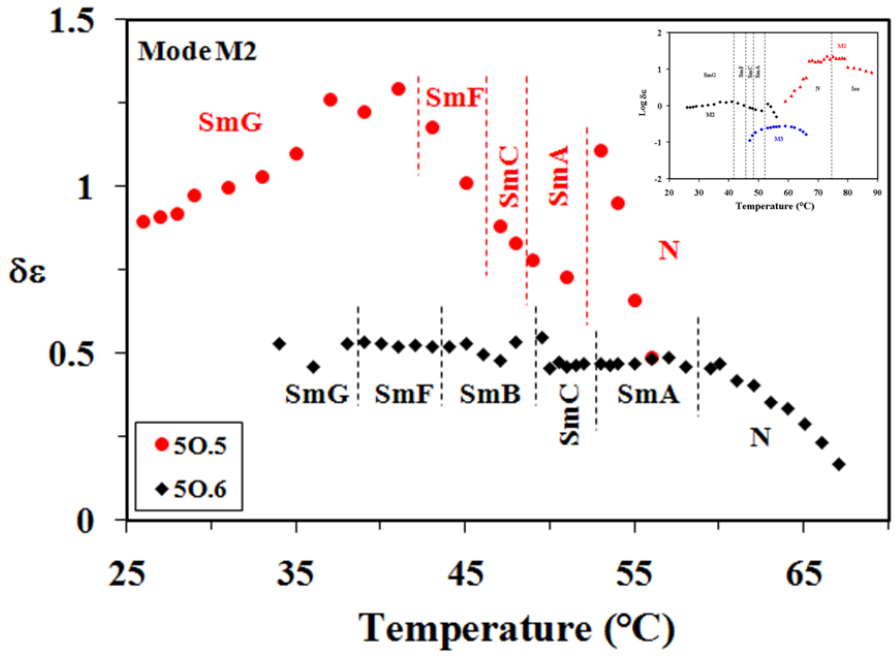

Figure 5: Variation of dielectric strength (δε) with temperature of mode M2 in 5O.5 (filled circle) and only mode (M2) in 5O.6 (filled rhombus). The inset shows the variation of δεwith temperature of different modes (M1, M2 and M3) in 5O.5.

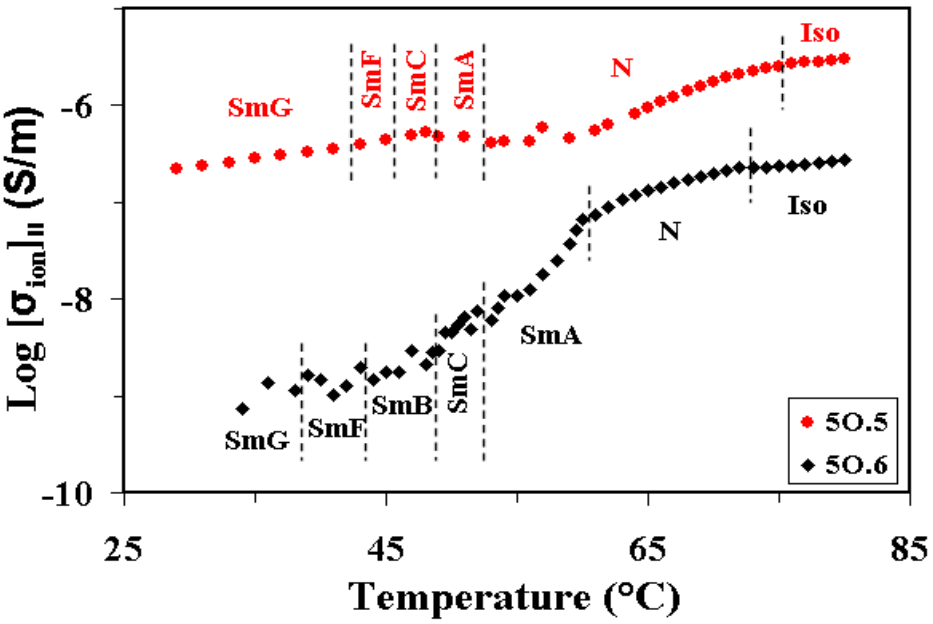

Figure 6: Ionic conductivity of 5O.5 (filled circle) and 5O.6 (filled rhombus) as a function of temperature.

Chapter: 9

Kinetic studies of 3-Toluic Acid by Ozonation, Photo-Ozonation, Peroxone and Photoperoxone

Susmita A. Mandavgane

Department of Chemistry, D. R. B. Sindhu Mahavidyalaya, Nagpur-440017 (India)

E-mail: susmitamandavgane@gmail.com

Abstract: In the present work 3-toluic acid in its aqueous solution was treated by ozonation, photo-ozonation, photoperoxone and photoperoxone processes. The experiments were carried out in a batch photoreactor using 8W low pressure mercury vapour lamp to examine the effects of different combinations of ozone, H_2O_2 and UV and their degradation rates are compared. Substrate concentration was determined by using a UV-Visible spectrophotometer. The photo degradation processes were adhered to first order kinetics. The degradation rate of 3-toluic acid obeys the following sequence: photoperoxone ($UV/O_3/ H_2O_2$) >photoozonation(UV/O_3) > peroxone(O_3/H_2O_2> ozonation (O_3).

Keywords: 3-toluic acid, ozonation, photo-ozonation, photoperoxone, photoperoxone.

1. Introduction: Recent years have demonstrated the presence of pharmaceutical compounds in rivers, lakes and even ground water; which are widely used as water resources for drinking water. Therefore, the widespread occurrence of pharmaceuticals may have a negative impact on purity of drinking water. Complete removal or reduction of hazardous organic pollutants present in wastewater to an acceptable level prescribed by the environmental protection agencies is of prime importance in wastewater treatment. Advanced oxidation processes(AOPs) are the most promising technologies for destroying toxic organic contaminants[1-3].Consequently, AOPs are of high interest to the scientific and industrial communities involved in water treatment and have been successfully applied to the detoxification of water polluted with a wide variety of chemicals such as pesticides , phenols, hydrocarbons, surfactants, dyes and pharmaceutical wastes [4-10].

Toluic acid is produced from oil industry, petroleum refining, etc. It is used as a solvent carrier in paints, inks, thinners, coatings, adhesives, degreasers, pharmaceutical products, printing industry,

leather finishing industry, rubber coating industry, shoemakers, etc. The process for manufacturing terephthalic acid generates liquid effluent streams that contain high levels of p-toluic acid, which is categorized as an environmentally hazardous material because of its toxicity and slow degradation.

Ozonation is used for the removal of odorous compounds, hazardous chemicals like pesticides and chlorinated organic compounds [11, 12]. The objective of this study is to degrade 3-toluic acid by various AOP's (UV/ H_2O_2/ O_3, UV/O_3, H_2O_2/ O_3 and O_3) and compare their degradation rates and to show that it follows pseudo-first order kinetics.

2. Materials and methods

2.1 Chemicals

Analytical grade -toluic acid was purchased from Merck, India; and was used as received without any further purification and stock solution of 0.01M of 3-toluic acid was prepared. Initial concentration of 3-toluic acid used during the experimental runs was 0.08 mM. Stock solution of H_2O_2 was prepared by diluting 30% w/v of peroxide (Qualigens) with distilled water. All stock solutions were stored in amber colored light resistant pyrex glass bottles. Oxygen cylinders were used for ozone generation.

2.2. Experimental procedure

Batch experiments were conducted at room conditions to determine the effect ozone concentration with different combinations during degradation of 3-toluic acid. All experiments were conducted out in a photoreactor (Fig. 1) equipped with low pressure mercury lamp (8W, UV-C manufactured by Phillips, Holland) placed in its centre. During the reaction, the solution was stirred by magnetic pellet to ensure its homogeneity. Ozone was produced using an ozone generator, which is high frequency cold plasma / cold corona ozone generator. The generator was fed with an inlet of pure and dried oxygen gas from an oxygen cylinder with an oxygen flow meter.

Synthetic wastewater containing 0.08 mM solution of 3-toluic acid in double distilled water was used in this study. 750 ml. of this synthetic wastewater was taken in the photoreactor and irradiated with UV lamp of 8W. Various experiments were carried out using UV light with

oxidant at various stoichiometric ratios of oxidant/pollutant. The overall degradation reaction was carried out for 45 min when O_3 was usedas oxidant.

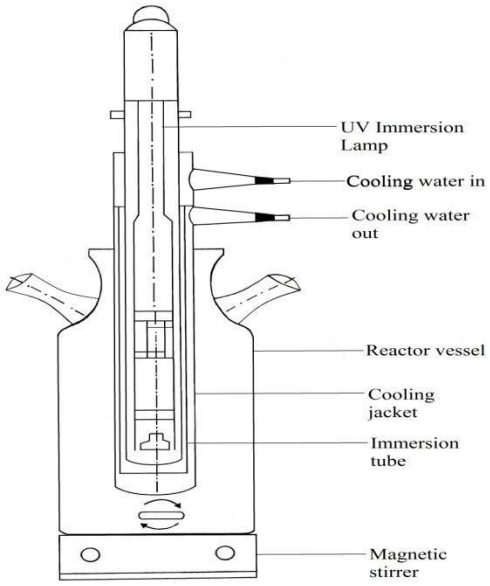

Figure 1: Photoreactor

2.3. Analyses

The initial pH of the solution was measured using Elico pH meter LI-120 equipped with a combined calomel-glass electrode. The H_2O_2 concentration in the stock solution and in samples was determined by standard iodometric titration method described in Jeffery et al. (1989).

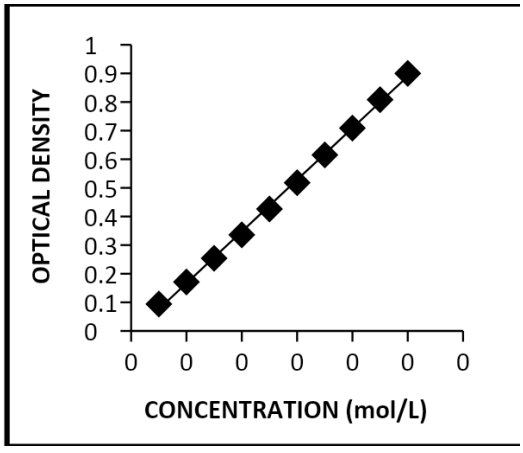

Figure 2: Beer's law plot of 3-toluic acid

The UV-visible spectrophotometric method was used for measurement of 3-toluic acid, ozone and H_2O_2 concentration in aqueous solution. A UV-visible spectrophotometer (Spectrascan UV 2600, Chemito, India) was used for this purpose. A calibration plot between absorbance and concentration of 3-toluic was plotted experimentally, which gave a high linear regression coefficient of 0.998 at 230nm (Fig. 2).

3. Results & Discussion

3.1. Effect of ozone at different combinations with UV and H_2O_2 on degradation of 3-toluic acid

To elucidate the role of ozone on degradation of 3-toluic acid, a series of experiments were performed at room conditions and optimum pH by varying the conditions as follows:

1. Only O_3
2. H_2O_2 /O_3
3. UV/O_3
4. UV/O_3/H_2O_2

The degradation of 3-toluic acid for these various conditions is illustrated in Fig. 7.

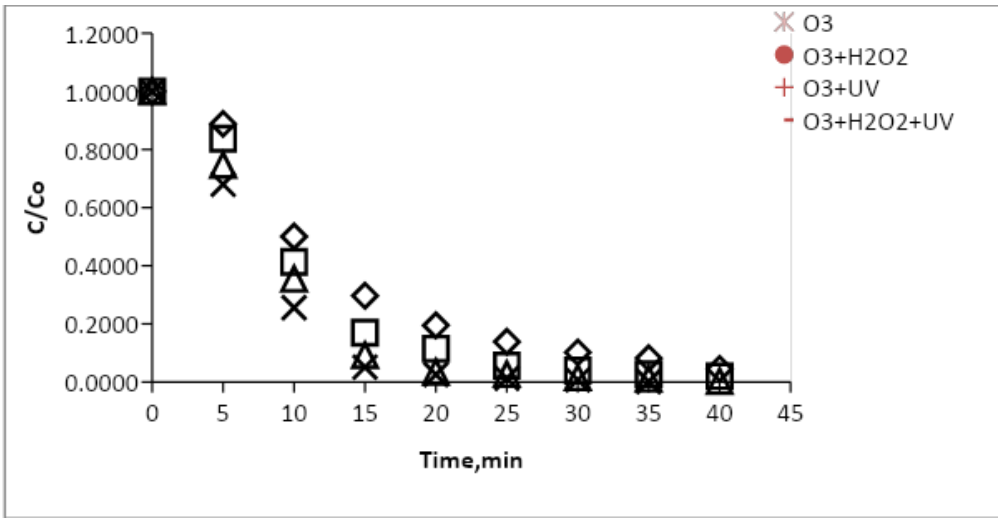

Figure 3: Degradation of 3-toluic acid by ozonation in different combinations

In photoperoxone($UV/O_3/H_2O_2$) the rate of formation of hydroxyl radicals are significantly enhanced due to UV irradiation and hence there is significant increase in the in the rates of ozonation in the presence of hydrogen peroxide and UV (11-14). Thus, it can be said that the overall efficiency of the degradation process will be significantly enhanced when a combination of UV radiation, ozone and hydrogen peroxide was used. The addition of H_2O_2 increases the contribution of ·OH radicals and helps in reducing the cost of oxidant addition, as it reduces the amount of ozone necessary to completely mineralize a pollutant or to produce a readily biodegradable wastewater solution of initially poorly biodegradable mixtures.

3.2. Comparison of various AOPs studied and the kinetic studies

A comparative study was carried out for degradation of 3-toluic acid at optimum conditions for different AOPs studied like O_3; O_3/UV; O_3/H_2O_2; $O_3/UV/H_2O_2$ and was found that the rate of degradation is highest when a combination of UV radiation, ozone and hydrogen peroxide was used.

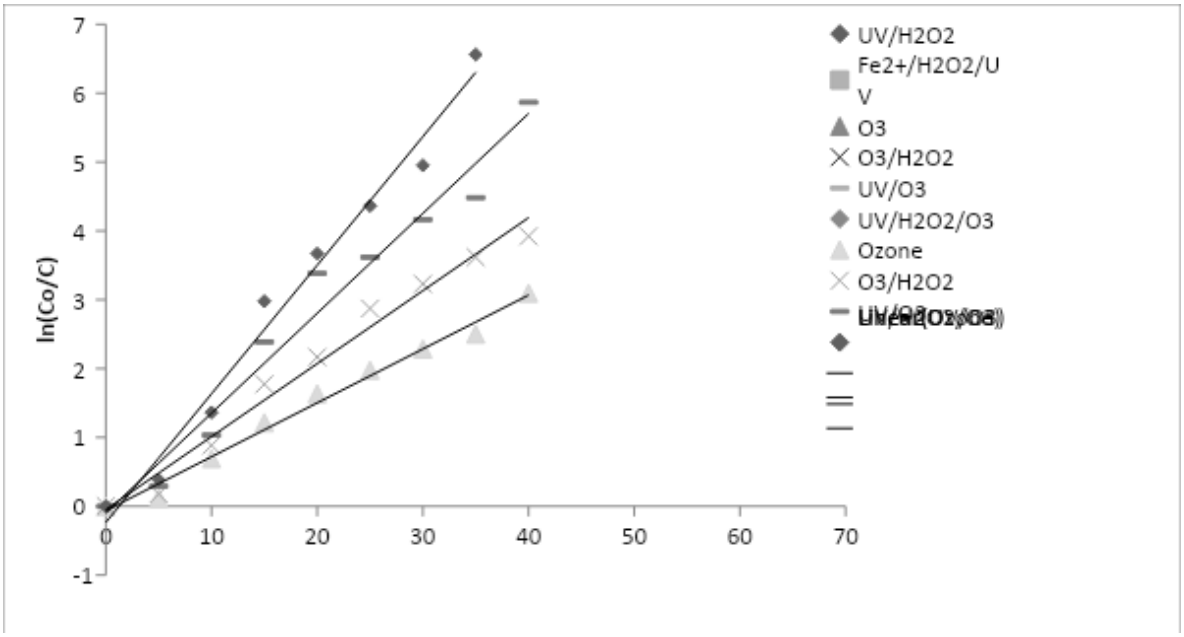

Figure 4: Concentration decline of 3-toluic acid as a function of time by different AOP's studied.

The semilogarithmic graph of the concentration of 3-toluic acid with time yield a straight line indicating the reaction is of pseudo first order (eq. A)

$-d [C(x)] /dt = k . C(x)$ …….. (A)

Where C(x) is the concentration and k (min^{-1}) is reaction rate constant.

4. Conclusions

Treatment of simulated wastewater containing 3-toluic acid by ozonation, photo-ozonation, peroxone and photoperoxone processes has been taken into consideration in the present study. All the AOPs studied were found to follow pseudo-first-order kinetics, since ozone and peroxide are in excess concentration to the substrate 3-toluic acid. The maximum degradation 99.6% of the studied substance was occurred in 35 min using $UV/O_3/H_2O_2$ combination. As can be seen from Fig 4., the rate of degradation of 3-toluic acid obeys the following sequence: photoperoxone($UV/O_3/ H_2O_2$) > photoozonation(UV/O_3) > peroxone(O_3/H_2O_2> ozonation (O_3). As during these processes the end products are CO_2 and H_2O, they are environmentally benign processes.

5. References

1. Carbala, M., Omill, F., Lema, J., Removal of cosmetics ingredients and pharmaceuticals in sewage primary treatment. *Water Res*., **2005**, 30: 4790-4796.

2. Susmita A. Mandavgane; Study of degradation of p-toluic acid by photo-oxidation, peroxidation, photo-peroxidation and photo-fenton processes; *Materials Today: Proceedings*, **2020**, 29: 1213–1216.

3. Huber, M., Oxidation of pharmaceuticals during ozonation and advanced oxidation processes. *Environ. Sci. Technol*, **2003**, 37: 1016-1024.

4. Mandavgane Susmita A., Yenkie M. K. N., *Rasayan Journal of Chemistry- International*, **2011**, Vol 4, No 3: 640-647.

5. Zweiner, C., 2000. Oxidative treatment of pharmaceuticals in water. Water Res., 2000, 34: 1881-1885.

6. Tunes, T., 2003. Ozonation: a tool for removal of pharmaceuticals, contrast media and fragrances from wastewater? *Water Res*., **2003**, 37: 1976-1982.

7. Kim WH, Nisijima W, Baes AU, Okada M. Pilot plant study on ozonation and biological activated carbon process for drinking water treatment, *Water science Technology*, **1997**; 35:21- 8.

8. Fernando J. Beltran, Vicente Gomez-Serrano, Antonio Duran, Degradation kinetics of p-nitrophenol ozonation in water, *Water Research*, **1992**, Vol. 26, No. 1: 9-17.

9. G. Anipsitakis, D.D. Dionysiou, *Environ. Sci. Technol*., **2003**, 37**:** 4790-4797.

10. Gogate, P. R., Pandit, A. B., A review of imperative technologies for wastewater treatment I: oxidation technologies at ambient conditions, *Adv. Environ. Res*., **2004**, 8(3-4) 501-551.

11. Bader H. Hoigne J. Determination of ozone in water by the indigo method, *Water Res*.,**1981**, 15: 449-456.

12. Lawrence J, Tosine H, Onuska F.I., Comba M.E. The ozonation of Natural waters: production, identification, *Ozone Sci Eng*., **1980**; 2:55-64.

Chapter: 10

Impact of Carbon dioxide on Health and Environmental

Vikas Tripathi[1] and Arvind Kumar Tripathi[2]

[1]Research Scientist, FMCG Industry, Gurugram, Haryana, India

[2]Chemist, Uttar Pradesh Rajya Vidyut Utpadan Nigam Limited, UP, India

E-mail: vikaschembhu@gmail.com; arvindbhuchem@gmail.com

Abstract: Carbon dioxide (CO_2) is actually one of the products produced during human metabolism, at higher concentrationswhich demonstratehazardous impact. CO_2 can be considered asimportant long-living greenhouse gases in the atmosphere, it accomplishesto be assessed for risks. The discussion of risk assessment as well as risk management, obviously circles around Carbon capture and storage (CCS). Therefore, this chapter presents an outline of excellent risk assessment as well as consequent risk management modeling tools explored in handling carbon dioxide. The objective of present chapter is the demonstration of a comprehensible viewpoint of CO_2. Additionally, this chapter covers the critical assessment of the impact of carbon dioxide toxicity on humans as well as the environment.

Keywords: Carbon dioxide; greenhouse gas;CCS (Carbon capture and storage).

Introduction

Carbon dioxide (CO_2) is a non-flammable, odorless, and colorless gas, undetectable to human senses, and often accumulated near the ground. It is inherently a product of ignition, fermentation, and breathing process. These peculiarities elucidate why surrounded environments are woundable for CO_2 buildup, dislodging oxygen from the region.[1] The volcanic outgassing, burning of organic matter, exhalation and inhalation processes of living aerobic organisms, burning of various fossil fuels for power generation, and usage for transportation are some of the major natural and man-made sources for the presence of atmospheric carbon dioxide.

The characteristic attributes of carbon dioxide prevail as comparatively more vulnerable to humans and the environment. The defined dense behavior of CO_2 i.e. 1.5 times than air, proportionally accounts for an increase in the tendency of leaking from pipework or confined storage spaces, which could create hazardous situations. Likewise, colorless, tasteless, and

odorless inherent property acts as an add-on to the hazardous nature of the release of CO_2.[2]Consequently, the enhanced atmospheric concentration of CO_2 can also have phenomenal repercussions on global warming.

Moreover, the long-term exposure, to airborne carbon dioxide, ranging between 0.5-1% concentrations can result in chronic effects such as metabolic acidosis and increased calcium deposits in soft tissues. The further increment in the concentration above 3% can prove to be lethal to the cardiovascular system and upper respiratory tract. The leakage can adversely affect the environment as well as human health resulting in an unforeseen impact on society as a whole. This indicates the requirement to conduct risk recognition programs centered on hazard identification, mitigation, and management.

Occurrence: The carbon dioxide naturally occurs in the atmosphere as a trace gas. Due to its solubility in water, it occurs naturally in groundwater, rivers and lakes, ice caps, glaciers, and seawater. It is present in deposits of petroleum and natural gas.

This appears to be antecedent of the times of Pliny, who in his "Naturalis Historiae" had stated, "But, by Hercules! the history of the heavens themselves would not be more difficult to relate: the abundance of metals, the virtues of medicinal springs, the exhalation of deadly vapors (spiritus lethales) either emitted from caverns or certain unhealthy districts; some of them fatal to birds alone as at Socrate, a district near the city; others to all animals, except to man, while others are so to man also". The interstices mentioned in this context are conventionally called vents or Charon's sewers, culpable for exhaling a deadly vapor. The written description also acknowledges a place in Asia and prophetic caves, where safe infiltrating by others is prohibited. Only the "priest of the great Mother of the Gods" is permitted to enter those caves, for predicting the future, as at Delphi. With the advent of modern times, the writings by Pliny are still unquestionable, due to his reference to the presence of carbonated water springs and CO_2 vents, such as the Grotta del Cane at Pouzzoles near Naples and likewise.

Historical Background

The initial chronicle of CO_2 was described in the early 1600s by J. B. van Helmont, which was specifically delineated by Joseph Black in 1756. Furthermore, with the passage of time, the toxic attributes of carbon dioxide were evidently revealed in the 19th century.

Physicochemical Properties: Under atmospheric requisite, carbon dioxide remains chemically stable and inert. It completely overcomes and restrains the combustion reactions. Carbon dioxide possesses a corrosive effect in combination with carbon steel and non-ferrous metals due to thegeneration of carbonic acid in the presence of water. It tends to react vigorously with some definite substances particularly amines or ammonia.

CO_2 is heavier than air and therefore, expects to flow downward accumulating in pits, basements, or native depressions. In presence of even mild air movement, these pools of CO_2 can persist for many hours. The physical states of carbon dioxide exceedingly confide on pressure and temperature

Physiological Role

The prosper amount of carbon dioxide, at the cellular level, confers the modification in buffering character, thereby shifting cellular pH. Thereupon, activating the Na^+/K^+ adenosine triphosphatase (ATPase) and subsequently causing hypokalemia. On the other hand, increased concentration of carbon dioxide with the lapse of time can cause acidosis and elevated K+ post-disintegration of the normal buffering system. In appendage, peptides, proteins, and amino acids are assumed to form *N*-carboxy derivatives (carbamates) in the presence of carbon dioxide, elucidating the observed neurotoxicity. The considerable perusal of literature also acquaints with some other systemic sympathetic stimulation, for instance, a rise in heart rate, cardiac output and cardiac arrhythmias, and an enhanced mean pulmonary artery pressure and pulmonary vascular resistance.

The passively absorbed carbon dioxide through the medium of lungs is primarily borne as carbonic acid and further dissociate into bicarbonate in the blood, in solution or alliance with hemoglobin, the reaction is catalyzed with the aid of carbonic anhydrase.[3]The minor quantities of CO_2 additionally find its existence in the dissolved form in plasma and carbamino compounds in blood. The gradient flow of carbon dioxide between the blood and the air in the alveoli guides the reverse formation of bicarbonate (Figure 7.1). The amount released and the rate of release is dependent on the pH, which is regulated by various buffers inclusive of bicarbonate. The metabolism of carbon dioxide is fundamentally surmised by lungs, and in some quantity by kidneys.

Uses

Carbon dioxide is extensively generated and employed in the chemical and petrochemical industries. The major part is retrieved from the former source, where it is emanated as a by-product of enumerate chemical processes such as synthesis of ammonia, methanol, hydrogen, substitute natural gas, limestone calcification, and likewise. It also finds its applicability in hydrocracking and hydrotreating petroleum products and as a coolant. Whilst in the food processing industry, it is handled in refrigeration, carbonation of beverages, and as a preservative. Additionally, it is utilized in fire extinguishers due to its oxygen displacing property. Hence, lower or anticipate burning due to the dearth of oxygen and in welding to impede molten metal reacting with oxygen.

There is also therapeutic usefulness of carbon dioxide in moderate concentrations, as it proves to be beneficial for neutralizing the effects of oxygen inadequacy. In patients after a head injury or succeeding neurosurgery, the carbon dioxide concentration may be manipulated to modify cerebral blood vessel thickness and blood flow.

Carbon dioxide has also been used in insufflation of the peritoneal cavity to permit visualization of the abdominal viscera during gynecological and surgical laparoscopic procedures. In the preceding years, it was also used in the management of hiccups, anxiety, and other psychiatricdisorders; however, the appropriateness of usage is unknown. Although, some practitioners still occasionally use this form of treatment and deaths have been reported.

Environmental Effects: One of the reasons beneath the mitigation of devastating effects on global climatic alterations lies around the CCS (Carbon capture and storage). The atmospheric level of carbon dioxide, the chief greenhouse gas, escalated around 40% since the advent of the Industrial Revolution. Out of which the oceans take up nearly one-third of that CO_2, propagating a rise in acidification by forming carbonic acid. Whereas, under other conditions, the runoff from the soil, human and animal waste, and similar origins in the ocean and rivers also play a crucial role in polluting ocean water. Additionally, initiating the depletion of oxygen level in water by the breakdown of organic matter formed during algal blooms. The potential risks may also contribute to the propagation of degraded marine ecosystems.[4] Though, carbon dioxide concentrations in ambient air does not have any lethal effect on plants, but the elevated

concentrations can disturb their growth, causing yellowing and drying out. Indirectly it may also permute pH of soil as well restrict root development.[5]

Hazardousness

The toxic behavior of carbon dioxide generally arises in presence of concentration greater than 5%, which consequently results in hypercapnia and respiratory acidosis. The interference by hydrolysis of acetylcholine by acetylcholinesterase aggravating the effects of parasympathetic nervous activity. Concentrations greater than 10% of carbon dioxide may cause convulsions, coma, and death[6-7] and more than 30% can lead to rapid loss of consciousness within a fraction of time (Figure 7.2). This clearly explains why victims of incidental intoxications often do not personate to resolve the situation (open a door, etc.).[8-10]Studies have shown a vast variableness of CO_2 tolerance in blood ranging from 0.055 to 0.085 atm (41.8-64.6 mmHg) alludes to safe exposure level,[9] which reduces, with age and in cigarette smokers. Concentrations of inevitable cases of carbon dioxide transmute between 14.1 and 26% CO_2 and an accompanying O_2 level between 4.2 and 25%.[7] In literature, the effects of oxygenmanagement both normal and high concentration have been documented.[10-11]

The enhanced concentrations of oxygen elevate venous partial pressure minimizing the dissolvability of carbon dioxide in the blood. The process, in turn, induces venous partial pressure of CO2 to rise in blood with no alteration in the metabolic requisites. A commencing augment of pCO2 in the bloodstream is expected while giving oxygen to a hypoxic carbon dioxide intoxicated person also so-called as Haldane effect. The high concentrations of oxygen may also result in the enhancement of dead space.

Carbon dioxide Toxicity: Case Study May 25, 2019: After carbon dioxide leak on a cargo ship, named Jin Hai Xiang, repaired at a dock in China. Consequently, 10 people were killed and 19 were injured reportedly. August 16, 2008: An incident took place post leakage of carbon dioxide in a gloss paint manufacturing plant In Mönchengladbach, Germany. The outbreak triggered the fire, propagating the formation of cloud that intoxicated a total of 107 individuals.

References

1. C. Zaba, J. T. Marcinkowski, A. Wojtyla, A. Tezyk, J. Tobolski and Z. Zaba, *Annals of Agricultural and Environmental Medicine*, **2011**, 18(2).
2. IPCC. (**2005**). Special Report on Carbon Dioxide Capture and Storage, Intergovernmental Panel on Climate Change, London: Cambridge University Press.
3. S. Patel, J. H. Miao, E. Yetiskul, et al. (**2020**). Physiology, Carbon Dioxide Retention. In: StatPearls. Treasure Island (FL): StatPearls Publishing
4. A. L. Strong, K. J. Kroeker, L. T. Teneva,, L. A. Mease and R. P. Kelly, *Bioscience*, **2014**, 64, 581-592.
5. A. Rusin and K. Stolecka, *Journal of Power Technologies*, **2014**, 94(4), 323-328.
6. N. J. Langford, *Toxicological Reviews*, **2005**, 24(4), 229-235.
7. C. Zaba, J. T. Marcinkowski, A. Wojtyla, A. Tezyk, J. Tobolski and Z. Zaba, *Annals of Agricultural and Environmental Medicine*, **2011**, 18(2).
8. S.Srisont, T.Chirachariyavej and A. V. Peonim, *Journal of Forensic Sciences*, **2009**. 54(4), 961-962.
9. M.Kettner, F.Ramsthaler, C.Juhnke, R.Bux and P. Schmidt, *Journal of Forensic Sciences*, **2013**, 58(2), 556-558.
10. M.Gill, M. J.Natoli, C.Vacchiano, D. B.MacLeod, K.Ikeda, M.Qin, et al. *Journal of Applied Physiology*, **2014**, 117(4), 406-412.
11. W. U.Spitz and D. J. Spitz, Asphyxia. In: Spitz WU (Ed.), Spitz and Fischer's medicolegal investigation of death,**2006**, (pp. 783-845). Springfield: Charles C Thomas.

Chapter: 11

Synthesis Characterisation and ^{1}H-NMR Studies of some Bis Polymeric Ligands

Vaishali P. Meshram

Department of Chemistry, Dharampth M. P. Deo Memorial Science College,

RTM Nagpur University, Nagpur, Maharashtra, India-440 033

E-mail: vaishali296@rediffmail.com

Abstract: Ligands of hydroxamic acid with adipic acid, azelaic acid, succinic acid, sebasic acid and subaric acid have been prepared in benzene medium by condensation process. The structural composition has been determined from elemental analysis, ^{1}H-NMR and IR spectra. The spectral assignment of NMR has been done with the help of distortion fewer enhancements by polarization transfer and the H-H coupling are explained with the help of total Correlated Spectroscopy. H-NMR Spectroscopy is a powerful technique for investigating nuclear structure of any organic compounds. Now a day's proton NMR technique can be used for determination of stereochemical structure and conformational analysis of polymer compounds. The chemical shift in NMR spectrum, indicates that what type of hydrogen atoms are present e.g., methylene, methyl groups, olefins, ethers, esters and aromatic compounds. 2D-NMR methods have been used as powerful and reliable techniques for determination of compositional and configurationally structure of co-ordination polymer. Polyvinyl pyridine and its copolymers have important applications as polyelectrolyte, polymer regents and in electrical applications. A literature survey however reveals that ligand with adipic acid, azelaic acid, succinic acid, sebasic acid and subaric acid which can be used for the preparation of chelate polymers of first transition metal ions. These ligands have been synthesized and characterized by various instrumental techniques.

Keywords: ^{1}HNMR studies, polymeric ligands, IR studies, spectral studies

Introduction

Synthesis of inorganic polymer is an emerging field that covers a wide range of disciplines including the frontiers of chemistry, materials, medicine, electronics, optics sensors, information

storage, energy conversion, environmental protection aerospace and many more[1-2]. Chelate polymers have important applications in medical sciences like controlled drug delivery, artificial organs and protein synthesis. Some polymers can be made to be electrically conductive and offer potential for the semiconductor industry and as lightweight electrodes and electrolytes for batteries for automotive and aerospace applications. Newly developed polymers exhibit unusual optical properties that have attracted significant interest from the defense industries. Besides the synthesis of chelate polymers and examination of their thermal stability, present work describes structural characterization of these chelate polymers on the basis of elemental analyses infrared and reflectance spectra, magnetic and thermal studies. Since polymeric chelates are thermally resistant and have a large number of practical applications[3-4]. Recently some chelate polymers have been synthesized, characterized and their thermal stability has been studied [5].

Experimental

Chemicals: All the chemicals used were AR grade (Merck). The solvents used were doubled distilled before used.

Instrumentations:

^{1}H-NMR ($CDCl_3$, DMSO-d_6) spectra were recorded on Bruker model DRX-30 NMR Spectrophotometer using TMS as internal reference (0 ppm) Carbon, Hydrogen and Nitrogen contents were analyzed on an EA 1108 Carlo Erba Elemental analyzer instrument at CDRI Lucknow. FTIR spectra were recorded on a Bruker IFS 66V Germany, spectrometer using the KBr technique at Regional Sophisticated Instrumentation Center, IIT Chennai. Reflectance spectra of the chelate polymers in solid state were recorded on a single beam Karl-Zeiss Jena, specord M-400 spectrophotometer, and finely powdered barium sulphate was used as a reference material in the studies of reflectance spectra. Magnetic susceptibility of chelate polymers was determined by the Gouy's method at room temperature using mercury tetrathiocyanatocobaltate (II) as standard. The non-isothermal measurement of Mn (II), Co (II), Ni (II) and Zn (II) were carried out using a TGS-2 thermogravimetric analyzer along with a TADS computer system at the Regional Sophisticated Instrumental Center, Nagpur University, Nagpur. The thermocouple used was Pt-Pt-Rh with a temperature range of 20-1000°C, 12mg sample was taken and the heating rate 15^0C/min was employed. The thermal analyses were carried out in air atmosphere and mass loss was recorded continuously on the recorder.

Preparation of dichloride of adipic, azelaic, succinic, sebasic and subaric acid: A quantity of (0.1m mol) dry acid and (0.25m mol) double distilled thionyl chloride was taken in 100ml dry round-bottomed flask fitted with water condenser provided with guard tube containing unhydrous calcium chloride. Flask was heated on a water bath for about 2-3 hours, till clear solution was obtained. The reaction mixture was then refluxed under reduced pressure for 30 min. to remove sulphur dioxide, hydrogen chloride and unreacted thionyl chloride.

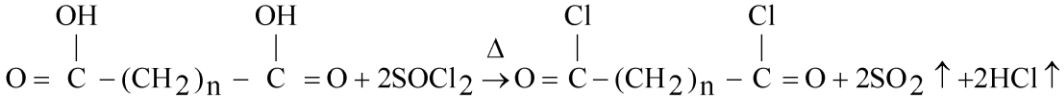

(1) *n=4* for adipic acid (2) *n=7* for azelaic acid (3) *n=2* for succinic acid (4) *n=8* for sebasic acid (5) *n=6* for subaric acid.

Preparation of ligand:

In present investigation, a modified method Priyadarshini and Tandon[6] based on Schotten Baumann reaction, was used for the preparation of hydroxamic acid. In this procedure hydroxylamine hydrochlorideand vacuum distilled acid chloride in stoichiometric ratio were reacted at low temperature 0°C or lower in diethylether medium containing aqueous suspension of sodium bicarbonate. Hydroxamic acid was prepared by the reaction of acid dichloride with excess of hydroxylamine hydrochloride in aqueous ethanol medium containing suspension of sodium bicarbonate, (0.25M) hydroxylamine hydrochloride A.R. grade, ethanol (50 mL) and sodium bicarbonate (0.5 M) and distilled water (25 mL) were placed in 500 mL beaker and acid dichloride was added (0.1 M) dissolved in 100 mL diethyl ether by dropping funnel during a period of 45 minutes with constant stirring. Mechanical stirrer was used for this. The stirring was further continued for 15 minutes. A granular solid mass was separated which was filtered and triturated with saturated solution of sodium bicarbonate in a porcelain mortar to remove any acidic impurities present and was then filtered and re-crystallized out in ethanol: DMF mixture. This ligand is reported first time in the present work and hence characterized by elemental and infrared spectral analyses. The reaction of ligand formation has shown in Fig.1

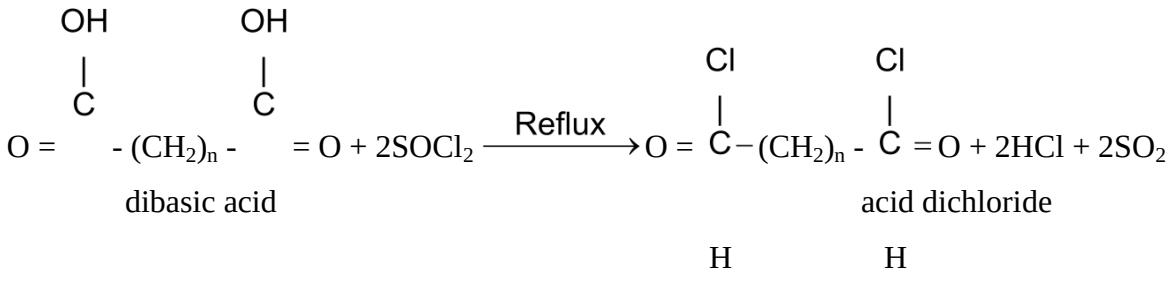

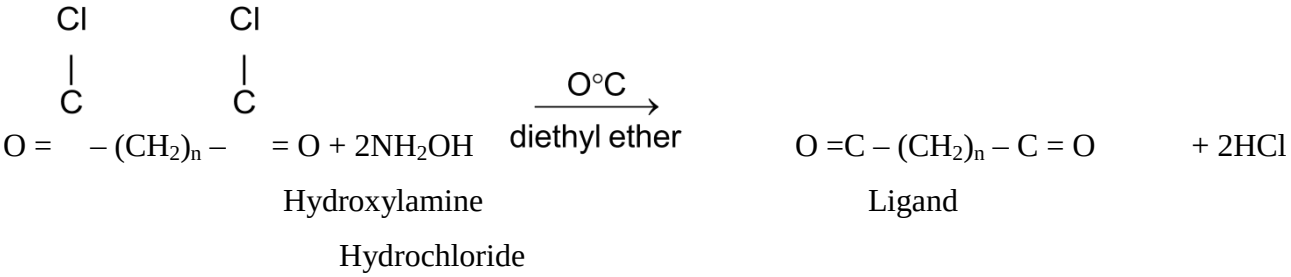

Figure 1: Synthesis of hydroxamic acid (ABHA)

Synthesis of chelate polymers of ligand

Chelate Polymers of with Mn (II), Co (II), Ni (II) and Zn (II) have been prepared by dissolving metal acetate (0.01M) separately in minimum amount of DMF and was added to a solution of hydroxamic acid (0.01 M) in (25 mL) DMF. The reaction mixtures were heated on an oil bath with constant stirring at 120 °C temperature. The chelate polymers generally appeared after 24-h heating on an oil bath. These chelate polymers obtained were filtered, washed thoroughly first with hot DMF and then with absolute alcohol and dried.

Table 1: ^{1}HNMR Spectral Data of Ligands

Observed Chemical Shift (δ) ppm					Nature of proton assigned	Expt. Chemical Shift (δ) ppm
ADBHA	**AZBHA**	**SABHA**	**SBBHA**	**SUBHA**		
2.02 – 2.37	**2.03 – 2.31**	**2.08 – 3.30**	**2.03 – 2.32**	**2.03 – 2.40**	**Methylene proton of –CO-$(CH_2)_n$-CO**	**1.4 – 2.4**
4.52	**5.57**	**5.61**	**5.57**	**5.66**	**Proton of Nitrogen of –C-NH-CO-**	**5.15**
7.33 – 7.46	**7.35 – 7.44**	**7.33 – 7.47**	**7.41 – 7.45**	**7.35 - 7.44**	**Aromatic Proton of Ar-H**	**7.42**

Table 2: Elemental Analyses of Ligands

S. No.	Name	Mol. Wt.	% C		% H		% N		% Br		Yield(%)
			Found	Calc.	Found	Calc.	Found	Calc.	Found	Calc.	
1	ADBHA	538	41.64	44.60	3.94	3.71	10.20	10.40	27.35	29.36	84
2	AZBHA	580	47.62	47.63	4.45	4.51	9.61	9.66	27.15	27.21	80
3	SABHA	510	42.34	42.40	3.10	3.13	10.85	10.98	30.85	30.79	85
4	SBBHA	594	48.42	48.48	4.71	4.74	9.35	9.42	26.48	26.54	75
5	SUBHA	568	46.34	46.51	4.16	4.25	10.05	10.21	27.74	27.81	80

Table 3: IR Spectral Assignment of Ligands (cm^{-1})

S. No.	Name	Colour	Solubility	- NH -	- CH_2 -	= C = O
1	ADBHA	White	Acetone, Hot DMF, Acetic acid & ethanol	3427 (s)	2882 (w)	1655 (vs)
2	AZBHA	White	Acetone, Hot DMF, Acetic acid & ethanol	3480 (vw)	2936 (w)	1700 (vs)
3	SABHA	White	Acetone, Hot DMF, Acetic acid & ethanol	3427 (w)	2937 (vw)	1606 (vs)
4	SBBHA	White	Acetone, Hot DMF, Acetic acid & ethanol	3427 (w)	2935 (w)	1606 (w)
5	SUBHA	White	Acetone, Hot DMF, Acetic acid & ethanol	3432 (vs)	2940 (w)	1656 (w)

Resultsand Discussion:

The ^{1}H-NMR Spectrum of hydroxamic acid ligands with adipic acid, azelaic acid, succinic acid, sebasic acid and subaric acid in acetone solvent along with complete assignments of resonances signals for aliphatic and aromatic protons are shown in Fig.1 to 5. The NMR signal around δ (chemical shift) 2.05-2.40 ppm is assigned to the over laps of –CH_2-protons of Ligands [7]. The aromatic protons of two phenyl groups are appeared at δ 7.48-7.63 ppm due to the presence of(-NHC=O) amide groups attached directly to benzene ring [8] and other resonance signal around δ 7.35-7.47 ppm is assigned due to two protons of benzene ring at which bromine attached[9-10] .

The resonance weak signal around δ 4.54-5.64 ppm is assigned to –NH-region of ligands and other weak signal around δ 8.24-8.27 ppm is assigned two protons of amide group (-NHC=O) [11] . In the infrared spectrum of the ligands a weak bands appeared from 3427-3480 cm^{-1} due to the presence of stretching vibration of the NH group [12]. Another sharp bands observed from 1606-1700 cm^{-1} may be assigned due to the C=0 stretching vibration[13] . A weak band appeared from 2882-2940 cm^{-1} may be assigned due to stretching vibrations of $–CH_2–$groups. ^{1}H-NMR, elemental analyses and infra-red spectra assignment of ligands are shown in Table 1, 2 and 3.

Composition of the polymeric unit: the composition of the polymeric unit was assigned on the basis of detailed study of elemental analyses. The presence of water of crystallization was ascertained on the basis of thermal studies. The composition of polymeric unit is $[M(II)L]_n$, $\{[M'(II) (L) 2H_2O]H_2O\}_n$ whereas (M = Zn(II), (M'= Mn(II), Ni (II) and Co(II)) (L = ABHA ligand).On the basis of elemental analyses, infrared spectra, reflectance spectra, magnetic measurements and thermal studies, the proposed structure of these chelate polymers .

Infrared spectral studies: In infrared spectra, a broad band appears at 3257 cm^{-1} in ABHA ligand may be assigned to the O-H stretching vibration [14]. A band appears at 1664 cm^{-1} in ABHA may be due to the resonating structure of the N-N-(C=O)-OH moiety. A band appears at 968 cm^{-1} may be assigned to the N-O stretching vibration.

The hydroxamic acids generally form five membered chelate ring with a metal ion and coordination takes place through >N-O and >C=O oxygen. As is anticipated, a band due to the O-H group disappears in polymers. Whereas a band due to the carbonyl group is shifted towards lower frequency side indicates that there is the formation of C=O □ M coordinated bond. The N-O band in polymers found to have been shifted slightly to higher frequency side with increase in its intensity. A medium band appears in the region of lower frequency may be assigned to the M-O bonding in chelate polymers. Thus, from the above discussion and from the consideration of potential donor atoms of the polyligands, it can be concluded that the substituted-bis-hydroxamic acids act as bidentate ligands and participated in bonding through the phenolic oxygen and the oxygen of the C=O group to give neutral linear chain chelate polymers.

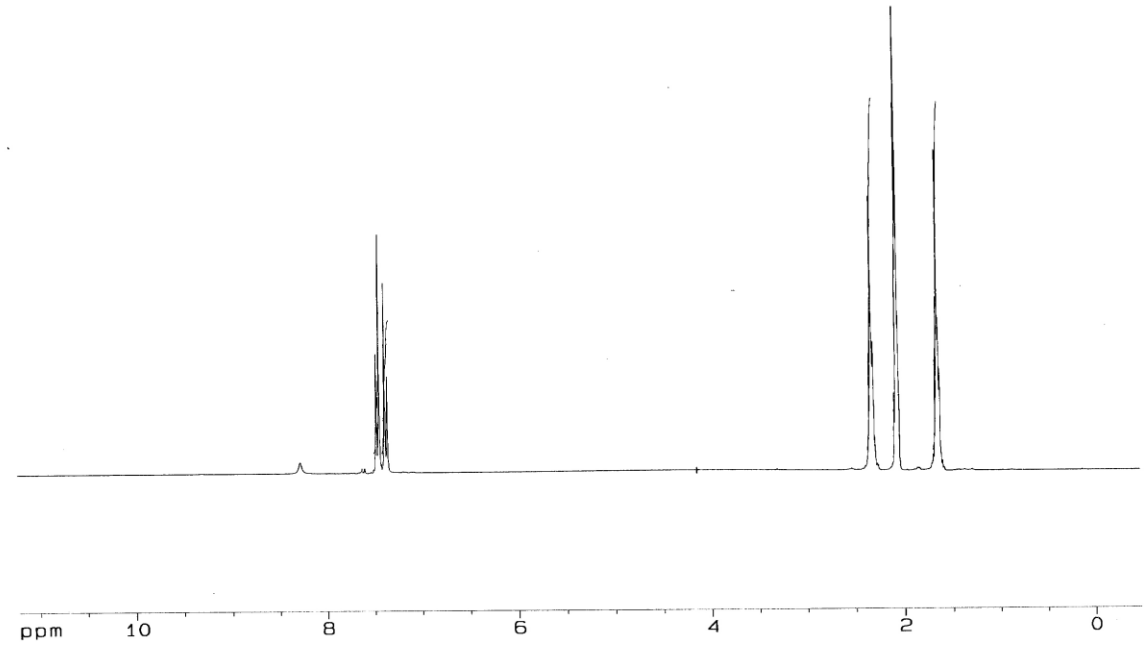

Figure.1: ^{1}H NMR of Ligand (ADBHA)

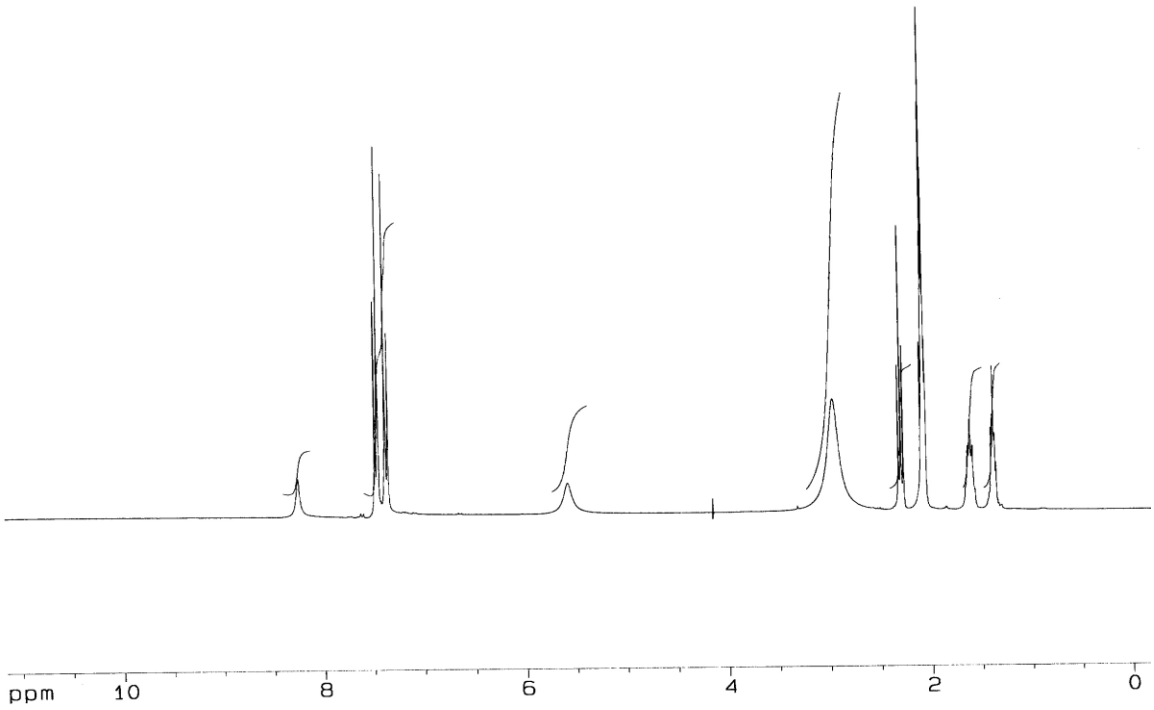

Figure 2: ^{1}H NMR of Ligand (AZBHA)

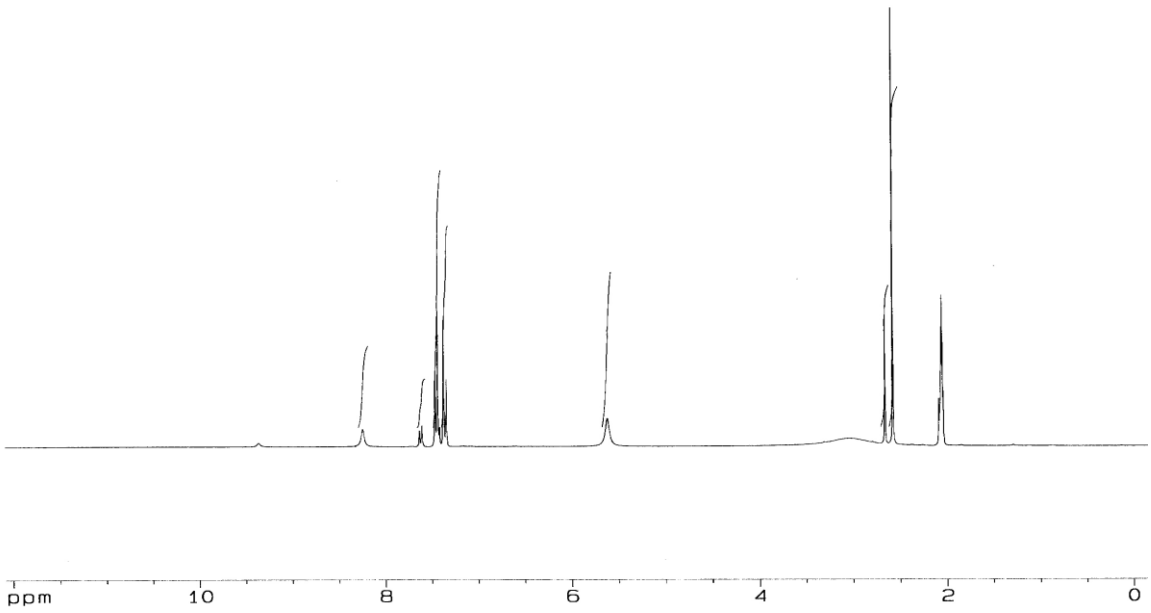

Figure 3: ^{1}H NMR of Ligand (SABHA)

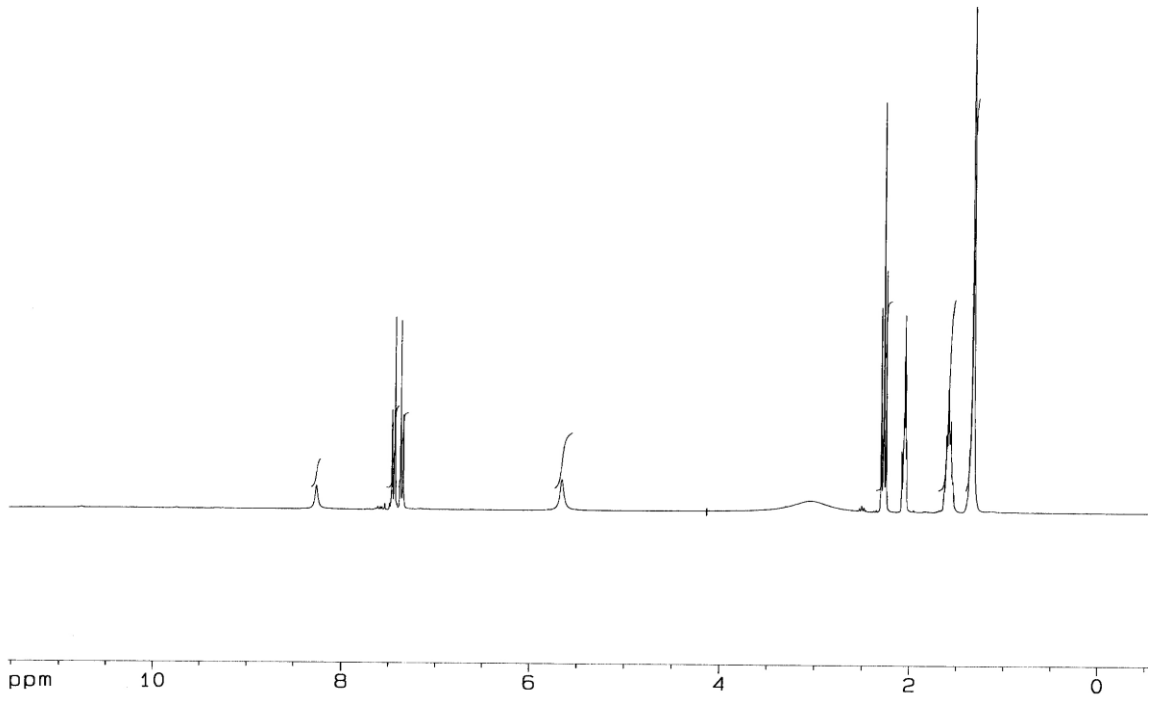

Figure.4: ^{1}H NMR of Ligand (SBBHA)

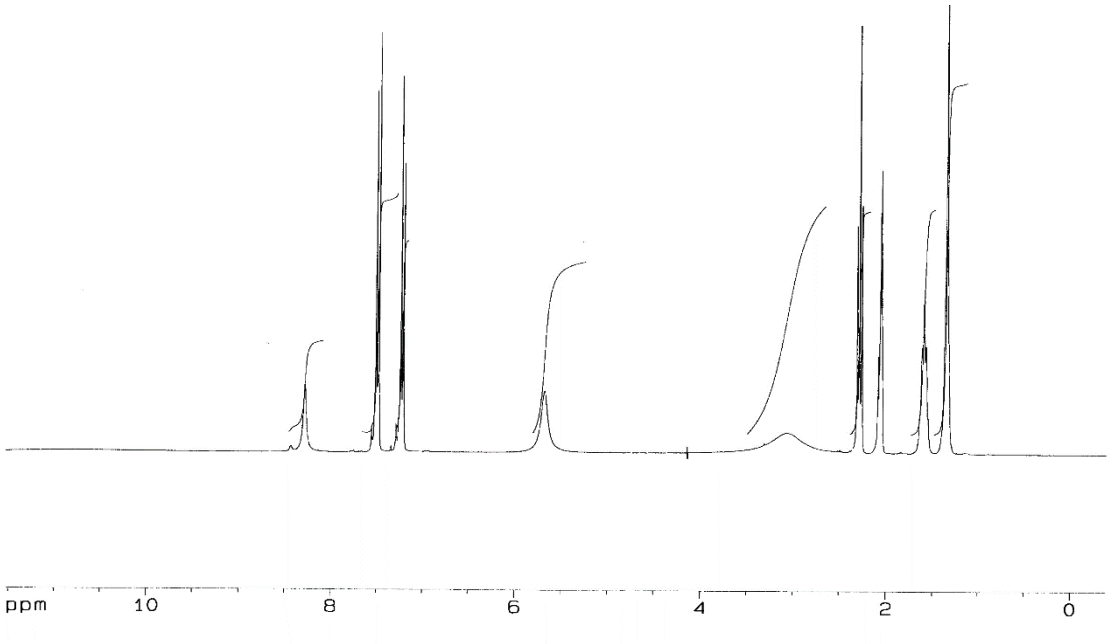

Figure 5: ^{1}H NMR of Ligand (SUBHA)

References:

1. L.M.Jackman and S.Sternhell, Application of Nuclear Magnetic Resonance Spectroscopy in organic chemistry, 2nd Ed.(Oxford;Pergaman Press,**1969**).
2. J.S.Waugh, *Analytical Chemistry*, 65, no.17 (**1993**)725A-9A.
3. A.S.Brar and R.J.Kumar, Polym.Sci.Part A; *Poly.chem*. 84(2002)50.
4. A.S.Brar, Hooda S.and Kumar R., *J.Polym.Sci.* Part A; 84(2002)50.
5. Sunita Hooda, Rajeev Kumar and Manpreet Kumar, *Indian J.of chemistry*, 43 A (**2004**)527-531.
6. Vogels, Text book of Practical Organic Chemistry, Fifth Edition, Revised by Briam S. Furniss, Antoy J. Hannaford, Peter W. Smith and Austin R. Tatchell, 965.
7. R. J. Abraham, J.Fisher and P.Loftus, Introduction to NMR Spectroscopy (New York, Wiley, 1998).
8. Michael Mcgregor, NMR Spectroscopy, Hand book of instrumental Techniques for Analytical Chemistry, 316.
9. A. E. Tonelli, NMR Spectroscopy and Polymer Microstructure, The conformational connection (New York; VCH, 1989).
10. Laurent F.Groux,Thomas Weiss,Dastigin N.Reddy,Preston A.Chase,Warren E.Piers,Tom Ziegler,Masood Parvez and Jordi Benet-Buchhotz,*J.AM.Chem.Soc*.Vol.127,No.6(2005)1865.
11. Robert M.Silverstein, Francis X.Webster, Spectrometric Identification of Organic Compounds, John Wiley and Sons Inc.New York, 1998.
12. W. B. Gurnule, P.K.Rahangdale, L.J.Paliwal and K.B.Kharat, Reactive and Functional Polymers 55(**2003**)255-265.
13. Ashaq Hussain, Sheikh H. N.and Kalsotra B.L., *J.Indian Chem. Soc*., 83,531-535, (**2006**).
14. Azza A. A. Abu-Hussen, *Journal of Coordination Chemistry*, Vol. 59, No. 2, 157-176, (**2006**).

Chapter: 12

Ecological and economic considerations of Deep Sea bed Mining Manganese : A Review

Ratna Sarkar

Department of Chemistry, DRB Sindhu Mahavidylaya, Panchpaoli, Nagpur 440017, Maharashtra, India

Email: ratnasarkar1712@gmail.com

Abstract: Manganese nodules contain economically valuable metals which may be mined in the future to supply metals to a growing world population. Commercial interest in deep sea minerals in the area beyond the limits of national jurisdiction has rapidly increased in recent years. The International Seabed Authority has already given out 26 exploration contracts and it is currently in the process of developing the Mining Code for eventual exploitation of the mineral resources. Priority issues have so far been feasibility and profitability of this emerging industry; while relatively little consideration has been given as to how, and to an even lesser extent, whether deep seabed mining should proceed. This article provides an insight on the economic and ecological aspects of deep sea bed mining which have been studied and impacted it in the last decade

Keywords: Deep seabed mining, Minerals, Manganese, Copper, Nickel Ecological,Resources

Introduction

Increasing international interest towards deep seabed mineral resources is evident by the growth of exploration contracts in areas beyond national jurisdiction as stated and regulated by International Seabed Authority (ISA) [1]. Since 2001, countries across globe, including Germany, Russia, United Kingdom, Japan, India, South Korea and China, have entered into exploration contracts with the ISA which holds responsibility for administering the ocean floor and the subsoil thereof beyond the limits of national jurisdiction according to the United Nations Law of the Sea Convention (LOSC) [2,3].This has been primarily due to extensive demand for metal raw materials, fuelled by global growth in emerging and developing countries and demand

for rapid technological innovation. Over the next two decades, one can anticipate further escalation in the global demand of seabed minerals especially nickel, copper, manganese and cobalt metals which are subjected to high importance especially to the economy of the European Union. The German Mineral Resources Agency, Informationen der DeutschenRohstoffagentur (DERA) expects a twenty four-fold increase in the worldwide demand for seabed metals by 2035, as a result of advancements in electric mobility, expansion of renewable energies and the development of infrastructure in developing nations [4].But interestingly when viewed from a historical perspective which can be traced to early 1970's, [5] the path towards commercial deep seabed mining is less straightforward than it may seem to both proponents and critics of deep seabed mining today. Changing technological, ecological and economic frameworks contributed to the rise, fall, and eventual re-birth of deep seabed mining with no documented commercial scale mining projects being carried out till date [6].

As per German Mineral Resources Agency,DERA and US Geological Survey [7] deep seabed mining of mineral nodules has witnessed a rising interest especially towards manganese, owing to its low risk to importing nations in regard to commercial and ecological concern. Today scientifically delineated as polymetallic nodules, the HMS Challenger expedition (1872–76) [8, 9] were the first to haul manganese nodules as mineral concretions from the surface of sediment-covered abyssal plains at water depths of approximately 3,000-6,000 m. The most extensive deposits of manganese nodules have been found in the Pacific Ocean, especially in the Clarion-Clipperton-Zone between the Clarion and Clipperton Fracture Zones.Kalahari manganese district in South Africa incorporates 70% of the world's manganese seabed resource and about 25% of its reserves. Recovery of manganese from these marine mineral deposits provides huge potential to contribute towards increase in future primary supply, diversification and enabling stability of prices. Other extensive nodule fields occur in the Peru Basin, near the Cook Islands, and in the Central Indian Ocean Basin. An estimated 8.9 billion tons of nodules are evaluated within the whole CI-EEZ area, with a total value of 10 trillion US dollars [10]. Manganese and iron oxides are the principal components in the manganese nodules, but commercial interests from the 1960s to the present day focus more on the nodule's content of nickel, copper, and cobalt [11]. Though manganese was and still is of secondary economic importance. There are also traces of other metals such as rare-earth elements and lithium, which are in demand today in many high-tech and green-tech applications [12,13].The idea of using manganese nodules as ores and therefore

considering them as a resource only came up after the Second World War, especially following the International Geophysical Year 1957-58.In West Germany, the earliest activities by companies can be traced back to 1969-72,wherein four West German companies from the mining and Metallurgy sector formed the consortium ArbeitsgemeinschaftmeerestechnischgewinnbareRohstoffe (AMR)[14]. In early 1975, AMR joined forces with three international partners from USA, Canada and Japan to create a joint venture OMI (Ocean Management Incorporated) [6,15],at a time when rapid progress of space flight provided impressive support to the ideas of high modernism [16].In a commercial system the relation between the operational costs and the market price is crucial .The prospect for manganese modules to undergo transition to become a "resource" largely depends on market demand and profitability. The relationship between costs and revenues looked favorable in the 1960s and early 1970s from the prospective investor's point of view, but it deteriorated considerably by the early 1980s. The revival in the first decade of the 21st century also took place against the background of the latest commodity boom that started in 2004 and lasted until 2011.As per United Nations Conference on Trade and Development [17] it is evident that the constant prices of metals had already risen in the mid-1960s.Looking more specifically at the constant prices for nickel and copper the metals with the highest economic significance contained in manganese nodules which had an upward trend from the mid-1960s to the mid-1970s.The consideration of adopting low operational costs for deep seabed mining in 1965 by Mero [18] provided a decisive advantage over land-based mining.This was a major pivotal point wherein companies worldwide started to look at manganese nodules as a "resource". In 1980 a study by Ocean Management Inc. (OMI) [19] released facts justifying the legal situation concerning deteriorating economic condition in deep seabed mining sector. According to OMI, from 1975 to 1980, the expected investment and operating costs had increased threefold, while the gross revenues had only doubled. The study served as an important reference to bolster that deep seabed mining is economically viable subject to substantial increase in prices of manganese metals or significant technological improvements or project scenarios that result in much lower investment and operating costs[19].This was evident in the revival of deep seabed mining in the 21st century which took place during substantial high commodity prices triggered by a fast expansion of demand worldwide, especially in China and India [20,21].One indicator for the growing attractiveness of deep seabed minerals in times of rising metal prices is the number of

exploration contracts between the ISA and state agencies. Till date, there are 17 such 15-year contracts for manganese nodules: seven of which were entered into in 2000/01, directly after ISA had adopted the respective regulations, while one contract with Germany was concluded in 2006 and the remaining nine were concluded since 2011.Since 2011 prices of metals and commodities, fell back drastically and it remains to be seen how this affects plans for deep seabed mining and whether the history of the 1970-80s will repeat itself [3].

Economic impact on global level

Inflated adjusted operational costs is expected to be lower today than in the 1980s due to technological progress and advances like deep-water oil drilling that have advanced considerably in recent decades. For instance, exploration has become more precise and cost-effective by today's multi-beam echo sounders or side-scan sonars which combined with the Global Positioning System produce detailed maps of the seafloor's topography in real time [22].In 2019, a Belgian company, Global Sea Mineral Resources (GSR), has planned to test a collector vehicle for manganese nodules in GSR's and Germany's exploration areas in the Pacific [23].Japan successfully conducted a pilot mining test in the Economic Exclusion Zone (EEZ)[24] around Okinawa in August and September 2017 [25].Nautilus Minerals, a Canadian company, is expected to start commercial mining of seafloor massive sulphides from a site within the EEZ of Papua New Guinea [26].Large scale metal recycling has also been pivotal to compensate the rising demand of deep seabed mining of manganese, but is presently at a nascent stage due to higher operating cost.

Ecological considerations of deep sea bed mining

Recent evidences and reports claim looming of deep seabed mining in the regions beyond the limits of national jurisdiction, known as "The Area". The number of 15-year exploration contracts approved by the International Seabed Authority (ISA) under the 1982 United Nations Convention on the Law of the Sea (UNCLOS) has also soared to an impressive 26 as of May 2017, covering 1.2 million km2 of the Area [27-29].When the idea of deep-sea mining first gathered momentum in the 1960s, it was rooted in the high modernist belief in technical progress and subjecting nature to suit humanity's purposes. Towards the end of the 1970s, however, the technological optimism had given way to widespread skepticism while ecological thinking

gained more and more influence since the start of the decade. The new “ecological era” [30], had little effect on the deep sea mining projects of the 1970s. It was not until the 1980s that research into environmental impacts became the focus of manganese nodule research. Public attention to this issue is an even more recent phenomenon. At present, marine biologists, NGOs, and parts of the public are critical of deep seabed mining because of its expected ecological impact. Recent studies claim deep seabed mining will constitute a direct and intense anthropogenic impact on the deep seabed and beyond. Mining manganese nodules will likely to have a threefold impact on the marine environment [31]: First, when picking up the nodules, the collector vehicle will destroy bottom-dwelling communities living on or between them. Second, collecting the nodules will stir up a near-bottom sediment plume, which will blanket a large area outside the path of the collector vehicle as a result many organisms will be unable to cope with this effect. Third, after pumping up the nodules, the mining ship will have to discard sediments and materials abraded from the nodules, thus creating a second plume close to the ocean’s surface, which might affect filter feeding pelagic organisms [32-34]. In addition, deep-sea mining will result in increased noise levels and anthropogenic light both on and below the surface. Miller in his work specifically stresses that these effects will also impact the fauna including seabirds, marine mammals, and fish [35]. Although knowledge about the ocean floor is still incomplete today, one can assume as a guideline that dark, cold, and energy-poor deep-sea ecosystems are particularly vulnerable to disruptions and will take decades to hundreds of years to recover [36-38].The ISA is currently in the process of developing a set of rules, regulations, and procedures “the Mining Code” for eventual exploitation of the mineral resources. To date, ISA has issued Regulations on Prospecting and Exploration for Polymetallic Nodules in the Area (adopted on 13 July 2000) which were later updated and adopted on 25 July 2013; the Regulations on Prospecting and Exploration for Managanese in the Area (adopted on 7 May 2010).An increasing number of developing countries such as Fiji, Nauru, Tonga, Tuvalu, Kiribati, and China are preparing domestic legislation to regulate their prospective activities in the Area [29]. Hopes and concerns have been expressed about the future of deep seabed mining [34].

Though the repercussions of deep seabed miming are evident, the prospects of the latter towards national development cannot be deprecated. Manganese nodules through deep seabed mining has potential to contribute to global sustainable development by providing financial and other economic benefits that could be equitably shared among states on a non-discriminatory basis.

Managanese has played a crucial role in construction industry due to its sulfur fixing, deoxidizing, and alloying properties [35]. Developing countries with very limited capacities have a chance at directly engaging in deep seabed mining by sponsoring financially and technologically capable contractors. Merging countries like Nauru and Tonga, for example, signed contracts with the ISA, helping them alleviate poverty. Increasing supply of certain metals would allow green technologies to be deployed at a greater scale or at a cheaper price. But more importantly, seabed mining serves as a promising alternative to the shortage of raw metals, which has to be conventionally be relied on terrestrial sources, concerning direct environmental problems. Researchers today also confirm the decline in grade and tonnage of land-based manganese deposits, hence increasing the footprint of these mining operations. Deep seabed manganese nodules bring in high-grade deposits, requiring less substrate to be removed. In the case of Nautilus Minerals' Solwara Project in Papua New Guinea, footprint is in fact relatively small, covering just 0.112 km^2, with eight times better ore grade in the case of manganese and copper compared to terrestrial mines [36,39].

Conclusion

The history of deep seabed mining of manganese nodules illustrates how mineral concentrations can turn from “neutral commodity” into a “resource” and back again. Though manganese nodules show evident scope of further following the viscous cycle, the final outcome remains debatable. Factors contributing to this process can be summed up by the following governing aspects. Investment in technology remains primary aspect which can increase efficiencies in the collection and processing of seabed manganese nodules and improve recycling technologies. Secondly, the relationship between commodity prices and operational costs is of decisive importance governing the commercial rise and fall of manganese nodules. Plummeting commodity prices coupled with the international legal framework sealed the fate of the mining projects in the early 1980s.While the recent commodity boom between 2004 and 2011 provided the main impetus for renewed interest in deep seabed minerals. Finally, the rise of environmental awareness will play a pivotal role in deciding the fate and long term viability of deep seabed mining projects. Ecological concerns are only expected to grow exponentially and more widespread with clear growing concerns today at different global scientific, political, and public platforms.

If our predicted future consumer behavior is to be resilient whilst transitioning to a greener economy, it can be said that deep seabed mining projects will be pushed to a similar state as they were in 1980s. With current advancement deep seabed minerals, and especially manganese nodules, are once again at the threshold of being resources. However, potential adverse effects on the environment of deep seabed mining are likely to outweigh major potential benefit from increased metal supply. In accordance with the precautionary principle in international law, full-scale commercial extraction of deep sea minerals must be delayed until the long-term pros and cons of deep seabed mining are scientifically scrutinized and democratically deliberated. Nevertheless, such an arising industry requires a clear definition of threshold values, conservation strategies, management and monitoring programmes in order to avoid serious harm to the marine environment. This fact poses a great challenge to science and to the drafting of environmental regulations, standards and guidelines for deep seabed mining at this moment in time, and highlights the necessity for a clear, transparent, multi-stakeholder and adaptive regulatory process.

References

1. International Seabed Authority (**2012**). Decision of the Assembly of the International Seabed Authority relating to the Regulations on Prospecting and Exploration for Cobalt-rich Ferromanganese Crusts in the Area. International Seabed Authority.

2. Ralph Watzel (**2020**) Carsten Rühlemann, AnnemiekVink,Mining mineral resources from the seabed: Opportunities and challenges,MarinePolicy,Volume 114.

3. Luise Heinrich, Andrea Koschinsky, Till Markus, Pradeep Singh (**2020**) Quantifying the fuel consumption, greenhouse gas emissions and air pollution of a potential commercial manganese nodule mining operation, Marine Policy,Volume 114.

4. F. Marscheider-Weidemann, S. Langkau, T. Hummen, L. Erdmann, L. Tercero Espinoza, G. Angerer, M. Marwede, S. Benecke (**2016**),RohstoffefürZukunftstechnologien DERA Rohstoffinformationen, vol. 28, p. 353 S.

5. John Childs (**2020**) Extraction in Four Dimensions: Time, Space and the Emerging Geo-politics of Deep-Sea Mining, Geopolitics, 25:1, 189-213.

6. Broadus, J.M. (**1986**). Asian Pacific marine minerals and industry structure, Mar. Resour. Econ. 3, 63-88.

7. W.F. Cannon, B.E. Kimball, L.A. Corathers, Manganese, chap. L of, in: K.J. Schulz, J. H. DeYoung Jr., R.R.I.I. Seal, D.C. Bradley (**2017**), Critical Mineral Resources of the United States - Economic and Environmental Geology and Prospects for Future Supply, U.S. Geological Survey, L1–L28.

8. Fellerer, R. (**1980**), Manganknollen. GeologischesJahrbuch. Reihe, 35–76.

9. Hannigan, J. (**2016**), The Geopolitics of the Oceans. Polity Press,185.

10. Cronan, D.S., Hodkinson, R.A., Miller, S., **1991**. Manganese nodules in the EEZ's of island countries in the southwestern equatorial Pacific. Mar. Geol. 98, 425-435.

11. Michael G. Petterson, AkuilaTawake (**2018**),The Cook Islands (South Pacific) experience in governance of seabed manganese nodule mining, Ocean and Coastal Management, doi : https://doi.org/10.1016/j.ocecoaman.2018.09.010

12. Petersen, S., Krätschell, A., Augustin, N., Jamieson, J., Hein, J.R., Hannington, M.D.,(**2016**),News from the seabed-geological characteristics and resource potential of deep-sea mineral resources, 175-187.

13. Hein, J.R., Mizell, K., Koschinsky, A., Conrad, T.A.,(**2013**),Deep-ocean mineral deposits as a source of critical metals for high- and green-technology applications: comparison with land-based resources. Ore Geol. Rev. 51, 1-14.

14. Arbeitsgemeinschaft meerestechnischgewinnbareRohstoffe (**1975**), AMR Durchführbarkeitsstudie.ProjektManganknollen. ErsteWirtschaftlichkeitsabschätzung 1972-1974. HessischesWirtschaftsarchiv, Sign. Abt. 119 Nr. 1702.

15. Heath, G.R., (**1981**), Ferromanganese Nodules of the Deep Sea, 736-765.

16. Scott, J.C., (**1998**), seeing like a State. How Certain Schemes to Improve the Human Condition Have Failed. Yale University Press, New Haven, https://yalebooks.yale.edu/book/9780300078152/seeing-state

17. 14.UNCTAD (**1960**) , Free market commodity price indices, annual, http://unctadstat.unctad.org/wds/TableViewer/tableView.aspx?ReportId=30728

18. J.L Mero (**1965**). The Mineral Resources of the Sea, Elsevier: Amsterdam, 565-565. doi:10.1017/S0016756800000339

19. Ocean Management Inc (**1980**), Deep Ocean Mining. BundesanstaltfürGeowissenschaften und Rohstoffe - Archiv, Sign. 0110932.

20. Radetzki, M., (**2006**), The anatomy of three commodity booms. Resour. Policy 31, 56-64.

21. Radetzki, M. (**2008**) A Handbook of Primary Commodities in the Global Economy.Cambridge University Press, Cambridge

22. International Seabed Authority (**2019**) Polymetallic Nodules, Avaiable online at: https://ran-s3.s3.amazonaws.com/isa.org.jm/s

23. Porter Hoagland (**1993**) Manganese nodule price trends: Dim prospects for the commercialization of deep seabed mining,ResourcesPolicy,Volume 19, Issue 4, 287-298.

24. Tanaka, Y (**2012**), The International Law of the Sea, Cambridge University Press,Cambridge.

25. Ministry of Economy Trade and Industry (**2018**), Summary Report of Comprehensive Assessment Concerning Development of Seafloor Polymetallic Sulphides, Avaiable online at: http://www.meti.go.jp/english/press/2018/1031_002.html

26. Nautilus Minerals (**2019**), Deep sea mining finance, Avaiable online at: http://www.nautilusminerals.com/irm/content/tsxannouncements.aspx?RID=311&RedirectCount=1

27. Ole Sparenberg (**2019**)A historical perspective on deep-sea mining for manganese nodules 1965–2019,The Extractive Industries and Society, Volume 6, Issue 3, 842-854

28. ISA National Legislation Database, (**2017**) Deep Seabed Minerals Contractors, https://www.isa.org. Jm/deep-seabed-minerals-contractors, Int. J. Mar. Coast. Law 31, 691-705.

29. Rakhyun E. Kim (**2017**) Should deep seabed mining be allowed?, Marine Policy, 134-137.

30. Radkau, J., (**2014**). The Age of Ecology. Polity Press, Cambridge/Malden, Mass

31. McCormack, G., (**2016**) Cook Islands seabed minerals,A precautionary approach to mining. Cook Islands Natural Heritage Trust, Rarotonga, Cook Islands, 978-982.

32. Amos, A.F., Roels, O.A., (**1977**), Environmental aspects of manganese nodule mining. Mar. Policy 1, 156-163.

33. Thiel, H., Schriever, G., (**1990**), Deep-sea mining, environmental impact and the DISCOL project.,Ambio 19, 245-250.

34. Thiel, H., Schriever, G., Foell, E.J., (**2005**),Polymetallic nodule mining, waste disposal and species extinction at the abyssal seafloor. Mar. GeoresourcesGeotechnol. 23209-220.

35. Miller, K.A., Thompson, K.F., Johnston, P., Santillo, D. (**2018**),An overview of seabed mining including the current state of development, environmental impacts, and knowledge gaps. Front. Mar. Sci. 4, 418.

36. Ecorys (**2012**),Marine Sub-Function Profile Report Marine Mineral Resources(3.6). Availableonlineat:https://webgate.ec.europa.eu/maritimeforum/sites/maritimeforum/files/Subfunction%203.6%20Marine%20mineral%20resource_Final%20v120813.pdf

37. Boetius, A., Haeckel, M., (**2018**) Mind the seafloor. Science 359, 34-36.

38. C. Gramling (**2014**) Seafloor mining plan advances, worrying critics, 344-463.

39. Mengerink (**2014**), A call for deep-ocean stewardship, Science 344 (2014) 696-698.

Chapter: 13

Review on Magnetic Nanomaterials Based Metal-Oxide Humidity Sensor

[1]Y. S. Bopche and [2]R. M. Patle

[1]Department of Physics, D. B. Science College, Gondia, Maharashtra, 441614

[2]Department of Chemistry, D. B. Science College, Gondia, Maharashtra, 441614

Email: yadavbopche@gmail.com

Abstract: Humidity measurement is one of the major factors in many areas of applications like instrumentation, automated system, agriculture and climatology. This review paper reports studies on different humidity sensor fabrication technologies, principles of materials, applications in general and moisture sensing mechanisms of metal-oxide magnetic nanoparticles. The diverse merits of nanomaterials (e.g., cost-effective, rapid and precise detection capabilities with improved detection limits), nanomaterial technology has made itself a promising option for designing new and advanced sensors in different fields of science. Out of which magnetic nanoparticles (MNPs) are very attractive especially for biomedical fields due to the elemental composition that makes them biocompatible and degradable. MNPs with cubic spinel structure also possess unique multifunctional properties, such as excellent magnetic characteristics, high specific surface area, surface active sites, high chemical stability, tunable shape and size. Thus, the magnetic NPs are a suitable applicant in the world of sensors. It will be used as Bio-Sensors, Gas-Sensors, Stress-Sensors and Humidity-Sensors. Humidity sensors based on metal-oxide MNPs have advantages such as being economical for mass production, and convenient for use in wide operating range and also exhibits the morphology-dependent, chemical-resistive humidity sensing behaviors which ensures them as a potential candidate for room temperature based next generation high performance humidity sensors. The ability of a metal-oxide to detect the presence of humidity depends on the interaction between water molecules and the surface of the metal oxide. The reactivity of the surface depends on the cation distribution and morphology/porous nature of the surface created during the synthesis process.The surface of metal – oxide (ferrite) materials are porous in nature and have surface oxygen atoms which essentially arise due sample preparation technique. When the materials adsorbs the humidity, its

resistivity decreases and conductivity increases due to the production of free electrons. Hence the metal-oxide nanomaterial's acts as a strong candidature for the future humidity sensors materials.
Keywords: Humidity sensors, metal-oxide MNPs, cobalt ferrites, relative humidity.

1. Introduction:

Humidity, which is amount of water vapor present in air or atmosphere, is highly variable and changes according to seasons, temperature and so on, and has an important role in the quality of industrial products, advanced instruments and human life. The regulation of humidity is important for human comfort, storage of various goods, industrial process control, high-tech instruments, and plenty of advanced sectors [1]. In industry, optimum humidity conditions should be provided on production lines for obtaining high quality products.In the agriculture sector, since adequate environmental humidity conditions are needed to grow fruits and vegetables, similar conditions are needed in the preservation of different types of foods and cottons.In the medical field, humidity sensors are used in respiratory equipment, sterilizers, and incubators, pharmaceutical processing, and biological products. Thus, the measurement and control of humidity have significant importance in many areas for different purposes. A relationship exists between humidity and frequency or temperature. Currently, miniaturized humidity sensors have shown many advantages, including integration, small size, low power consumption, high performance, low cost, and ease of mass fabrication, compared to the classical measurement used in early age sensors [2]. The different types of humidity sensors are classified according to the working technology and sensing principle. Humidity is evaluated by different functions such as vapor pressure, saturation vapor pressure, dew/frost point temperature, and relative humidity [3].Humidity can also be expressed in other ways like absolute humidity (g/m^3), defined as the amount of water vapor contained in a unit volume of dry air.

Development of an ideal metal-oxide based humidity sensor depends on some key criteria, such as accuracy, power consumption, precision, repeatability, long-term stability, response time, size, packaging, and cost. In recent advances, cost effective miniaturization with ultra-high precise performance has received much attention for advanced application fields. To know the effect of different doping elements or materials in the sensor materials is most vital part of humidity sensor development for the different applications [4]. Due to heavy population growth and their

daily activities, environmental pollution is a great problem for a healthy atmosphere. Hence different types of gas sensors have an important role to detect or analyze the different contaminants present in the atmosphere. Importantly, the detection of humidity is one of the most important tasks owing to its versatile application in the fields of industrial control, agriculture, material analysis and biomedical instruments. A potential versatile humidity sensor must have good reproducibility, low hysteresis, low cost, be resistant against contaminants, good sensitivity, good durability and long life time, a very short response time, and low dependency on temperature. For many sophisticated applications, there has been a keen attempt to reduce the size of the sensors using the most advanced technologies collectively called miniaturization. Miniaturized humidity sensors mainly depend on five different transduction principles: hygrometry, capacity, resistance, gravimetry and optical properties [5].

In this review, we aim to present extensive researches and developments of humidity sensing materials and characteristics for a wide variety of applications. Particularly changes in impedance or resistance, capacitance, hysteresis, recovery and response times, and stability with respect to relative humidity, frequency, and temperature are the primary interest of this present review article. A typical comparative study of the above particular characteristics changes with different materials is critically reviewed in the following sections.The essential physical or morphological properties and typical electrical characteristics of relative humidity sensors based on different key materials in metal –oxide sensors such as carbon, iron, tin, titanium and zinc are highlighted. This review also focuses the changes in the physical, chemical, electrical as well as structural characteristics of the base material due to different dopants. A short review on number of key applications of humidity and moisture measurement are highlighted in different areas such as structural health monitoring (SHM), food processing and storage, medicine, ecology, agriculture, mineral processing, fuel quality control, and aerospace.

2. Metal-Oxide based Humidity Sensing Materials:

During the last five decades, plenty of sensing materials have been developed for different types of humidity sensors in a wide range of applications. The most common commercial sensors are mostly based on metal oxides, porous silicon and polymers [6]. Addition of different dopants to a base material changes its physical, chemical, electrical as well as structural characteristics and these characteristics are also changed with different base materials. In this section, different

electrical characteristics (i.e., impedance or resistance, capacitance, response and recovery time, hysteresis, and stability with the variation of relative humidity, frequency, and temperature) of various metal-oxide sensor materials based on tin, titanium and zinc are compared. Both similarities and dissimilarities in the electrical characteristics for different sensor materials are observed, which vary strongly with the doping concentration of different materials, film thickness of the substrates and the morphological changes.This is extremely important in the miniaturization of sensors in nanotechnology for many advanced applications. Therefore, in ordered to determine the best humidity sensor based on different materials, the plots of the important electrical characteristics of various morphological structures and doping agents are recognized and typically compared.Hence, this review article is mainly focused on the key sensing materials and their typical characteristic properties for the application in humidity sensors.

Metal oxide semiconductors such as tin oxide (SnO_2), zinc oxide (ZnO), tungsten oxide (WO_3) and iron oxide (Fe_2O_3) are the most popular humidity sensing materials. The fundamental principle of all these metal oxide semiconductors is based on electrical conductivity, which changes with the composition of the surrounding gas atmosphere.

2.1 Tin-Based Oxide Materials for Humidity Sensors

Tin Based Sensor Material	Method of Synthesis	Response Time (s)	Recovery Time (s)	Ref.
KCl-doped SnO_2 nanofibers silver-paladium	Electrospinning and calcination; fabricated by screen-printing	5	6	[1]
KNO_3-doped SnO_2–$LiZnVO_4$	Wet chemical and calcinations	<80	100	[7]
SnO_2–$LiZnVO_4$ ceramic	Liquid state	60	100	[8]
$La^{3+}$and K^+ co-doped $Ti_{0.9}Sn_{0.1}O_2$ thin films on alumina substrates	Sol-gel	-	-	[9]
SnO_2 nanoparticles	Microwave irradiation	-	-	[10]

KCl-doped nanoporous $Ti_{0.9}Sn_{0.1}O_2$ thin films	Sol-gel	11	14	[11]
$ZnSnO_3$ cubic crystallites	Hydrothermal	7	6	[12]

Table 1. Different types of tin oxide-based humidity sensors and their synthesis methods.

Recently, most of the development work has been focused on SnO_2-based materials, due to their large surface areas, high surface activity, good gas sensitivity, lower working temperature and adaptability to sense different gases with the addition of suitable dopants. Different types of tin oxide-based humidity sensors and their synthesis methods are listed in Table 1.

The electrical characteristics (resistance, capacitance, sensitivity, response time, hysteresis, stability) variation with the variation of frequency, temperature and relative humidity of tin-based sensor materials are explained in the following subsections.

2.1.1. Resistance or Impedance Variation with Relative Humidity

Doping concentration has a great impact on the impedance variation of tin oxide-based composites. From the experimental analysis it is confirmed that the impedance of the composite decreases with increasing doping concentration for KCl-doped SnO_2 nanofiber sensors at doping concentrations of 5%, 10%, 15%, 20% KCl [1]. The 15% KCl in SnO_2 sensor shows the best linearity and good sensitivity [1]. For other materials such as a K+-doped SnO_2–$LiZnVO_4$ humidity sensor [7], or $LiZnVO_4$ added in SnO_2 [8], and so on have shown similar kind of effects. In all these systems, the pure humidity sensor shows poor sensitivity in the whole range of humidity values, but as doping concentration is increased, the sensor impedance decreases greatly, sensitivity is enhanced, and the linearity deteriorates at high RH.

2.1.2. Effect of Frequency on Resistance-RH Characteristics

The different tin oxide-based humidity sensors show their best impedance-RH characteristics at different operating frequencies. A significant nonlinearity is observed in the low humidity range at high operating frequency and good linearity is found in the high humidity region as well as at low operating frequency. It has been seen that impedance decreases with increasing frequency

for any RH, but the best linearity of the impedance vs. RH curve is observed at lower frequency levels, for example, the best linearity appeared at 100 Hz for KCl-doped SnO_2 nanofibers [1] and 60 Hz for $ZnSnO_3$ cubic crystallite film humidity sensors [12].

The impedance became independent of the humidity at a frequency range nearly greater than 1 kHz. This is because at high frequency, the electrical field direction changes so fast that the polarization of the water cannot catch up with it, and as a result the dielectric constant becomes small and independent of RH. Conversely, the direction of electrical field changes slowly at low frequency and subsequently a high space-charge polarization appears on the adsorbed water, and thus impedance or resistance changes significantly at low frequency. In contrast, a few materials such as KNO_3 doped SnO_2–$LiZnVO_4$ [7] and $LiZnVO_4$ doped SnO_2 [8] humidity sensors show excellent linearity at any frequency over the whole humidity range.

2.1.3. Response and Recovery Time Analysis

The response and recovery time of some tin oxide-based humidity sensors such as KNO_3-doped SnO_2–$LiZnVO_4$ [7], KCl-doped SnO_2 nanofibers [1], $LiZnVO_4$-doped SnO_2 [8], KCl-doped nanoporous $Ti_{0.9}Sn_{0.1}O_2$ thin films [11], and $ZnSnO_3$ cubic crystallite [12], are listed in Table 1. From the reported data it is clear that the KCl-doped SnO_2 nanofiber humidity sensor has the smallest response and recovery time.

2.1.4. Hysteresis Characteristics Analysis

All the tin oxide-based humidity sensors show very narrow hysteresis loops of less than 6%. So far the KCl-doped SnO_2 nanofiber humidity sensor has shown smallest hysteresis of 3% among the tin oxide-based humidity sensors [1].

2.1.5. Stability Analysis

At low RH, the stability is very high for all the tin oxide-based humidity sensors as very little change in impedance or resistance is observed at low RH conditions even up to 25 months of study. Considering all the above tin oxide-based sensors, the $LiZnVO_4$-doped SnO_2 sensor impedance variation was almost constant, hence it shows the best stability compared to other sensors.

2.2 Titanium Based Oxide Materials for Humidity Sensors

Titanium oxide (TiO_2) is a most popular metal oxide semiconductor material which has enormous applications in environmental cleaning and protection, solar cells, photocatalysis, and chemical sensors. Anatase (tetragonal), rutile (tetragonal), and brookite (orthorhombic) are the three most available crystallographic structures of TiO_2 crystal. The catalytic performance, photocatalytic activities, as well as sensing properties of TiO_2-based devices are influenced by the differences in crystallographic structures. The devices were fabricated by evaporating metal contacts on a SiO_2 layer thermally grown on a silicon substrate. The humidity sensing characteristics of $CdTiO_3$ nanofibers prepared by the electrospinning method were analyzed by Imran et al. [13].

$Bi_{0.5}(Na_{0.85}K_{0.15})_{0.5}Ti_{0.97}Zr_{0.03}O_3$ (BNKTZ) sensing materials were successfully synthesized via a simple metal–organic decomposition method by Wang et al. [14] and their humidity sensing properties, which are listed in Table 2, were successfully analyzed.

Titanium Based Sensor Material	Method of Synthesis	Response Time (s)	Recovery Time (s)	Hysteresis (%)	Ref.
$CdTiO_3$ nanofibers	Electrospinning	4	6	≈7	[13]
Bi0.5(Na0.85K0.15)0.5Ti0.97Zr0.03O3 (BNKTZ)	Metal–organic decomposition	18	60	4	[14]
Develop a novel humidity sensor based on $Na_2Ti_3O_7$ nanowires	Hydrothermal	4	5	-	[15]
Pure TiO_2 and KCl-doped TiO_2 nano fibers with different crystallographic structures	Electro-spinning and calcinations	3	3	-	[16]
$Bi_{0.5}K_{0.5}TiO_3$ (BKT) powder	Chemical solution method	12	25	3	[17]
Pure $CaCu_3Ti_4O_{12}$ and Mg-doped $CaCu_3Ti_4O_{12}$	Conventional solid state method	Very slow (>882)	Very slow (>234)	-	[18]

Barium titanate ($BaTiO_3$) nanofiber	Electro-spinning and calcinations	<5	<4	5	[19]
Bi0.5Na0.5TiO3–Bi0.5K0.5TiO3 (BNT–BKT) powder	Metal-organic decomposition	20	60	4	[20]
TiO_2 and polystyrene sulfonic sodium (NaPSS) composite films on the alumina substrate	Dip-coating	178.1 (for pure TiO_2) 774.9 (for pure ZTNA composites)	5.9 (for pure TiO_2) 19.7 (for pure ZTNA composites)	-	[21]
ZnO nanorods in core deposited of TiO_2 in shell (ZnO/TiO_2) on glass substrates	Hydrothermal growth (reparation of ZnO nanorods) and sol-gel (deposition of anatase TiO_2 shells)	990.6	35.4	High	[22]
Electrospun TiO_2 nanofiber with metallic electrodes: titanium (Ti), nickel (Ni), and gold (Au)	Evaporating metal contacts on SiO_2 layer thermally grown on silicon substrate	3 4 7	5 7 13	3 5 15	[23]

Table 2. Different types of titanium oxide-based humidity sensors and their synthesis methods.

The variation of electrical characteristics (resistance, capacitance, sensitivity, response time, hysteresis, stability) with the variation of frequency, temperature and relative humidity of titanium-based sensor materials are explained in the following subsections.

2.2.1. Resistance or Impedance Variation with Relative Humidity

Like other humidity sensors, the resistance or impedance of titanium oxide-based humidity sensors also decreases with increasing RH. The effect of different metallic electrodes (e.g., Ti, Ni, and Au) on the humidity sensing properties of electrospun TiO_2 nanofibers is different [13]. The impedance of three TiO_2 nanofibers sensors with different metallic electrodes such as Ti, Ni, and Au becomes smaller as the RH increases from 40% to 90% RH at room temperature. The size of the impedance range decrease is quite different for different electrode materials, and it is 300–38 MU for Ni-electrode sensor, 381–4.7 MU for Ti-electrode sensor and 199–0.03 MU for a Au-electrode sensor in the humidity range from 40% to 90% RH. Ti-electrode and Ni-electrode sensors show quite linear behavior in this range; however the Au-electrode sensor offers low impedance with significantly poorer linear behavior as compared to the other two metallic electrode sensors. The Ti-electrode has shown noticeably higher sensitivity of (7.53 MU/%RH) compared to Ni-(5.29 MU/%RH) and Au-(4.01 MU/%RH) electrode sensors at 100 Hz.

2.2.2. Effect of Frequency on Resistance-RH Characteristics

The impedance or resistance of titanium oxide-based humidity sensors decreases as RH increases with operating frequency and it is influenced significantly by the frequency in different humidity ranges. Maximum linearity but high resistance or impedance is observed at lower operating frequency in the whole RH range for all these humidity sensors. However, at high operating frequency the best linearity is observed only at higher RH range and the impedance or resistance becomes independent of the RH at lower frequencies. The observed flat or independent impedance curves are attributed to dielectric phenomena. At higher frequency, the adsorbed water molecules are difficult to polarize, which leads to an insignificant decrease in impedance. Most of these materials show their best impedance-RH curve linearity at nearly 100 Hz.

The impedance value with RH at different frequencies for KCl-doped TiO_2 nanofibers calcinated at 600 °C [16], for a BKT humidity sensor [17], for a BNT–BKT sensor [20], and for a BNKTZ humidity sensor [14] is influenced especially at low RH, and the impedance decreases

remarkably with an increase of the frequency. The high humidity sensitivity and the good linearity of the impedance vs. RH curve appear in the low frequency region, and the best linearity appears at 100 Hz. The BNT–BKT sensor impedance decreases remarkably with increasing frequency at low RH, and the impedance difference between two adjacent curves becomes progressively smaller with increasing RH. A similar kind of behavior was also found in the other nanomaterials such as $CdTiO_3$ nanofiber [13], $BaTiO_3$ nanofiber [19], and $Na_2Ti_3O_7$ nanowire sensors [15].

2.2.3. Effect of Temperature on Resistance-RH Characteristics

Temperature is another important key parameter for humidity sensors because humidity always depends on the ambient temperature. The impedance decreases with increasing ambient temperature since the applied thermal energy activates the mobile charge carriers within a stable water layer. The average temperature coefficient between 15 and 35 °C is about −0.2% RH/°C in the humidity range of 11%–95% RH [15].

2.2.4. Effect of Frequency on Capacitance-RH Characteristics

It has been noticed that the capacitance increases with an increase in RH at low frequencies from 50 to 100 Hz. However, at high frequencies, greater than 1 kHz, the capacitance values become very low at any RH and are almost independent of the RH [19]. A relation between capacitance and relative humidity at different frequencies for TiO_2 nanofiber depicts the variation of capacitance with frequency under different absolute humidity conditions [13]. It can be noticed that the capacitance increases gradually as the RH increases, but it changes rapidly by lowering the frequency. At high RH values, the capacitance increases as the frequency decreases. At higher frequency, i.e., >1 kHz, the capacitance becomes very small and hardly changes with humidity.

2.2.5. Response and Recovery Time Analysis

Response and recovery times of different titanium oxide-based humidity sensors are listed in Table 2. From the above data it is observed that the KCl-doped TiO_2 nanofiber humidity sensor has the lowest response and recovery time.

2.2.6. Hysteresis Characteristics Analysis

Titanium-based humidity sensors in general have lower hysteresis and the values are illustrated in Table 2. It is evident that the Ti-electrode sensor has lower hysteresis values as compared with those for the Ni-electrode and Au-electrode sensors [23]. The ZnO/TiO_2 core/shell nanorod sensor has high hysteresis, but has very good repeatability [22]. From the above results it is clear that the BKT humidity sensor has lowest hysteresis value [17].

2.2.7. Stability Analysis

The stability of titanium oxide-based humidity sensors is high at low frequency but they have high impedance values, even after exposure for up to 100 days. Considering various titanium-based materials, it has been noticed that the titanium oxide-based humidity sensors show very good stability in terms of insignificant change in impedance with increasing time up to 75% RH, and beyond that RH, the resistance or impedance varies significantly. It has also been reported that the KCl-doped TiO_2 nanofibers show better best linearity and the quickest response compared with pure anatase or rutile structures [16]. In order to explain the stability of the best titanium oxide-based humidity sensor, we select a KCl-doped TiO_2 nanofiber humidity sensor, which was exposed to air for 100 days to measure its impedances at various RH levels. Like any other sensor material, the titanium oxide-based humidity sensor materials also forms water layers with increasing RH on the surface of nanofibers by a physisorption mechanism. The mechanism of the dissociation of the doping material has an important role in a material in order to show the best performance or stability. Normally, in ceramic and porous materials, the water-related conduction occurs mainly through surface mechanisms [24]. However, for films, a large increase in electrical conductivity with increasing RH of TiO_2 nanofibers may be related to the adsorption of water molecules on the surface of the sensing film. For nanofibers, a high local charge density and a strong electrostatic field are provided by the tips and defects of the nanofibers, and this can promote the dissociation of water and ionic salt molecules [25]. In case of the KCl-doped TiO_2 nanofiber humidity sensor, the dissociation of KCl supplies protons and ions (such as H^+, H_3O^+, K^+, Cl^-) as charge carriers for the hopping transport. In this system, H_3O^+ may be hydrated in the presence of sufficient adsorbed water since hydration of H_3O^+ is energetically favored in liquid water [13, 16, and 26]. Although the initial and final states are the same (water molecule and hydronium ion) according to the ion transfer mechanism [27], the transfer of hydronium (H_3O^+) is quite easy as the energy is equivalent. Simultaneously, KCl

dissolves in the adsorbed water and plays a major role in carrier conduction by dissociating into K^+ and Cl^- ions. However, when the RH is increased further, more of the ionic salt (*i.e.*, KCl) dissociates into free ions (*i.e.*, K^+ and Cl^-). This enhances the transfer process of the KCl-doped TiO_2 nanofibers, and as a result, the linearity of the impedance *vs.* RH curve improves significantly by doping KCl in the whole range of 11%–95% [16].

Qi et al. [16] had also speculated that the crystallographic structure may change the specific surface area (i.e., surface-to-volume ratio) of their KCl-doped TiO_2 nanofibers, but all their samples exhibited relatively low specific surface areas. Hence, eventually, they considered dissociation phenomena along with crystallographic structure in order to explain the performance or linearity of TiO_2- and KCl-doped TiO_2 nanofiber sensors. According the report by Qi et al., the mixed structures revealed more defects of the nanofibers compared with pure anatase or rutile, which led to the dissociation of more molecules (H_2O and KCl) and resulted in an increase of carrier concentration, which eventually improved the sensing performance of the nanofibers [16, 25].

2.3 Zink Based Oxide Materials for Humidity Sensors

Zinc oxide (ZnO) is very popular semiconductor materials in the field of humidity sensor applications. High chemical and physical stability, good sensitivity as well as fast response and recovery time, and high surface to volume ratio are the main salient features of ZnO-based humidity sensors. However, the higher hydrophobicity of ZnO materials is an inherent drawback, but this can be overcome by using different doping techniques. Different kinds of zinc oxide-based materials for humidity sensors and their synthesis techniques are listed in Table 3.

The electrical characteristics (resistance, capacitance, sensitivity, response time, hysteresis, stability) changes with the variation of frequency, temperature and relative humidity of zinc-based sensor materials are explained in the following subsections.

Zink Based Sensor Material	Method of Synthesis	Response Time (s)	Recovery Time (s)	Hysteresis (%)	Ref.
Flower-like ZnO nanorods on a ceramic	Screen-printing	5	10	2	[28]

substrate with silver-palladium (Ag–Pd) interdigital electrodes					
KCl-doped ZnO nanofibers	Electrospinning	2	1	-	[29]
ZnO nanofibers and LiCl-doped ZnO composite fibers on ceramic substrates with carbon interdigital electrodes	Screen-printing	3	6	2	[30]
KCl-doped Cu–Zn/CuO–ZnO (KCZ/CZN) nanoparticles	Wire electrical explosion (WEE)	40	50	4	[31]
High pure ZnO colloidal nanocrystal clusters (CNCs)	Modified hydrolyzation	110	80	-	[32]
Nanocrystalline zinc tungstate ($ZnWO_4$) (nanoparticles, nanorods)	Precipitation or hydrothermal	3	50	5.5	[33]
ZnO and In_2O_3 thin films on SiO_2/Si substrates with interdigitated Pt signal electrodes	Radio-frequency sputtering	15	40	4	[34]
Mn-doped ZnO nanopowders	Sol-gel	6	20	4.36	[35]
ZnO nanorods (Capacitive type)	Thermal decomposition	70	20	-	[36]
Porous zinc aluminate	Homogeneous co-	15	30	2	[37]

($ZnAl_2O_4$) spinel nanorods	precipitation approach followed by a heat treatment at 900 °C				
ZnO colloid spheres (coated on quartz crystal microbalance, QCM)	Self-assembly	38	18	-	[38]

Table 3. Different types of zinc oxide-based humidity sensors and their synthesis methods.

2.3.1. Resistance or Impedance Variation with Relative Humidity

Like other sensor materials ZnO-based materials have shown decreasing resistance or impedance with increasing RH. The doping materials and their structure or synthesis techniques play important roles in the resistance or impedance vs. RH characteristics. The KCl-doped Cu–Zn/CuO–ZnO nanoparticles (KCZ/CZNs) show much better linearity of the correlation curve than that of undoped CZ/CZNs on a semi-logarithmic scale. It has been found that the impedance of KCZ/CZNs decreases linearly by about four orders of magnitude as the RH increases from 11% to 95%. Similar behavior was also found in the KCl-doped ZnO nanofiber material [29] and LiCl-doped ZnO nanofibers [30]. In both cases, the doped ZnO nanofibers exhibited greatly improved sensitivity with lower impedance and higher linearity compared to a pure ZnO sample. Addition of Mn in ZnO_2 enhances its humidity sensing characteristics. The 6 at % Mn-doped ZnO gives the best linearity and highest sensitivity.

2.3.2. Effect of Frequency on Resistance-RH Characteristics

The resistance or impedance of the ZnO-based humidity sensors decreases with increasing RH and it is more pronounced at higher frequency. Furthermore, the change in impedance between the operating frequencies becomes progressively smaller with increasing RH. The probable reason for this result is that at higher frequencies, the adsorbed water cannot be polarized so fast and thus, the dielectric phenomenon does not appear. Most of the ZnO-based sensors, such as

flower-like ZnO nanorods [28], KCl-doped ZnO nanofibers [31], LiCl-doped ZnO nanofibers [30], KCZ/CZNs [31], porous $ZnAl_2O_4$ nanorods [37] and ZnO nanotips [39], shows the best linearity in the impedance *vs.* RH curve at nearly 100 Hz.

The impedance of the porous $ZnAl_2O_4$ nanorod-based sensor decreases with increasing RH at all measuring frequencies [37]. Especially, at low frequency, e.g., at 40 Hz, it changes from 7×10^3 to 70 kΩ as RH varies from 11% to 95%, implying a relatively high sensitivity. Although the impedance was nonlinear with increasing RH, the impedance followed a logarithmic increase with increasing RH and exhibited a good linear log (impedance) relationship to RH in the 11%–95% RH range, as shown by Cheng et al. Moreover, the slope of the linear fit curves decreased from −0.02309 to −0.00619 with the increase of measurement frequency from 40 Hz to 1 MHz, clearly indicating a decrease in sensitivity. On the other hand, ZnO nanotip sensors show an impedance change by six orders of magnitude at 100 Hz compared to operating at a frequency of 100 kHz measured at 1 V [39]. From the impedance-RH curve of the ZnO nanotips sensor, it can be clearly seen that the impedance of the film decreases remarkably at higher frequency in the low RH range, and the impedance difference between the two working frequencies becomes progressively smaller with increasing RH.

2.3.3. Effect of Frequency on Capacitance-RH Characteristics

The capacitance variation is found to be more at the low frequency range and its effect becomes slow at higher frequency range. This happens due to the sluggish change in electrical field direction at low frequency which strongly affects the space–charge polarization of adsorbed water. A higher RH means more the water molecules are adsorbed and the polarization is stronger, and thus a larger dielectric constant or capacitance value is obtained. However, at a high frequency the polarization of the water cannot catch up with the faster change in electric field direction, and hence the dielectric constant or capacitance value becomes smaller and independent of RH.

The properties of capacitance vs. frequency at different RH values for flower-like ZnO nanorod [28], porous ZnAl2O4 nanorod [37] and ZnO/Si-NPA [40] sensor materials shows flower-like ZnO nanorod sensor displays a large capacitance change at lower frequency (40 and 100 Hz) in the range of 54%–95% RH. The porous $ZnAl_2O_4$ nanorod sensor shows a large change of

capacitance at a frequency lower than 100 Hz in the 55%–95% RH range. The ZnO/Si-NPA sensor shows the best capacitance-RH characteristics at 1 kHz in the 55%–95% RH range.

2.3.4. Response and Recovery Time Analysis

The response and recovery time of the different ZnO-based humidity sensors are listed in Table 3. It has been noticed that the response and recovery times of the KCl-doped ZnO nanofiber sensor is remarkably low compared to any other humidity sensor material.

2.3.5. Hysteresis Characteristics

The hysteresis of ZnO-based humidity sensors are listed in Table 3. Most of the ZnO-based humidity sensors show excellent hysteresis loss in their impedance or capacitance-RH plots (near to 2%).

2.3.6. Stability Analysis

In the low humidity range, there was almost no change observed even up to 60 days in the impedance or capacitance values, which directly confirms the good stability of ZnO-based humidity sensors. A slight fluctuation is observed in the higher RH range above 50% RH. The impedance stability of the ZnO nanotip-based humidity sensor in a wide range of RH values was observed up to 30 days at 100 Hz [39], indicating good stability and durability of the sensor. A good long term stability was also observed for a ZnO/Si-NPA cauliflower humidity sensor, which showed insignificant change in capacitance values up to 50 days exposure to ambient air at temperatures in between 19 °C and 30 °C [40].

3. Applications and Scopes of Humidity Sensors

After analyzing the different electrical characteristics of different doping concentrations of different materials, it is very important to study the wide range of applications where humidity sensors are used. Humidity sensors have several applications and scopes such as medical, agricultural, mineral, fuel, aerospace, high-energy physics, and food storage of humidity sensors .The typical humidity sensors, including flexible micro-humidity sensors with different humidity or moisture sensing mechanisms, operating temperatures and different humidity ranges have been used in wide range of applications.

4. Conclusions

Humidity sensors for measuring relative humidity based on different types of materials, including tin, titanium and zinc have been reviewed extensively. The electrical properties of humidity sensors such as resistance and capacitance, the effects of temperature, frequency, and relative humidity, sensitivity, response time, hysteresis and stability have been compared in detail for different metal-oxide materials.For different sensor materials, the electrical properties are changed significantly with the doping concentration of different materials, film thickness of the substrate and the resulting morphological changes. From the above analysis it has been observed that the different doping materials for humidity sensors like tin, titanium and zinc show their best linearity at the optimized frequency of 100 Hz. Hysteresis is one of the most important parameters for all sensors. For practical applications a sensor must have minimum hysteresis value. In this review article the best hysteresis value for different humidity sensor doping materials like tin, titanium and zinc were 3%, 3% and 1.9%, respectively. The response and recovery times are also an important parameter for all humidity sensors. The response and recovery times of different doped humidity sensors have been critically reviewed. The best response times for tin, titanium and zinc doped sensor materials were 5, 3 and 2 s, respectively, and best recovery time of these sensor materials was 6, 3 and 1 s, respectively. The selection of sensor material based on hysteresis, response time, recovery time and stability is listed in Table 4. In ordered to select a best humidity sensors based on different materials, according to the F-value and T-test by statistical analyses, we grade three categories such as good (i.e., >3% for hysteresis, >19 s for response and recovery times), very good (i.e., 2%–3% for hysteresis, 6–19 s for response and recovery times) and excellent (i.e., <3% for hysteresis, <6 s for response and recovery times).

Sensor Material Based on	Response Time	Recovery Time	Hysteresis	Stability
Tin	Excellent	Excellent	Very good	Good
Titanium	Excellent	Excellent	Very good	Very good
Zinc	Excellent	Excellent	Excellent	Excellent

Table 4. Different sensor materials based on their best electrical response quality

Since stability is the change in resistance or capacitance curves with respect to humidity over a long time, according to observation, it is directly graded as good, very good and excellent according to our flatness for a particular humidity sensor material. Based on our review, it has been found that the zinc oxide-based sensor material is the best for humidity sensor design due to its extremely low hysteresis loss, minimum response and recovery times, and excellent stability. Humidity sensors have a tremendous range of applications in different important fields such as biomedicine, SHM, food processing and storage, medicine, ecology, agriculture, mineral processing, fuel quality control, aerospace, the electronics industry and high-energy physics applications. The humidity conditions, including temperature and % RH, are also very important for different manufacturing or processing sectors as well as their specific areas. Therefore, the development of more integrated humidity sensors for multi-field applications would be highly fascinating topic for the new generation of humidity sensing devices. The review has provided examples that represent the diversity of applications and the demand for RH or moisture sensors in industry today. Therefore, it can be expected that different advanced humidity sensors made of hybrid or doped materials using the latest nanotechnology will be able to monitor a wide range of application sectors.

5. References

1. Song, X.; Qi, Q.; Zhang, T.; Wang, C. A humidity sensor based on KCl-doped SnO_2 nanofibers. *Sens. Actuators B Chem.* **2009**, *138*, 368–373.
2. Wiederhold, P.R. *Water Vapor Measurements*; Marcel Dekker: New York, NY, USA, **1997**.
3. Chen, Z.; Lu, C. Humidity Sensors: A Review of Materials and Mechanisms. *Sens. Lett.* **2005**, *3*, 274–295.
4. Hamid Farahani, Rahman Wagiran, Mohd Nizar Hamidon, Humidity Sensors Principal, Mechanism, and Fabrication Technologies: A Compressive Review; *Sensors***2014**, 14, 7881-7939.
5. Ashis Tripathy, Sumit Pramanik, Jongman Cho, Jayasree Santhosh and Noor Azuan Abu Osman, Role of Morphological Structure, Doping, and Coating of Different Materials in the Sensing Characteristics of Humidity Sensors; *Sensors***2014**, *14*, 16343-16422.
6. Chu, J.; Peng, X.; Feng, P.; Sheng, Y.; Zhang, J. Study of humidity sensors based on nanostructured carbon films produced by physical vapor deposition. *Sens. Actuators B Chem.* **2013**, *178*, 508–513.
7. Hu, S.; Chen, H.; Fu, G.; Meng, F. Humidity sensitive properties of K^+-doped SnO_2–$LiZnVO_4$. *Sens. Actuators B Chem.* **2008**, *134*, 769-772.
8. Hu, S.; Fu, G. Humidity-sensitive properties based on liquid state $LiZnVO_4$-doped SnO_2.
9. *Sens. Actuators A Phys.* **2010**, *163*, 481-485.
10. Anbia, M.; Fard, S.E.M. Humidity sensing properties of La^{3+} and K^+ co-doped $Ti_{0.9}Sn_{0.1}O_2$ thin films. *J. Rare Earths* **2011**, *29*, 668-672.
11. Parthibavarman, M.; Hariharan, V.; Sekar, C. High-sensitivity humidity sensor based on SnO_2 nanoparticles synthesized by microwave irradiation method. *Mater. Sci. Eng. C Mater. Biol. Appl.* **2011**, *31*, 840-844.
12. Anbia, M.; Moosavi Fard, S.E. A humidity sensor based on KCl-doped nanoporous $Ti_{0.9}Sn_{0.1}O_2$ thin films prepared by the sol-gel method. *Sci. Iran.* **2012**, *19*, 546–550.

13. Bauskar, D.; Kale, B.B.; Patil, P. Synthesis and humidity sensing properties of $ZnSnO_3$ cubic crystallites. *Sens. Actuators B Chem.* **2012**, *161*, 396–400.
14. Imran, Z.; Batool, S.S.; Jamil, H.; Usman, M.; Israr-Qadir, M.; Shah, S.H.; Jamil-Rana, S.; Rafiq, M.A.; Hasan, M.M.; Willander, M. Excellent humidity sensing properties of cadmium titanate nanofibers. *Ceram. Int.* **2013**, *39*, 457–462.
15. Wang, R.; Wang, D.; Zhang, Y.; Zheng, X. Humidity sensing properties of $Bi_{0.5}$ $(Na_{0.85}K_{0.15})_{0.5}Ti_{0.97}Zr_{0.03}O_3$ microspheres: Effect of A and B sites co-substitution. *Sens. Actuators B Chem.***2014**, *190*, 305–310.
16. Zhang, Y.; Fu, W.; Yang, H.; Li, M.; Li, Y.; Zhao, W.; Sun, P.; Yuan, M.; Ma, D.; Liu, B.; *et al*.
17. A novel humidity sensor based on $Na_2Ti_3O_7$ nanowires with rapid response-recovery. *Sens. Actuators B Chem.* **2008**, *135*, 317–321.
18. Qi, Q.; Feng, Y.; Zhang, T.; Zheng, X.; Lu, G. Influence of crystallographic structure on the humidity sensing properties of KCl-doped TiO_2 nanofibers. *Sens. Actuators B Chem.* **2009**, *139*, 611–617.
19. Zhang, Y.; Zheng, X.; Zhang, T.; Gong, L.; Dai, S.; Chen, Y. Humidity sensing properties of the sensor based on $Bi_{0.5}K_{0.5}TiO_3$ powder. *Sens. Actuators B Chem.* **2010**, *147*, 180–184.
20. Li, M.; Chen, X.L.; Zhang, D.F.; Wang, W.Y.; Wang, W.J. Humidity sensitive properties of pure and Mg-doped $CaCu_3Ti_4O_{12}$. *Sens. Actuators B Chem.* **2010**, *147*, 447–452.
21. He, Y.; Zhang, T.; Zheng, W.; Wang, R.; Liu, X.; Xia, Y.; Zhao, J. Humidity sensing properties of $BaTiO_3$ nanofiber prepared via electrospinning. *Sens. Actuators B Chem.* **2010**, *146*, 98–102.
22. Zhang, Y.; Zheng, X.; Zhang, T. Characterization and humidity sensing properties of
23. $Bi_{0.5}Na_{0.5}TiO_3$–$Bi_{0.5}K_{0.5}TiO_3$ powder synthesized by metal-organic decomposition. *Sens.*
24. *Actuators B Chem.* **2011**, *156*, 887–892.
25. Sun, A.; Huang, H.; Chu, C.; Li, Y. Effect of the pore size of TiO_2 porous film on humidity sensitive properties of TiO_2/NaPSS composite films. *Sens. Actuators B Chem.* **2011**, *160*, 1335–1339.

26. Gu, L.; Zheng, K.; Zhou, Y.; Li, J.; Mo, X.; Patzke, G.R.; Chen, G. Humidity sensors based on ZnO/TiO_2 core/shell nanorod arrays with enhanced sensitivity. *Sens. Actuators B Chem.* **2011**, *159*, 1–7.
27. Batool, S.S.; Imran, Z.; Israr Qadir, M.; Usman, M.; Jamil, H.; Rafiq, M.A.; Hassan, M.M.; Willander, M. Comparative Analysis of Ti, Ni, and Au Electrodes on Characteristics of TiO_2 Nanofibers for Humidity Sensor Application. *J. Mater. Sci. Technol.* **2013**, *29*, 411–414.
28. Kulwicki, B.M. Humidity Sensors. *J. Am. Ceram. Soc.* **1991**, *74*, 697–708.
29. Schaub, R.; Thostrup, P.; Lopez, N.; Lagsgaard, E.; Stensgaard, I.; Nurskov, J.K.; Besenbacher, F. Oxygen vacancies as active sites for water dissociation on rutile TiO_2(110). *Phys. Rev. Lett.* **2001**, *87*, 2661041–2661044.
30. Oliveira, O.N., Jr.; Riul, A., Jr.; Leite, V.B. Water at interfaces and its influence on the electrical properties of adsorbed films. *Braz. J. Phys.***2004**, *34*, 73–83.
31. Knauth, P.; di Vona, M.L. Introduction and Overview: Protons, the Nonconformist Ions. In *Solid State Proton Conductors: Properties and Applications in Fuel Cells*; John Wiley & Sons, Ltd.: Chichester, UK, 2012; pp. 1–4.
32. Qi, Q.; Zhang, T.; Yu, Q.; Wang, R.; Zeng, Y.; Liu, L.; Yang, H. Properties of humidity sensing ZnO nanorods-base sensor fabricated by screen-printing. *Sens. Actuators B Chem.***2008**, *133*, 638–643.
33. Qi, Q.; Zhang, T.; Wang, S.; Zheng, X. Humidity sensing properties of KCl-doped ZnO nanofibers with super-rapid response and recovery. *Sens. Actuators B Chem.***2009**, *137*, 649–655.
34. Wang, W.; Li, Z.; Liu, L.; Zhang, H.; Zheng, W.; Wang, Y.; Huang, H.; Wang, Z.; Wang, C. Humidity sensor based on LiCl-doped ZnO electrospun nanofibers. *Sens. Actuators B Chem.* **2009**, *141*, 404–409.
35. Qi, Q.; Zhang, T.; Zeng, Y.; Yang, H. Humidity sensing properties of KCl-doped Cu–Zn/CuO–ZnO nanoparticles. *Sens. Actuators B Chem.* **2009**, *137*, 21–26.
36. Si, S.; Li, S.; Ming, Z.; Jin, L. Humidity sensors based on ZnO Colloidal nanocrystal clusters. *Chem. Phys. Lett.* **2010**, *493*, 288–291.

37. You, L.; Cao, Y.; Sun, Y.F.; Sun, P.; Zhang, T.; Du, Y.; Lu, G.Y. Humidity sensing properties of nanocrystalline $ZnWO_4$ with porous structures. *Sens. Actuators B Chem.* **2012**, *161*, 799–804.
38. Liang, Q.; Xu, H.; Zhao, J.; Gao, S. Micro humidity sensors based on ZnO–In_2O_3 thin films with high performances. *Sens. Actuators B Chem.* **2012**, *165*, 76–81.
39. Peng, X.; Chu, J.; Yang, B.; Feng, P.X. Mn-doped zinc oxide nanopowders for humidity sensors. *Sens. Actuators B Chem.* **2012**, *174*, 258–262.
40. Chen, L.; Zhang, J. Capacitive humidity sensors based on the dielectrophoretically manipulated ZnO nanorods. *Sens. Actuators A Phys.* **2012**, *178*, 88–93.
41. Cheng, B.; Ouyang, Z.; Tian, B.; Xiao, Y.; Lei, S. Porous $ZnAl_2O_4$ spinel nanorods: High sensitivity humidity sensors. *Ceram. Int.* **2013**, *39*, 7379–7386.
42. Xie, J.; Wang, H.; Lin, Y.; Zhou, Y.; Wu, Y. Highly sensitive humidity sensor based on quartz crystal microbalance coated with ZnO colloid spheres. *Sens. Actuators B Chem.* **2013**, *177*, 1083–1088.
43. Biswas, P.; Kundu, S.; Banerji, P.; Bhunia, S. Super rapid response of humidity sensor based on MOCVD grown ZnO nanotips array. *Sens. Actuators B Chem.* **2013**, *178*, 331–338.
44. Wang, L.L.; Wang, H.Y.; Wang, W.C.; Li, K.; Wang, X.C.; Li, X.J. Capacitive humidity sensing properties of ZnO cauliflowers grown on silicon nanoporous pillar array. *Sens. Actuators B Chem.***2013**, *177*, 740–744.

Chapter: 14

Optical analysis of Cadmium doped Selenium-rich Glassy Chalcogenide

[1]Arvind Kumar Verma, [2]R. K. Shukla and [3] Susheel Kumar Singh

[1]Department of Physics, SRMCEM Lucknow, UP, India
[2]Department of Physics, University of Lucknow, Lucknow, UP, India
[3]Department of Physics, HLYB PG College, Lucknow, UP India
E-mail: susheelsingh489@gmail.com

Abstract: In my recent work, investigating the influence of addition of cadmium (Cd) with decreasing atomic wt. % of Selenium (Se) at constant atomic wt. % of Tellurium (Te) on the optical studies of the $Se_{90-x}Te_{10}Cd_x$ (x = 0, 10, 20 at. %) chalcogenide alloys. Spectral dependence of the absorption spectra recorded in the range of 200 1800 nm for as-prepared and thermally annealed samples in normal wavelength scanning mode is shown by UV/VIS/NIR spectroscopy. Optical band gap (E_g) of the as-prepared sample increases and thermally annealed sample decreases with increasing photon energy. Absorption coefficient and absorption constant of the as-prepared and annealed samples S1, S2, S3 decrease with increasing Cd% in the synthesized materials.

Keywords: $Se_{90-x}Te_{10}Cd_x$ (x = 0, 10, 20 at. %) powder; UV/VIS/NIR;

1. Introduction

This work is focussed on discussing the optical studies of chalcogenide alloys because any glass is free from defects like bubbles or imperfections; it can be considered as a perfect material for propagation of light [1]. Chalcogenide glasses are oxygen-free inorganic glasses containing one or more kinds of chalcogen elements (Te, Se) [2]. Due to semi-metallic nature and a high degree of crystallinity, Te-rich alloys limits, the glass forming ability whereas Se-rich alloys show a semiconducting nature [3]. The main difference between Se and Te is the nature of the bonding responsible for the interchain cohesion. Chalcogenide glasses are generally less strong more weakly bonded materials than oxide glasses. The change in the optical properties of the composition may be explained by assuming that Te atoms act as an impurity centre in the mobility gap [4-7]. The Se-Te alloys exhibit higher photosensitivity, greater hardness, better thermal stability, and lower ageing effects [9]. Se-Te based glasses, due to their extreme

tendency to crystallise, have found applications as phase change materials for optical storage in the Digital Versatile Disk (DVD) technology [10, 11]. These glasses are being studied mostly for applications as passive devices (lenses, windows, fibres) and also attractive for the preparation of active devices such as Laser fibre amplifiers and nonlinear components [12]. Photocells, rectifiers, memory, and switching devices due to their unique electrical, thermal, and optical properties are the technological applications of the chalcogenide glasses [13].

It is well-known that the addition of metallic additives to binary chalcogenide system changes their structure and new properties are expected for these alloys. From this point of view, the effect of the addition of Cd metal on the optical properties of the Se-Te binary system has been studied.

2. Experimental Setup

In the present work, Melt quenching method has been adopted to prepare $Se_{90-x}Te_{10}Cd_x$(x = 0, 10, 20 at. %) chalcogenide alloys to obtained an amorphous structure from 99.999% pure Se, Te and Cd elements. The exact amount of alloying elements were weighed according to their atomic weight percentages using an electronic balance with the least count of a 10^{-4} gram and then placing into ultra-cleaned quartz ampoules (length ≈ 5 cm and internal diameter ≈ 8 mm). The ampoules were evacuated and sealed in a vacuum of 10^{-3} Torr with an oxygen-hydrocarbon flame torch using rotary pumps to avoid reaction of alloying elements with oxygen at a higher temperature. The sealed ampoules were heated in a furnace at the rate of 4^0C/min. The temperature was raised up to 1000 ^{0}C and was maintained for 10 hours. During the heating process, the ampoules were constantly rocked by a ceramic rod to ensure the homogeneity of the alloying materials. The ampoules with molten materials were rapidly quenched into the ice-cooled water to allow glass formation and to avoid crystallisation. The ingots of chalcogenide materials were taken out from ampoules by breaking them. The obtained melt was ground into powder form and filtered to obtain homogeneous alloys. The obtained as-prepared sample is further annealed for 4 hours at a 150 ^{0}C fixed temperature to remove internal stress to make the material less brittle. After that bulk samples of as-prepared and thermally annealed was compressed into pellets form having a diameter of 13 mm and thickness of about 1-2 mm under a uniform pressure of 5 tons using a hydraulic press machine. Bulk/pellets made from $Se_{90-x}Te_{10}Cd_x$ (x = 0, 10, 20 at. %) alloys were named as S1 ($Se_{90}Te_{10}$), S2 ($Se_{80}Te_{10}Cd_{10}$), and S3 ($Se_{70}Te_{10}Cd_{20}$). Physical dimensions of each pellet were measured with the help of digital screw-

gauge (BAKER-Type J02, 7301) having least count 0.01 mm.Optical studies were recorded using JASCO V670 UV/VIS/NIR spectrophotometer in the spectral range of 200 to 1000 nm using a quartz cuvette with an optical path of 1 cm for all samples dissolved in ethyl alcohol at normal incidence.

3. Results and Discussion

1. Absorption coefficient

Absorption coefficient (α) is the property of a material which defines the amount of light absorbed by it and depends upon photons energy as well as the nature of the material [22]. The absorption coefficient (α) has been evaluated by Beer-Lambert law (α =2.303A/t), where A is optical absorption which depends on wavelength and density of point defects and (t) is light path length (10 mm) [23].Figure 1 (a, b) shows the absorption coefficient of as-prepared and annealed bulk sample of S1, S2, S3 for $Se_{90-x}Te_{10}Cd_x$(x = 0, 10, 20 at. %) with incident photon energy range. The absorption coefficient of the as-prepared samples observed in UV regions and gradually decrease with increasing frequency for Cd-doped sample S2, S3 with respect to undoped sample S1, whereas in thermally annealed samples absorption coefficient observed in NIR regions and continuously decrease with increasing frequency, originates due to defects and impurities whose shape and magnitude depends on the purity, thermal history and preparation conditions [24, 25].

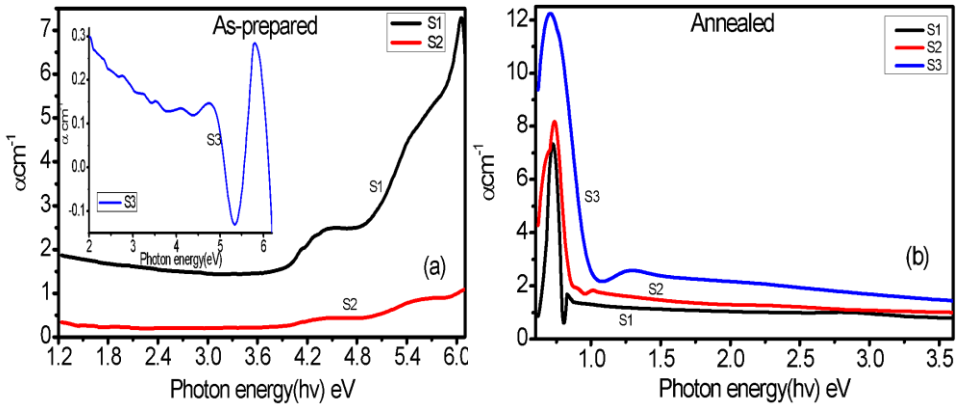

Fig. 1 (a, b) Absorption coefficient for as-prepared and annealed samples S1, S2, S3 of $Se_{90-x}Te_{10}Cd_x$(x=0, 10, 20 at. %) alloys

2. Optical Bandgap

The energy at which electron and hole pair is generated is called optical band gap energy. The high absorption region determines the optical band gap energy. The optical energy gap is defined

as the intercept of the plot of $(\alpha h\nu)^{1/2}$ against hν. Figure 2 (a,b) shows the optical band gap of as-prepared and thermally annealed sample S1, S2, S3 for $Se_{90-x}Te_{10}Cd_x$ (x = 0, 10, 20 at.%) by the direct transition.

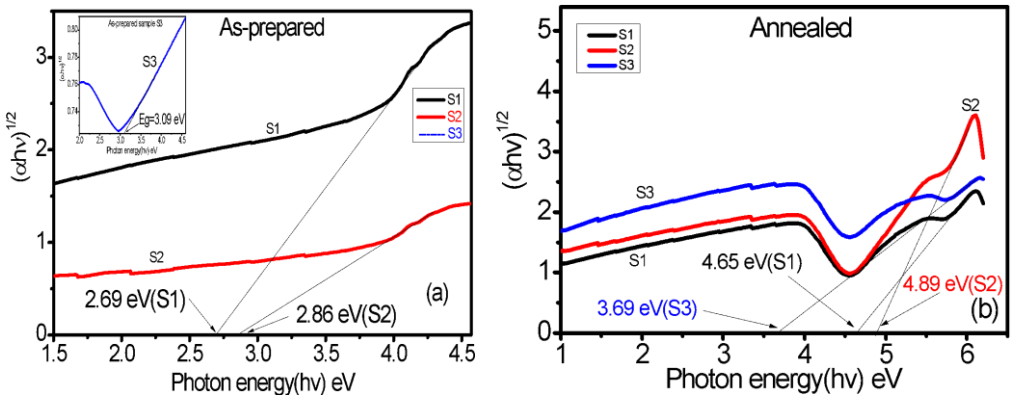

Fig. 2(a, b) Optical band gap for as-prepared and annealed samples S1, S2, S3 of $Se_{90-x}Te_{10}Cd_x$(x = 0, 10, 20 at. %)

The increment in the optical band gap with increasing Cd concentration in the as-prepared sample S1, S2 and S3 may be due to the reduction in the disorder and decrease in density of defect states [26]. Reduction in the value of measured optical band gap for thermally annealed sample S3 with respect to undoped sample S1 due to the increment of charged defects in the band tail regions, which leads to reducing the optical band gap [27]. The expected value of optical band gap for as-prepared and thermally annealed sample S1, S2, S3, are given in Table 1.

3. Absorption constant

Absorption constant indicates the amount of absorption loss when electromagnetic wave propagates through the sample. The variations of absorption constant can be related to the variation of optical transmittance. Figure 3 (a, b) shows the absorption constant of the as-prepared and thermally annealed sample of $Se_{90-x}Te_{10}Cd_x$(x = 0, 10, 20 at. %) for S1, S2, S3 with increasing wavelength. The decrease in absorption constant with increasing wavelength shows that the transmittance is increased. This type of behaviour is due to decrease in absorption coefficient with increasing wavelength of the incident photons.

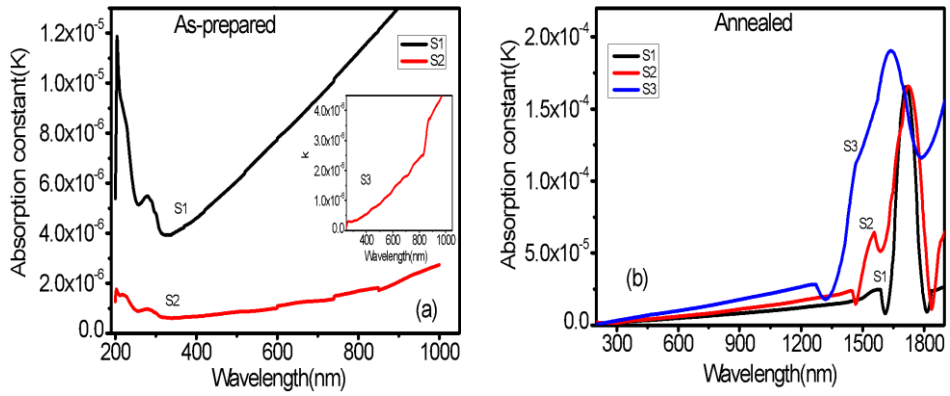

Fig. 3 (a, b): Absorption constant for as-prepared and annealed sample of $Se_{90-x}Te_{10}Cd_x$(x = 0, 10, 20 at. %) alloys

Variations of absorption loss of as-prepared and thermally annealed sample S1, S2 and S3 are observed in NIR regions. The absorption constant has been evaluated using formula $K=\lambda\alpha/4\pi$ [28, 29].

Table.1: Crystal size by XRD and Optical parameters of as-prepared and annealed $Te_{90-x}Se_{10}Cd_x$ (x = 0, 10, 20 at. %) chalcogenide

Sample	Absorption coefficient (α) in cm^{-1}		Absorption constant (K)		Optical band gap (Eg) in eV	
	As-prepared at 3.90 eV in UV regions	Annealed at 1.50 eV in NIR regions	As-prepared at 329 nm	Annealed at 900 nm	As-prepared	Annealed
S1($Se_{90}Te_{10}$)	1.566	1.131	3.95×10^{-6}	8.45×10^{-6}	2.69	4.65
S2($Se_{80}Te_{10}Cd_{10}$)	0.247	1.466	6.54×10^{-7}	1.14×10^{-5}	2.86	4.89
S3($Se_{70}Te_{10}Cd_{20}$)	0.131	2.388	3.50×10^{-7}	1.80×10^{-5}	3.09	3.69

6. Conclusion

The decrease in energy loss with an increase in Cd concentration of all as-prepared and thermally annealed samples of Se-rich $Se_{90-x}Te_{10}Cd_x$(x = 0, 10, 20 at. %) chalcogenide alloys indicates that

the charge carriers absorb more energy giving small absorption coefficient which may not be suitable for optical data storage.Variation in the optical gap due to the increment of the doping concentration of Cd in as-prepared and annealed samples. Amount of absorption loss in both samples decreases with increasing wavelength. Luminescence of as-prepared sample observed between UV and visible (red) regions while annealed sample observed only in visible (green) region with the lowest intensity due to surface defects in the synthesized materials with increasing wavelength.

References

1. M. Barsoum, Mc Graw-Hill, New York, 543 (**1977**).
2. B.T.Kolomieto, Phys. Status Solidi. 7 (**1964**) 713.
3. S.O.Nelson, J. Microwave Power and Electromagnetic Energy, 44 (2) (2010) 98-113.
4. A.N.R. Long, Adv. Phys, 31 (1981) 553-637.
5. V.K. Bhatnagar**,** K.L**.** Bhatia, J. Non-Cryst. Solids, 119(2) (1990) 214-231.
6. AN.I.Gubanov, Quantum Electron theory of amorphous conductors, New York, (1965).
7. S.K. Shinde, D.P.Dubal, G.S.Ghodake, V.J.Fulari, Synthesis and characterization of chemically deposited flower-like $CdSe_{0.6}Te_{0.4}$ thin films for solar cell application, Materials Letters,126 (2014) 17-19.
8. C. Conseil, J.C Bastien, C. B.Pledel, Optical Materials Express. 2(11) (2012) 1470.
9. J.Bartak, R.Svoboda, J. Malek, J.Applied Physics, 111094908 (2012).
10. J.Feinlei, Deneufville, J.Moss, S.C.Ovshinsky, Appl. Phys. Lett, 18 (1971) 254.
11. N.O.Yamada, E.Nishiuchi, E. Akahira, N.Takao, J. Appl. Phys, 69 (1991) 2849-2856.
12. D.Lezal, J. Pedlikova, J.Zavadila, Chalcogenide Glasses for Optical and Photonics Applications, Optoelectronics and Advanced Materials. 6 (2004) 133-137.
13. V Modgil, V.S, Rngra, J.Non-Oxide Glasses, 6(4) (2014) 69-78.
14. Y.Haoyong, X. Zhude, B. Jingyi, B.Huahui, Z. Yifan, Ethylenediamine assisted the growth of single crystal tellurium channels, Materials Letters. 59 (2005) 3779.
15. M.Brian, X.Younan, One-dimensional nanostructures of trigonal tellurium with various morphologies can be synthesized using a solution-phase approach. J. Mater. Chem. 12 (2002) 1875.
16. C.Bhattacharya, J.Datta, J. Solid State Electrochem, 11(2007) 215.
17. Md.Nasir, M. Zulfiqar, Open J. of Inorganic Nonmetallic Mat., 2 (2012) 11-17.
18. P.K.Mishra, V.Dave, R.Chandra, J.N.Prasad, A.K.Choudhary, Effect of processing parameter on structural, optical, and electrical properties of Photovoltaic chalcogenide nanostructures RF magnetron sputtered thin absorbing films, Mat. Sci. at Semiconductor Processing. 25 (2014) 307-319.
19. E-Abd El-Wahab, Vacuum, 57(2000) 339.
20. J.Pankove, J. I, Optical process in semiconducting thin films, Thin Solid Films, 90 (1982)172.

21. J. Tauk, R. Grigorovici, A. Vancu, Phy. Sta. Solidi. 15 (1966) 627.
22. A.A. Al-Ghamdi, Vacuum, 80(2006) 400-405.
A. Ashour, N. El-Kdry, S.A. Mahmoud, Thin Solid Films, 269 (1995) 117.
23. P. Petkov, M. Wuttig, P. Ilchev, T. Petkova, J. Opt. Adv. Materials, 5 (2003) 1101.
24. M. Devika, N.K. Reddy, K. Ramesh, H.R. Sumana, K.R.Gunasekhar, E.S.R. Gopal, K.T. Ramakrishna Reddy, Semicond. Sci.Technol, 21, (2006) 1495.
25. N.Mott, E.A.Davis, Electronic Processes in Non-crystalline Materials, Clarendon Press, (1970).
26. K.Shimakawa, A. Kondo, K. Hayashi, S. Akahori, T. Kato, S. R. Elliot, Photoinduced metastable defects in amorphous semiconductors: commonality between hydrogenated amorphous silicon and chalcogenides, J.Non-Cryst. Solids, 387 (1993) 164-166.
27. A.A.Mulama1, J. M. Mwabora, A. O. Oduor, C.C. Muiva, Optical Properties, and Raman Studies of Amorphous Se- Bi Thin Films, The African Review of Physics. 9 (2014) 33.
28. V.Pandey, S.K.Tripathi, A.Kumar, J.Optoelectronics and Advanced Materials 8(2006) 789-793.
29. R.A.Taylor, J.F.Ryan, Time-resolved exciton photoluminescence in GaSe and GaTe., J. Phys. C, 20(1987) 6175.
30. H.S.Guder, B. Abay, H. Efeoglu, Y.K. Yogurtu, J.Lumin, 93 (2001) 243.
31. A.V.Kolobov, J.Tominaga, Properties of Amorphous Chalcogenides.DOI: 10.1007/978-3-642-28705-3_2, Chalcogenides, Springer Series in Materials Science, (2012) 164.

Chapter: 15
Analysis of Thermoelastic Properties of Materials in the Limit of Infinite Pressure

A. Dwivedi
Department of Physics, Institute of Basic Sciences, Khandari Campus,
Agra – 282 002, India
E-mail: adwd40@gmail.com

Abstract: Expressions for the higher order pressure derivatives of bulk modulus have been obtained in the limit of infinite pressure using the basic principles of calculus. The infinite pressure extrapolation based on the Stacey model has been used for determining equation of state parameters and thermoelastic properties at extreme compression. The results have been obtained using the Stacey reciprocal K-primed equation and compared with those determined from the Birch-Murnaghan equation, Poirier-Tarantola equation, generalized Vinet-Rydberg equation, and the Keane K-primed equation. The third-order Grüneisen parameter at infinite pressure has been found to play an important role in formulating the higher order pressure derivatives of bulk modulus. It should be emphasized that the generalized expressions formulated in the present study have the status of identities valid for all physically acceptable equations of state. A new thermodynamic constraint has been investigated for testing equations of state.

Keywords: Pressure derivatives of bulk modulus, Infinite pressure behaviour, Equations of state, Third-order Grüneisen parameter, Thermodynamic constraints.

1. Introduction

Study of bulk modulus and its pressure derivatives provides useful insight for investigating equations of state (EOS) and thermoelastic properties of materials [1-5]. The infinite pressure extrapolation method developed by Stacey [2, 3] can be used to determine the EOS parameters which are valid for the entire range of compressions from $V/V_0 = 1$ at atmospheric pressure down to the volume tending to zero in the limit of infinite pressure With

the help of an EOS, we calculate pressure as a function of volume, and bulk modulus at different pressures for a given material [6-10].

It has been found [2, 3] that pressure derivatives of bulk modulus depend sensitively on the potential energy functions and their derivatives with respect to interatomic separation. It is thus possible to make a test of the suitability for different potential energy functions with the help of pressure derivatives of bulk modulus. At high pressures, interatomic distance decreases and the magnitude of potential energy increases [11]. The potential energy derivatives evaluated from the pressure derivatives of bulk modulus have enhanced our knowledge regarding the anharmonic behaviour of materials [12].

The Grüneisen parameter γ and its volume derivatives provide important link between thermal and elastic properties of materials [1-3]. We have formulated expressions for higher order Grüneisen parameters in terms of pressure derivatives of bulk modulus using the method based on the principles of calculus [13-16]. In the present study, we obtain some new relationship for the pressure derivatives of bulk modulus in the limit of infinite pressure.

2. Method of Analysis

The second order Grüneisen parameter q is defined as [1, 2]

$$q = \left(\frac{d \ln \gamma}{d \ln V} \right)_T \tag{1}$$

and the third order Grüneisen parameter [2]

$$\lambda = \left(\frac{d \ln q}{d \ln V} \right)_T \tag{2}$$

In the limit of infinite pressure or the extreme compression (volume $V \rightarrow 0$) we have the relationship [2, 3]

$$\gamma_\infty = \frac{1}{2}K'_\infty - \frac{1}{6} \tag{3}$$

where the symbol ∞ represents the values in the limit of infinite pressure. It has been found [2, 3] that Eq. (3) has the status of an identify. K'_∞ is the value of first pressure derivative of bulk modulus, $K' = dK/dP,$ in the limit of infinite pressure. All physically acceptable EOSs reveal that pressure P and bulk modulus K both increase regularly with the increase in compression, and become infinitely large at extreme compression. On the other hand, K' decreases with the increase in compression, and it attains a minimum positive value equal to K'_∞ such that [17]

$$\left(\frac{P}{K}\right)_\infty = \frac{1}{K'_\infty} \tag{4}$$

Although P and K both are infinite in the limit of infinite pressure, but their ratio is positive finite given by Eq. (4). Using the definition $K = -V(dP/dV)$ in Eq. (4) we get

$$\left(\frac{d\ln P}{d\ln V}\right)_\infty = -K'_\infty \tag{5}$$

Eq. (5) implies that P changes asymptotically as $V^{-K'_\infty}$, and K as $K'_\infty V^{-K'_\infty}$ satisfying Eq. (4) in the limit of infinite pressure.

According to the principles of calculus, if y is a function of x such that (dlny/dlnx) is found to be a finite constant value in the limit of $x \to 0$,

$$\left(\frac{d\ln y}{d\ln x}\right)_{x\to 0} = 0 \tag{6}$$

$$\left(\frac{d\ln y}{d\ln x}\right)_{x\to 0} = \text{positive finite} \tag{7}$$

$$\left(\frac{d\ln y}{d\ln x}\right)_{x\to 0} = \text{negative finite} \qquad (8)$$

then Eqns. (6), (7) and (8) are satisfied for example by a function $y = cx^n$ when y remains positive finite in Eq. (6), becomes zero in Eq. (7), and tends to infinity in Eq. (8) in the limit x tends to zero,

Since γ_∞ remains positive finite, we find from Eqs. (1) and (6)

$$q_\infty = \left(\frac{d\ln\gamma}{d\ln V}\right)_{\substack{V\to 0\\ P\to\infty}} = 0 \qquad (9)$$

Thus the second-order Grüneisen parameter q tends to zero $(q_\infty \to 0)$ in the limit of infinite pressure. For the third-order Grüneisen parameter λ, we use Eqs. (2) and (7) to find

$$\lambda_\infty = \left(\frac{d\ln q}{d\ln V}\right)_{\substack{V\to 0\\ P\to\infty}} = \text{positive finite} \qquad (10)$$

Thus λ_∞ remains positive finite. An expression for λ_∞, the third-order Grüneisen parameter in the limit of infinite pressure, has been obtained [13, 14] by taking

$$\left(\frac{q}{KK''}\right)_\infty = \text{finite constant} \qquad (11)$$

where $K'' = d^2K/dP^2$ is the second pressure derivative of bulk modulus. K'' is multiplied by K so that KK'' is dimensionless. Since K' decreases with the increase in pressure at finite pressures [2, 3], KK'' is negative, but in the limit of infinite pressure K' becomes constant (K'_∞), and therefore

$$(KK'')_\infty = 0 \qquad (12)$$

Thus q_∞ and (KK'') both tend to zero but their ratio is finite constant (Eq. 11). The volume derivative of Eq. (11) gives

$$\left(\frac{d\ln q}{d\ln V}\right)_{\substack{V\to 0\\ P\to\infty}} = \left(\frac{d\ln KK''}{d\ln V}\right)_{\substack{V\to 0\\ P\to\infty}} \tag{13}$$

which can be written as follows

$$\lambda_\infty = -K'_\infty - \left(\frac{K^2K'''}{KK''}\right)_\infty \tag{14}$$

where $K''' = d^3K/dP^3$. We multiply K''' by K^2 to write K^2K''' in a dimensionless form. Eq. (14) was formulated by Shankar et al. [13, 14]. There exists another principle of calculus. If the ratio of two functions of a common variable (such as volume or pressure) becomes indeterminate (zero divided by zero or infinity divided by infinity) at a particular value of the variable, then this ratio of two functions becomes equal to the ratio of the differential derivatives of these two functions at that point. It has been found that KK'' and K^2K''' both are zero but their ratio is finite in the limit of infinite pressure. Using the abovementioned principle of calculus we can write

$$\left(\frac{K^2K'''}{KK''}\right)_\infty = \left(\frac{2KK'K''' + K^2K^{IV}}{K'K'' + KK'''}\right) \tag{15}$$

which gives

$$\left(\frac{K^3K^{IV}}{K^2K'''}\right)_\infty = -K'_\infty + \left(\frac{K^2K'''}{KK''}\right)_\infty \tag{16}$$

Using Eq. (14) in Eq. (16) we get

$$\left(\frac{K^3K^{IV}}{K^2K'''}\right)_\infty = -2K'_\infty - \lambda_\infty \tag{17}$$

In a similar manner, we have derived

$$\left(\frac{K^4K^{V}}{K^3K^{IV}}\right)_\infty = -3K'_\infty - \lambda_\infty \tag{18}$$

In Eqs. (15) to (18), $K^{IV} = d^4K/dP^4$ and $K^{V} = d^5K/dP^5$. They are respectively multiplied by K^4 and K^5 to express them in dimensionless terms.

3. Results and Discussions

We can thus evaluate the higher pressure derivatives of bulk modulus at extreme compression with the help of Eqs. (14) to (18). With the help of these equations we can write

$$\left(\frac{K^4K^{V}}{K^3K^{IV}}\right)_\infty + \left(\frac{K^2K'''}{KK''}\right)_\infty = 2\left(\frac{K^3K^{IV}}{K^2K'''}\right)_\infty \tag{19}$$

Thus the terms representing ratios of higher pressure derivatives in Eq. (19) are in arithmetic progression. Eq. (19) can be generalize to yield

$$\left(\frac{K^n d^{n+1}K/dP^{n+1}}{K^{n-1}d^nK/dP^n}\right)_\infty + \left(\frac{K^{n-2}d^{n-1}K/dP^{n-1}}{K^{n-3}d^{n-2}K/dP^{n-2}}\right)_\infty = 2\left(\frac{K^{n-1}d^nK/dP^n}{K^{n-2}d^{n-1}K/dP^{n-1}}\right)_\infty \tag{20}$$

where n is a positive integer greater than 3. Equations (14) to (20) are found here to be satisfied by the Stacey reciprocal K- primed EOS [18].

$$\frac{1}{K'} = \frac{1}{K'_0} + \left(1 - \frac{K'_\infty}{K'_0}\right)\frac{P}{K} \tag{21}$$

and also satisfied by the Shanker reciprocal gamma relationship [5]

$$\frac{1}{\gamma}=\frac{1}{\gamma_0}+K'_\infty\left(\frac{1}{\gamma_\infty}-\frac{1}{\gamma_0}\right)\frac{P}{K} \tag{22}$$

where $K'_0, K'_\infty, \gamma_0$ and γ_∞ are the values of bulk modulus and Grüneisen parameter at zero pressure and infinite pressure respectively. It has been found that $K'_\infty / K'_0 = 3/5$ [19-22]. Values of λ_∞ and ratios of higher pressure derivatives of bulk modulus determined from different equations of state are reported in Table 1. Stacey and Hodgkinson [23] showed that λ_∞ must be positive with the constraint

$$0 < \lambda_\infty < K'_\infty - 2f_\infty \tag{23}$$

where f_∞ is the infinite pressure limit of the free volume parameter in the theory of Grüneisen parameter value of f_∞ is nearly equal to 1.50 [23]. Shanker et al [13] derived the equation

$$\lambda_\infty = \left[KK''/\left(1-K'P/K\right)\right]_\infty / K'_\infty + K'_\infty \tag{24}$$

The first derivative of $1/K'$ with P/K can be obtained as follows –

$$\frac{d\left(1/K'\right)}{d\left(P/K\right)} = -\frac{KK''}{K'^2\left(1-K'P/K\right)} \tag{25}$$

Equations (24) and (25) taken together yield

$$\left[\frac{d\left(1/K'\right)}{d\left(P/K\right)}\right]_\infty = 1-\frac{\lambda_\infty}{K'_\infty} \tag{26}$$

Taking the derivative of $\left(1/K'\right)$ with respect to P/K from the Stacey EOS, Eq. (21), we get

$$\left[\frac{d(1/K')}{d(P/K)}\right] = 1 - \frac{K'_\infty}{K'_0} \tag{27}$$

Equations (26) and (27) yield

$$\lambda_\infty = \frac{K'^2_\infty}{K'_0} \tag{28}$$

Since K'_∞ is less than K'_0, Eq. (28) reveals that λ_∞ is less than K'_∞. For the lower mantle $(K'_0 = 4.2, K'_\infty = 2.4)$ and the Earth core $(K'_0 = 5.0, K'_\infty = 3.0)$ as reported by Stacey and Davis [2], we calculate $\lambda_\infty = 1.37$ and 1.80 from Eq. (28). Thus the Stacey reciprocal K-primed EOS, Eq. (21) satisfies the constraint given by Eq. (23). On the other hand, the Poirier-Tarantola EOS and the Keane K-primed EOS (Table - 1) do not satisfy Eq. (23).

4. Conclusions

Eqs. (14) to (20) represent the thermodynamic constraints which must be satisfied in the limit of infinite pressure for all physically acceptable equations of state and thermodynamic formulations. K'_∞, γ_∞ and λ_∞ must remain positive finite whereas q_∞ must tend to zero. Higher pressure derivatives of bulk modulus such as $KK'', K^2K''', K^3K^{IV}, K^4K^V$ are found individually to be zero. However, the ratios of any two of them remain finite. K'_∞ and λ_∞ are two important parameters which play the central role in determining higher pressure derivatives of bulk modulus at infinite pressure. We have also discussed the fundamental constraint according to which λ_∞ must be less than K'_∞. This constraint is useful for a critical test of an EOS.

References

1. O.L., Anderson, Equation of State for Geophysics and Ceramic Sciences, Oxford University, Press, New York, 1995.
2. F.D. Stacey, P.M. Davis, Phys. Earth Planet, Inter. **142**, 137 (2004).
3. F.D. Stacey, Rep. Prog. Phys. **68**, 341 (2005).
4. A. Dwivedi, Canadian J. Phys. **94**, 748 (2016).
5. J. Shanker, K. Sunil, B.S. Sharma, Phys. Earth Planet Inter. **262**, 41 (2017).
6. F. Birch, J. Geophys. Res. **91**, 4949 (1986).
7. J.P. Poirier, A. Tarantola, Phys. Earth Planet, Inter. 109, 1 (1998)
8. J. Shanker, B.P. Singh, K. Jitendra, Condensed Matter. Physics **12**, 205 (2009).
9. A. Keane, Aust. J. Phys. **7**, 323 (1954).
10. K. Sushil, K. Arunesh, P.K. Singh, B.S. Sharma, Physica B, **352,** 134 (2004).
11. F.D. Stacey, B.J. Brennan, R.D. Irvine, Geophys. Survey **2,** 189 (1981).
12. F.D. Stacey, D.G. Isaak, J. Geophys. Res. **108**, 2440 (2003).
13. J. Shanker, P. Dulari, P.K. Singh, Physica B **404**, 4093 (2009).
14. J. Shanker, K. Sunil, B.S. Sharma, Physica B **407**, 2082 (2012).
15. J. Shanker, P.K. Singh, M.P. Singh Indian J. Pure Appl. Phys. **52**, 33 (2014).
16. J. Shanker, P.K. Singh and S. Saurabh, Indian J. Pure Appl. Phys. **53**, 230 (2015).
17. L. Knopoff, J. Geo Phys. Res. **68**, 2929 (1963).
18. F.D. Stacey, Geophys. J. Int. **143**, 621 (2000).
19. S.S. Kushwah, H.C. Shrivastava, K.S. Singh, Physica B **388**, 20 (2007).
20. S.K. Srivastava, S.K. Sharma, P. Sinha, J. Phys. Chem. Solids **70**, 255 (2009).
21. S.S. Kushwah, N.K. Bhardwaj, J. Phys. Chem. Solids, **70**, 700 (2009).
22. H.C. Shrivastava, Physica B **404**, 251 (2009).
23. F.D. Stacey, J.H. Hodgkinson, Phys. Earth Planet. Inter. **286,** 42 (2019)

Table: 1 – Values of the ratios of higher pressure derivatives of bulk modulus at infinite pressure.

Equation of State	λ_∞ (Eq. 14)	$\left(\frac{K^2K'''}{KK''}\right)_\infty$	$\left(\frac{K^3K^{IV}}{K^2K'''}\right)$	$\left(\frac{K^4K^{V}}{K^3K^{IV}}\right)$
Birch-Murnagham [6]	2/3	$-\left(K'_\infty+\frac{2}{3}\right)$	$-\left(2K'_\infty+\frac{2}{3}\right)$	$-\left(3K'_\infty+\frac{2}{3}\right)$
Poirier-Tarantola [7]	0	$-K'_\infty$	$-2K'_\infty$	$-3K'_\infty$
Generalized Rydberg [3]	1/3	$-\left(K'_\infty+\frac{1}{3}\right)$	$-\left(2K'_\infty+\frac{1}{3}\right)$	$-\left(3K'_\infty+\frac{1}{3}\right)$
Keane K-primed [9]	K'_∞	$-2K'_\infty$	$-3K'_\infty$	$-4K'_\infty$
Stacey reciprocal K-primed [18]	$\frac{3}{5}K'_\infty$	$-\frac{8}{5}K'_\infty$	$-\frac{13}{5}K'_\infty$	$-\frac{18}{5}K'_\infty$

Chapter-16

Quantum chemical calculation s of [(1S, 4R)-4-{2-amino-6-(cyclopropylamino) purin-9-yl} cyclopent-2-en-1-yl] methanol (Abacavir) using Density Functional Theory

[1]Shashi Kumar Gangwar, [2]Susheel Kumar Singh, [3]R. K Shukla and [4]Bhuvan Bhasker Srivastava

[1]Department of Physics, M. J. P. R. U. Bareilly, UP India
[2]Department of Physics, HLYB PG College, Lucknow, UP India
[3]Department of Physics, University of Lucknow, Lucknow, UP India
[4]Department of Physics, Shia PG College, Lucknow, UP India
Email-susheelsingh489@gmail.com

Preface

A large number of structural nucleoside analogous (NA) have been designed and synthesized [1, 2] for anticancer activity [3-5] and viral infections. Abacavir is a strong class nucleoside analog reverse transcriptase inhibiter (NRTI) and has been used for the treatment of the cancer (the formation of DNA from an RNA Template) [6-8]. It has been seen that 5-substituted -2'-deoxyuridines reduces cancer cell proliferation by inhibiting thymidylate synthase, an enzyme essential in the synthesis of DNA [9, 10]. The Potent anticancer agents have been recently synthesized in which the cyclopentene ring is replaced by an indane system [10] and assayed on different cancer cell lines. The title compound shows more resistance to hydrolases than the natural nucleosides. The charge transfer involved in the formation of adducts is also qualitatively studied [11]. However, nucleoside anticancer drug commonly associated with various adverse effects are associated with the molecular structure [12]. The anticancer drug and DNA binding mechanism involves the donation of electrons from DNA and acceptance of the electrons by the drug molecule.

Computational Methodology

All the quantum chemical calculations are carried out with the help of Gaussian 09 software package [23] for the prediction of the molecular structure, energies of the optimized structure, ^{1}H NMR chemical shifts, NBO analysis, vibrational wavenumbers, UV analysis, reactivity descriptors and first hyper-polarizability using B3LYP functional 6-311++G(d, p) basis set [24] which invokes Becke's three parameter (local, nonlocal, Hartree-Fock) hybrid exchange functional (B3) with Lee-Yang-Parr correlation functional (LYP). The basis set 6-311++G(d, p)

with ‘d’ polarization functions on heavy atoms and ‘p’ polarization functions on hydrogen atoms are used for better description of polar bonds of molecule [13,14]. It should be emphasized that ‘p’ polarization functions on hydrogen atoms. Time dependent density functional theory (TD-DFT) is used to find the various electron excitations and their nature within the molecule. The optimized geometrical parameters are used in the vibrational wave numbers calculation to characterize all stationary points as minima and their harmonic vibrational wave numbers are positive. Gauss View program is used for visualization of optimized geometry of the molecule. Potential energy distribution along internal co-ordinate is calculated by Gar2ped software [15]. The comparative experimental and calculated (IR and UV-Visible) spectra of the title molecule shown in **Figure 3.1** have been plotted. DFT calculations have been also used to calculate the dipole moment, mean polarizability $< \alpha_0 >$ and first static hyperpolarizability β_0 based on the finite field approach.

Molecular Structure and Optimized Geometry

The optimized geometry for ground state lower energy conformer is shown in **Figure 3.1**. Selected optimized parameters of the title compound calculated at B3LYP/6-311++ G (d, p) [16] are listed in the **Table-3.1**. The molecule possess C_1 symmetry and total energy for the ground state lower energy conformer is calculated as -948.29 a.u. and the dipole moment about the symmetry is 5.003 debye. The common features of molecule include one pyrimidine ring (R_1), one cyclopentene ring (R_2) and one cyclopropane ring (R_3) attached through –N-H group and one cyclopentene (five membered) ring is attached with the purine structure of the molecule in 3d geometry in which R1 ring is attached with NH_2 group and OH group is attached with cyclopentene through CH_2. The bond length, bond angle and dihedral angles are calculated for the equilibrium state of the abacavir. Almost all the calculated bond length and bond angles show a reasonable agreement with the experimental values. Based on the optimized geometry parameters, although there are some differences between the theoretical and experimental values, the optimized structure parameters can well reproduce the experimental ones and they are the basis for there after discussion.

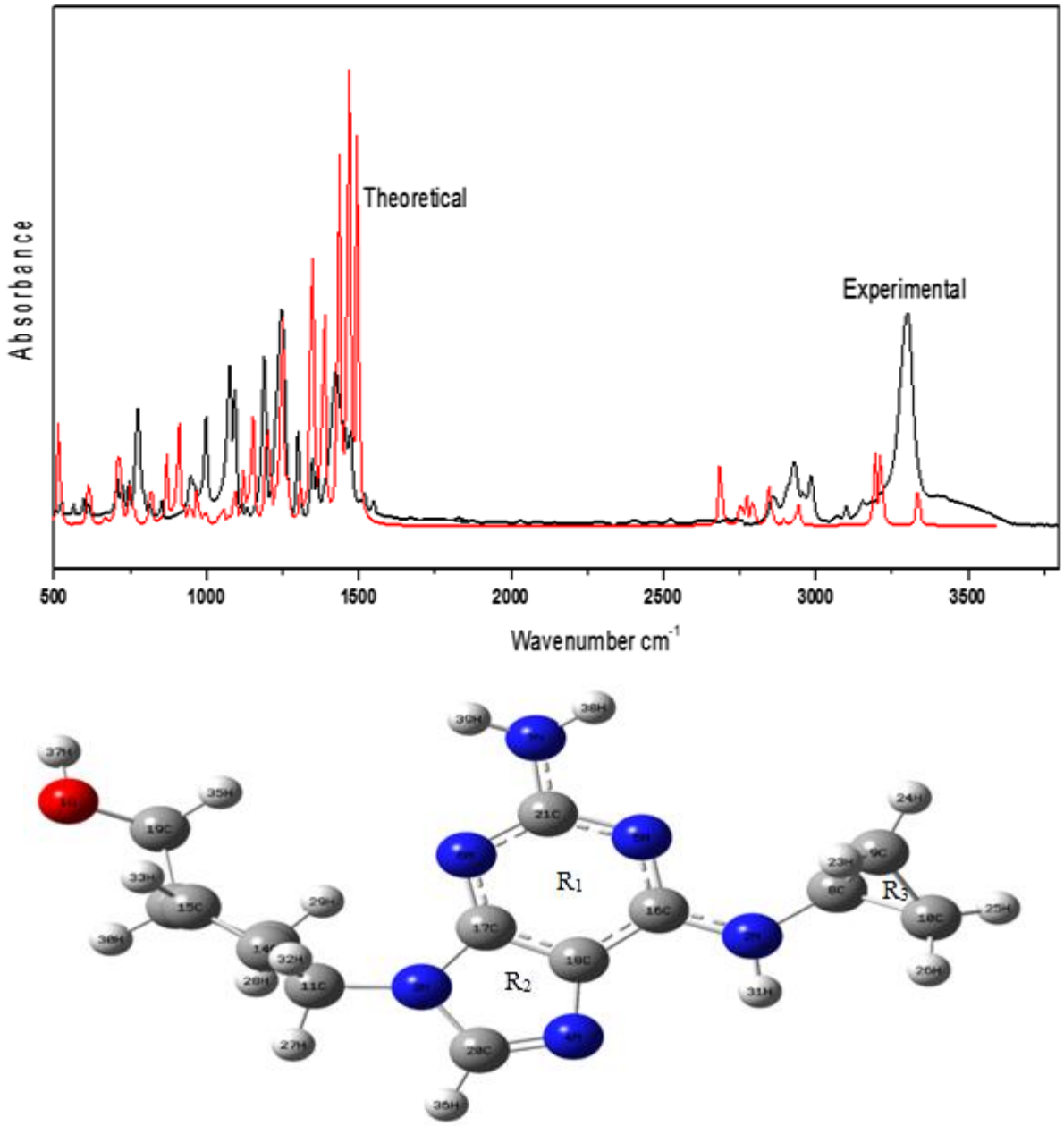

Figure 3.1: Optimized Geometry for the Lowest Energy Conformer of Abacavir

Vibrational analysis and FTIR Spectrum

The selected theoretical and experimental vibrational modes of title molecule**,** calculated at B3LYP/6–311++G (d, p) method and their assignments using PED are given in **Table 3.2**. Comparison between theoretical and experimental IR spectra in the region 4000–400 cm^{-1} and is shown in **Figure 3.2**. In many chemical systems, the theoretically calculated frequencies and experimentally observed frequencies match experimentally well. Hence, it may be expected that

the vibrational analysis from the theoretical predicted force field mimics well the modes of vibrations in a real molecule. In the calculation of vibrational frequencies there are some limitations like effect of electron correlation, basis set deficiencies as well as inter and intra molecular interactions. First principle calculations follow the approximation that the chemical bonds are elastic but in case of higher frequencies there is an aberration presumably due to anharmonicity. Therefore, calculated wavenumbers are scaled down using scaling factor 0.9608 to discard the anharmonicity present in real system. The Vibrational band assignments have been made on the basis of normal co-ordinate analysis. Internal coordinates have been chosen according to Pulay's recommendations. Gauss-View program is used to assign the calculated harmonic vibrational wavenumbers.

N-H Vibrations

In the FT-IR spectrum of abacavir, the N-H stretching of ν_{NH2} is observed at 3467 cm^{-1}, whereas this is calculated at 3562 cm^{-1}. The weak band of NH_2 scissoring is assigned in the range 1625-1597 cm^{-1}, which matches well with the observed mode between 1630-1590 cm^{-1} in FT-IR spectrum. The observed NH wagging mode at 550 cm^{-1} agrees well with the calculated wavenumber at 535 cm^{-1}. The observed NH_2 wagging mode at 812 cm^{-1} agrees well with the calculated wavenumbers at 803 cm^{-1}.

C-H and O–H Vibrations

All organic compounds possess a group of bands between 3100 and 2750 cm^{-1} which are observed both in Raman and infrared spectra. The stretching modes of C-H in cyclopropane ring are observed in the region 3104 -2869 cm^{-1} and one -OH group is attached with tetra cyclopropane ring having observed frequency to be 3345cm^{-1}.

C-C Vibrations

In aromatic hydrocarbon, skeletal vibrations involving carbon–carbon stretching within ring are absorbed in the region 1225-1630 cm^{-1}. The wavenumbers calculated at 1232-1625 cm^{-1} assigned to the C=C stretches in pyrimidine ring which corroborate well with experimental at 1530-1532 cm^{-1}. Rocking of C–C bond is calculated at 1546 cm^{-1} and observed in the experimental spectrum with weak intensity.

C-O Vibrations

The experimental FT-IR spectrum gives C-O mode at 962 cm^{-1}. The C–O stretching vibrations of alcoholic group actually consist of two asymmetrical coupled vibrations as O−H=O−H,

O−C−H−H and these bands occur in the region 1536–1113 cm^{-1}. The calculated wavenumber at 1010 cm^{-1} with 16% contribution in PED demonstrates the O–C–C stretching vibration ($\nu_{O1–C19}$) and corresponds to the observed wavenumber at 962 cm^{-1} experimentally.

Fukui Function

Fukui function (f_k^+, f_k^-), Local softness (s_k^+, s_k^-) and Local electrophilicity Indices (ω_k^+, ω_k^-) for selected atomic sites of title molecule are listed in **Table 3.5** using Hirschfeld [16] population analyses. The high values of all the three local electrophilic reactivity descriptors at C20 indicate that this site is more prone to nucleophilic attack. The calculated local reactivity descriptors of synthesized molecule favour the formation of new conformers of the molecule and synthesis of heterocyclic compounds.

Table 3.5 *Selected reactivity descriptors as Fukui functions (f_k^+, f_k^-), local softnesses (s_k^+, s_k), local electrophilicity indices (ω_k^+, ω_k^-) for compound, using Hirshfild atomic charges.*

Sites	f_k^+	s_k^+	ω_k^+	Sites	f_k^-	s_k^-	ω_k^-
C8	0.0215	0.29252	0.029866	O1	0.0205	0.278919	0.028477
C9	0.0345	0.46940	0.047924	N2	0.0957	1.302075	0.132937
C10	0.0465	0.63267	0.064593	N3	0.0249	0.338784	0.034589
C16	0.0815	1.108873	0.113212	N4	0.0529	0.719747	0.073483
C17	0.0184	0.250347	0.025559	N5	0.0280	0.380962	0.038895
C20	0.1399	1.903451	0.194335	N6	0.0929	1.263979	0.129047
C21	0.0433	0.589131	0.060148	N7	0.1511	2.055836	0.209893

QTAIM Analysis

The Quantum theory of atoms in molecule (QTAIM) defines the chemical bonding and structure of the chemical system based on the topology of the electron density. In addition to bonding, QTAIM allows the calculation of certain physical properties on a per atom basis, by dividing space up into atomic volumes containing exactly one nucleus which acts as a local attractor of the electron density (ED). Molecular graph of using AIM program [17.18] at B3LYP/6-311++G (d, p) level. Topological as well as geometrical parameters for bonds of interacting atoms are given in **Table 3.6**. For the interaction N6….H29, ED and its Laplacian ($\nabla^2\rho_{bcp}$) follow the Koch and popelier criteria and distance between interacting atoms ($D_{N6.....H29}$ = 2.45) is less than the sum of vander Waals radii of these atoms ($r_{N} + r_{H}$ =2.643 A°). Therefore, intramolecular interaction N6-H29 is a hydrogen bond. The various inter-molecular, intra-molecular interactions and H–bonding are characterized with the use of the quantum theory of atoms in molecules (QTAIM) [19]. H-bonded interactions may be classified as follows:

(i) Strong H–bonds are characterized by $\nabla^2\rho_{(BCP)} < 0$ and $H_{BCP} < 0$ and their covalent character is established

(ii) Medium H–bonds are characterized by $\nabla^2\rho_{(BCP)} > 0$ and $H_{BCP} < 0$ and their partially covalent character is established

(iii) Weak H–bonds are characterized by $\nabla^2\rho_{(BCP)} > 0$ and $H_{BCP} > 0$ and they are mainly electrostatic.

Other weak interactions (X···Y) are characterized by $\nabla^2\rho_{(BCP)} > 0$ and $H_{BCP} > 0$.The nature of N6-H29 Hydrogen bond is week due to $\nabla^2\rho_{(BCP)} > 0$ and $H_{BCP} > 0$. Espinosa proposed a proportionality between hydrogen bond energy (E_{HB}) and potential energy density (V_{BCP}) at N.....H contact, $E_{HB} = ½(V_{BCP})$ [20]. According to this equation the energy of N6-H29 hydrogen bond is calculated as -2.38kcal/mol.

References

[1] Cheason B. D., Keating M. I., Plunkett W., "Nucleoside analogous in cancer therapy", Dekker, New York **12**, (1997) 227-264.

[2] Sarmah P., Deka R. C., "Anticancer activity of nucleoside analogues" *J Mol. Model* **16**, (2010) 411-418.

[3] Branciforte D, Martin S.L., Developmental and cell type specificity of LINE-1 expression in mouse testis, implications for transposition. *Mol Cell Biol.* **14**, (1994) 2584–2592.

[4] Kurth R., Bannert N., Beneficial and detrimental effects of human endogenous retroviruses. Int J Cancer **126**, (2010) 306–314.

[5] Carr A., Workman C., Smith D. E., Hoy J., Hudson J., (2002).

[6] Fermandez F., Garcia-M., Morales X., Morales M., Rodriguez- Borges J. E., Synthesis **2**, (2001) 239-242.Abad F., Alvarez. F., Alvarege F. Garcia-Mera X., Rodriguez-Borges J.E., Nucleosides. Nucleic Acids **20**, (2001) 1127-1128.

[7] Abad F., Alvarez. F., Alvarege F., Fermandez, X.Garcia-Mera, Rodriguez-Borges J.E., Nucleosides. Nucleic Acids **20**, (2001) 1127-1128.

[8] Yao S.W., Lopes V.H.C., Fermandez F., Garcia-Mera X., Morales M., Rodrguez- Borges J.E., Cordeiroa M.N.D.S., *Bioorg. Med. Chem.* **11,** (2003) 4999-5006.

[9] Marlon C., Lee C. H., Gfesser G. A., Erol K., Bayburt S., Shripad A.O., Stewart, Yu Haixia, "*Bioorganic & Medicinal Chemistry Letter"* **11,** (2001) 83-86.

[10] Contreras-Galindo R, Kaplan M. H, Leissner P., Verjat T., Ferlenghi I., Bagnoli F., Giusti F., Dosik M. H., Hayes D. F., Gitlin S. D., Markovitz D. M., Human endogenous etrovirus K (HML-2) elements in the plasma of people with lymphoma and breast cancer. **82**, (2008) 9329–9336.

[11] Srivastava H.K., Pasha F.A., Singh P.P., *Int. J. Quantum Chem.* **103**, **(2005)** 237- 245.

[12] Helguera A.M., Rodriguez-Borges J.E, Garcia-Mera X., Fermandez F., M.N.D.S Cardeiroa *J Med Chem* **50,** (2007) 1537-1545.

[13] Chattaraj P.K., Giri S., *J. Phys. Chem.* A **111**, (2007) 11116

[14] Frisch M. J., et al., Gaussian 03, Revision C.02, Gaussian, Inc., Wallingford, CT (2004).

[15] Parr R.G., Yang W., Density Functional Theory of Atoms and Molecules, Oxford University Press, New York, (1989).

[16] Becke A.D., *J. Chem. Phys.* **98**, (1993) 5648–5652. K. Fukui, T. Yonezawa, H. shingu, *J. Chem. Phys.* 20 (1952) 722–725.

[17] Koch U., Popelier P., *J. Phys. Chem.* A **99**, (1995) 9747.

[18] Bader R. F. W., Cheeseman J. R., In AIMPAC (2000).

[19] Runge E., Gross E. K. U., *Phys. Rev. Lett.* **52**, (1984) 997-1000**.**

[20] Unver H., Karakus A., Elmali A., *J. Mol. Struct.* **702**, (2004) 49–54.

Chapter: 17

Dye sensitized solar cells-need of an hour

Priyanka Chawla, Kumari Pooja and Mridula Tripathi*

***Department of Chemistry, CMP Degree College,**
University of Allahabad, Allahabad India-211002
***E-mail: mtcmpau@gmail.com**

Introduction

Among all the available renewable energy sources like wind, water, tide, biomass, solar energy is considered to be most promising as it provides clean and abundant energy. To convert solar energy into electrical energy solar cells devices are being used. Nowadays scientists all over the world are focusing their attention in developing such solar cells which are low in cost and provide economically sustainable energy source. With the increase in world population at high rate has increased the present energy consumption to a much high level. The traditional energy sources such as coal, oil and natural gas are not able to full fill the present energy demand as well as release of green house gases as a result of this combustion have created an adverse environmental effect. Hence, the need of renewable and environment friendly energy sources is unquestionable. The various renewable energy sources are solar energy, wind energy, geothermal energy and hydropower; various energy policies are being implemented in many countries to accelerate renewable energy use [1-2]. Energy from renewable sources i.e. wind, solar, geothermal, hydropower accounts for 13% of global energy consumption. The largest share comes from the burning of traditional biomass. India is also focusing on renewable energy sources. The government set ambitious target to generate 160 Gigawatt's (GW) of wind and solar energy by 2022, a 400% increase from previous target. Also in certain European countries like Germany, such policies have induced a "Green Economy" boom especially in the wind and solar electricity (photovoltaic sectors) [3-4].

Among all photovoltaic is the fastest growing power generation technology and it is growing power with an annual rate of about 40% for the past few decades. The reason for

such a growth is enormous energy source for conversion into electricity. It is estimated that the energy of sunlight reaching the surface of the earth in an hour is more than that the total energy used by global population in a year. Therefore if we can harness the available solar energy in an economic way than undoubtedly we can easily ease the energy problems that we are facing. There are several types of solar cells known today which are being employed for converting solar energy into electricity. First generation solar cells or silicon based solar cells have dominated the photovoltaic market for many years but the cost employed in their fabrication limits its use widely so researchers are looking for some other alternative solar cells which are cheap and eco friendly in this direction as successfully demonstrated by O'Regan and M. Gratzel in 1991,the dye sensitized solar cells (DSSCs) have attracted a lot of attention by both academia and researchers. DSSCs sensitized with dyes based on heavy metals such as ruthenium and zirconiums with nonporous TiO_2 have been recorded to show a conversion efficiency of about 11-12% using liquid electrolyte [5-6]. The main difference between DSSCs and p-n junction solar cells is about their components and working. In p-n junction solar cells the semiconductor performs both the tasks of light harvesting and charge carrier transport, while in DSSCs these two functions are performed separately. Moreover, the solar energy conversion mechanisms in DSSCs are the interfacial processes while in p-n junction cells these bulk processes. Hence most studies on DSSC are made to understand the prevailing role of electron transfer dynamics and kinetics at nanocrsytalline metal oxide/sensitizer/electrolyte interfaces. Though researchers are performing studies on this subject, but still not much understanding of the kinetics of the interfacial processes has been made. If we properly understand the kinetics of interfacial process we can improve the efficiency of DSSC and scale up their manufacturing.

Structure and Working of DSSCs

The dye sensitized solar cells (DSSCs) is a nanostructured photoelectrochemical devices. Light is absorbed by a dye attached to the large band gap semiconductor. Solar energy is converted into electricity by the photoinduced injection of an electron from the excited dye to the conduction band of the semiconductor oxide. The electron moves from the semiconductor oxide to current collector and the external circuit. In the pores there is a

redox mediator which ensures that the oxidized dye species are continuously regenerated over and over again and the cycle is not stopped as shown in figure.

The major charge transfer and transparent processes in a DSSC is shown in figure 1. As soon as the light absorption takes place by the dye molecules, the ultrafast electrons injection takes place into the conduction band of semiconductor photoelectrode. There are two important back reactions in DSSCs one is the recombination of conduction band electrons with the oxidized dye molecules, which occurs on a microsecond timescale. It is also important to note that the reduction of the oxidized dye (S^+) by I^- is also very fast, occurring on a nanosecond timescale, which also compete efficiently with the back reactions to ensure the collection of photoelectrons by back contact.

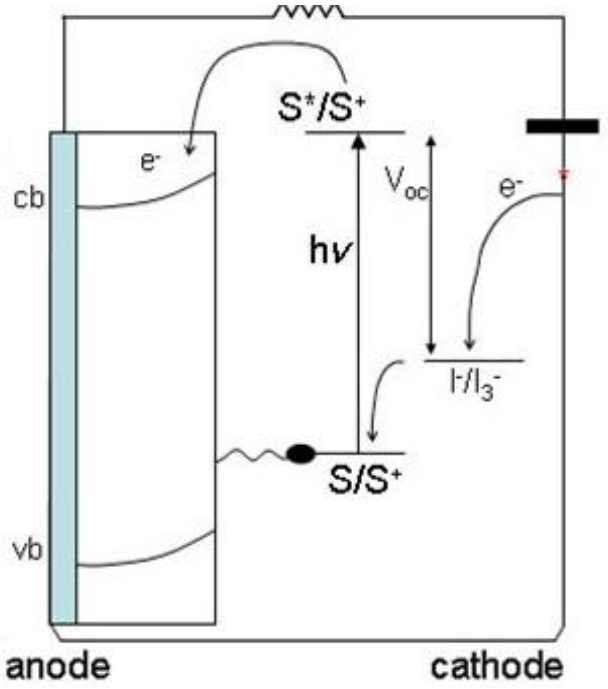

Figure 1: Energy diagram of DSSC

The second back reaction is the recombination of conduction band electrons with tri-iodide (I_3^-) in the electrolyte. This process also occurs on milliseconds to seconds' timescale. The iodide (I^-) is regenerated in turn at counter electrode by the reduction of I_3^- with electrons which have passed through the external circuit. Each of the above mention steps are shown below:

$S\|TiO_2 + h\nu \rightarrow S^*\|\ TiO_2$	Photoexcitation
$S^*\|\ TiO_2 \rightarrow S^+\|TiO_2 + ecb(TiO_2)$	Charge injection
$S^*\|\ TiO_2 \rightarrow S\|TiO_2$	Relaxation
$S^+\|TiO_2 + 2\ I^- \rightarrow S\|TiO_2 + I_2^{-\bullet}$	Regeneration
$S^+\|TiO_2 + e^-(TiO_2) \rightarrow S\|TiO_2$	Recombination
$e^-(TiO_2) + I_2 \rightarrow I_2^{-\bullet}$	Back reaction

The four major components of DSSCs are

1. Photoanode
2. Sensitizers or Dyes
3. Electrolytes
4. Counter electrode

Photoanode

It is the most important component of DSSCs, it is rather called the heart of the DSSCs. Semiconductors oxide are generally preferred for the photoanode of DSSCs because of their exceptional stability against photo-corrosion on optical excitation in the band gap. Moreover, their large band gap (~3eV) is needed for the transparency of the semiconductor electrode for the large part of the solar spectrum. Generally TiO_2 or ZnO is the mostly used semiconductor oxides for DSSCs, however other semiconductor are also used in porous nanocrystalline electrodes in dye sensitized solar cells includes SnO_2, Fe_2O_3, WO_3, Nb_2O_5, Ta_2O_5 etc. But still titanium dioxide is the first choice for dye sensitized nanostructured electrodes for DSSCs. As it have nearly the same band gap (~3.3 eV) which favour the ejection of electrons into their conduction bands [7-8].

For the preparation of colloidal metal oxide particles Sol-Gel route is adopted. As with this method nanoparticles of low range can be obtained such as TiO_2, ZnO, ZrO, Ta_2O_5, WO_3, NiO and many others [9-10].

Transparent Conductive Oxide (TCO)

TCO is an important material in the field of optoelectronic it is used in flat panel displays, LEDs and waveguide devices because of its special characteristics of high transparency and

low sheet resistance. It is a wide band gap n-type semiconductor that consists of high concentration of free electrons. The most common one are Indium doped tin oxide (ITO), fluorine doped tin oxide (FTO) and Aluminium doped Zinc Oxide (AZO). Due to its high transparency, good electrical conductivity and low material cost. ITO performs the best among all TCO substrates.

Sensitizers or Dyes

Dye as photosensitizers is the most important component Of DSSCs. The main work of dye is absorption of light and injection of the electrons into the conduction band of the semiconductor. A layer of sensitizers is attached over the surface of photoanodes by chemical bonding between the anchoring groups present on the sensitizers and hydroxyl group present on the metal oxide of photoanodes. There are mainly two categories of sensitizers: metal based dyes and metal free organic dyes. In order to reduce the cost and environment pollution natural dyes are being employed as photosensitizers in DSSCs. Natural pigments containing betalains, carotenoids, chlorophyll, and flavonoids which are found in various parts of plants such as fruits, flowers and leaves have been successfully used as photosensitizer in DSSCs [11-12]. Though the natural sensitizers are non-toxic, eco-friendly, easy to prepare but DSSCs prepared with natural sensitizers showed less efficiency due to low absorption range. Therefore researchers are using cocktail mixtures of these dyes in order to improve the absorption range of natural sensitizers [13-14].

Electrolytes

Generally iodide/triiodide (I^-/I_3^-) redox couple in an organic solvent is used as liquid electrolyte for DSSCs. But the reodxshuttels used in the electrolyte reacts with the platinum electrode and corrode the surface of electrode which effects the proper functioning of cell as well as the organic solvent used leaks and vaporizes with time. In order to overcome this major problem scientists are focusing their attention in the solidification of electrolyte such as inorganic or organic hole conductors, ionic liquids, polymer electrolyte [15-16]. Various polymers such as poly ethylene oxide (PEO), poly (vinylidene fluoride) (PVDF) etc are being employed as electrolyte in DSSCs. Further to improve the conductivity of these polymers electrolyte nanoparticles are being added in the polymer matrix, producing a

composite polymer electrolyte. The main function of these nanoparticles in the polymer matrix is to reduce the crystallinity of the polymer, as well to create the porous system which helps in easy diffusion of ions which results in increase in the ionic conductivity as well the photocurrent and efficiency of device. Various types of fillers based on carbon as well as inorganic nanomaterials such as TiO_2, SiO_2, and ZrO2 are being employed for composite polymer electrolytes [17-18].

Counter electrode

The photoexcited electrons from the dye diffuses through the TiO_2 network in the photoanode and go to the counter electrode which is usually formed by the thin catalytic layer of platinum on a conducting glass substrate. The platinum in the counter electrode helps in the regeneration of dyes by catalysing the I^- regeneration from the I_3^- species in the redox couple. The morphology of the Platinum, its surface roughness, nature of the exposed facet etc. plays a very important role in determining the overall efficiency of a DSSC device [19-20].

Application of DSSCs

Having the advantages of light weight, low cost and flexibility, DSSCs are being developed for consumer applications. For example DSSCs are being used in portable electronic devices, bags, buildings serving as charging stations. Samsung has manufactured DSSCs battery for charging mobile, with a cost between one third and one fifth of the existing silicon based photovoltaic products.

The performance of DSSCs is less sensitive to the illumination conditions compared to the inorganic solar cells. The working electrode in DSSCs can absorb incident light from different directions. Therefore they are able to provide electricity to low power electrical equipment's over under low illumination conditions. DSSCs can be used in building as windows, skylights, roof and walls to provide electric power for the buildings and save electric energy. Figure 1.5 shows various examples of commercialized DSSCs.

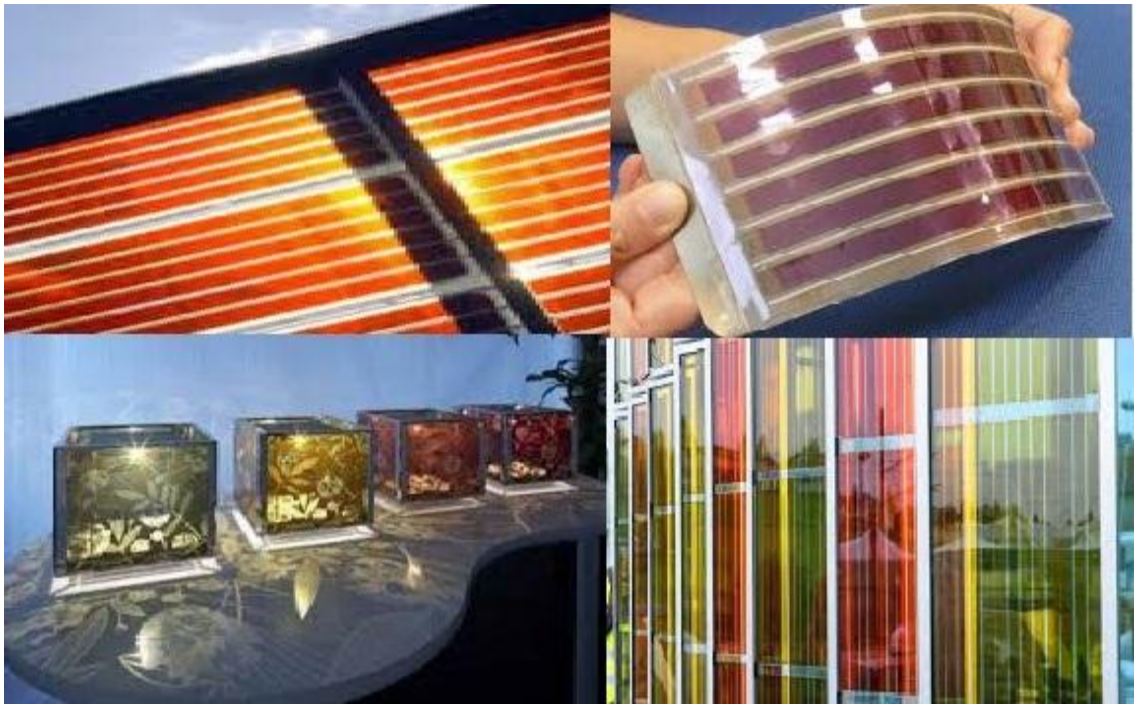

Figure 2: Various examples of commercialized DSSCs

Acknowledgement

One of the authors is thankful to CSIR-India for the financial support in the form of Research Associate.

References

1. Hamakawa Y (2002): Solar PV energy conversion 21st century's civilization. *Sol. Ener. Mater. Sol. Cells*, 74, 13.
2. Renewable Global Status Report: Update 2012. Renewable Energy Policy Network for the 21st Century, Paris.
3. PV Status report, JRC European Commission, (2011).
4. Schiermeier Q, J. Tollefson, T. Scully, A. Witze and O. Morton (2008): Energy alternatives: Electricity without Carbon. *Nature,* 454, 816.
5. Gratzel M. Photoelectrochemical cells. *Nature* 2001; 414:338-344.
6. Gratzel M. Solar energy conversion by dye sensitized photovoltaic cells. *Inorg Chem* 2005; 44: 6841-6851.
7. Cho S, Sung HK, Lee SJ, Kim WH, Kim DH, Han YS. Photovoltaic performance of dye sensitized solar cells containing ZnO microrods. *Nanomaterials* 2019; 9: 1645.
8. Tripathi M, Cahwla P. Renewable energy in the service of Mankind II 2016: 377-384.
9. R. Upadhyay, M. Tripathi, P. Chawla and A. Pandey, "Performance of CeO_2- TiO_2 admixed photoelectrode for natural dye sensitized solar cell," *J. Solid State Electrochem.* **18**, 1889-1892 (2014).
10. J.Y. Park, C.S. Kim, K. Okuyama and H.M. Lee, "Copper and nitrogen doping on TiO_2 photoelectrodes and their functions in dye sensitized solar cells," *J. Power Sou.* **306** 764-771 (2016).
11. P. Chawla and M. Tripathi, "Novel improvements in the sensitizers of dye sensitized solar cells for enhancement in efficiency- A review," *Int. J. Ene. Res.* **39** (12), 1579-1596 (2015).
12. M.A.M Al-Alwani, H.A. Hasan, N.K.N. Al-Shorangi and A.B.S.A. Al-Mashaan, "Natural dye extracted from Areca catechu fruits as a new sensitizer for dye sensitized solar cell fabrication: Optimization using D-Optimal design," *Mater. Chem. Phys.* **240** (15), 122204 (2020).
13. N.Y. Amogne, D.W. Ayele and Y.A. Tsigie "Recent advances in anthocyanin dyes extracted from plants for dye sensitized solar cell," *Mater. Renew. Sustain. Ene.* **9**, 23 (2020).

14. C.O. Ogabi, B.A. Idowu, A.O. Boyo, S.O. Oseni and R.O. Kesinro "Simulation and Performance of Natural Sensitizer Dye from Lagerstroemia speciosa Flowers and Leaves," *J. Mat. Sci. Res. Rev.* **7**(1), 60-65 (2021).
15. P. Chawla and M. Tripathi, "Nanocomposite polymer electrolyte for enhancement in stability of betacyanin dye sensitized solar cells," *ECS Solid State Lett.* **4** (2015) 21-23.
16. M. Kokkonen et al., "Advanced research trends in dye-sensitized solar cells," *J. Mater. Chem. A.* **9**, 10527-10545 (2021).
17. S. Ketabi and K. Lian, "Effect of SiO_2 on conductivity and structural properties of PEO-$EMIHSO_4$ polymer electrolyte and enabled solid electrochemical capacitors,"*Electrochim. Acta.* **103**, 174-178 (2013).
18. S. Venkatesan, P. Liu, L.T. Chen, Y. C. Hou, C.W. Li and Y. L. Lee, "Effects of TiO_2 and TiC nanofillers on the performance of dye sensitized solar cells based on the polymer gel electrolyte of a cobalt redox system," *ACS Appl. Mater. Interfaces,* **8**, 24559-24566 (2016).
19. Yan Q, Chang ML, Bao SJ, Bao QL (2007) Carbon nanotube/polyaniline composite as anode material for microbial fuel cells. J Power Sources 170: 79-84.
20. Chen BK, Chang S, Li DY, Chen LL, Wang YT, Chen T, Zou BS, Zhong HZ, Rogach AL (2015) Template synthesis of CuInS2 nanocrystals from In2S3 nanoplates and their application as counter electrodes in dye-sensitized solar cells. Chem Mater 27:5949-5956.

Chapter: 18

Prism based refractometer

Priyanka Srivastava

Institute of Engineering & Technology, Dr RLAvadh University, Ayodhya

E-mail: priyanka.srivastava73@gmail.com

Abstract: Refractive index is a fundamental property of substance which indicates that how fast light can pass through the substance. It is very important for optical instruments and can also judge the purity or measure the concentration of a substance. The device that can measure the refractive index of liquid or solids is known as refractometer. It has wide application for quality control especially in pharmaceuticals and beverages industries.

A highly sensitive refractometer, able to measure the refractive index of liquid phase ambient is discussed here. It's a prism based refractometer which gives very high sensitivity when light falls over the prism ambient interface at an angle very close to the critical angle. The design is highly sensitive, robust, and user friendly.

Keywords: refractive index, critical angle

Introduction

Refractive index is an important characteristic of optical materials. It has wide application in characterizing substances. In fact, using this parameter we can check the presence of impurities in various liquids. Refractive index is a fundamental constant and we all are aware of its velocity and angle dependency by Snell's law[1]. The instrument used to measure or sense the refractive index of a substance is termed as refractometer. Several types of refractometers are available and are widely used in various industries like drug manufacturing, food processing, beverages and sugar industry.

Bali et al.[2,3] have proposed a prism base liquid sensing refractometer giving small intensity modulation for small refractive index variation of ambient liquid. The new configuration

presented here shows large variation in intensity for small change in refractive index leading to a significant increase in the sensitivity of the refractometer.

Types of Refractometers

Refractometers can be classified in four categories depending on their sensing techniques

1. Optical refractometer based on measurement of critical angle or deviation angle[4]
2. Optical refractometer based on interferometric methods and Brewster angle method
3. Optoelectronic Refractometer
4. Fibre optical Refractometer

Mostly the conventional refractometers like Abbe, Pulfrich, Hilger Chance refractometers are based on the first category. The most popular refractometer is Abbe's refractometer which is based on measurement of critical angle. A precision Immersion refractometer is also used for refractive index measurement of liquids with higher accuracy. The Baush and Lamb immersion refractometer is provided with six interchangeable prisms to cover wide sensing range. In all these refractometers based on critical angle the eyepiece crosswire has to be set on a demarcation line separating bright and dark areas. Asymmetrical nature of this setting may cause reduction in accuracy. The optoelectronic version of refractometer uses an array of pixels to determine the direction of light beam. Fibre optical sensors depend on measurement of intensity modulation or phase modulation. Another modern version of automatic refractometer compares refractive index of continuous flow sample with that of a reference liquid. It gives electrical output proportional to difference in r.i.

Interferometric refractometer falling under category 2 are easily influenced by air turbulence. Fringe counting becomes ambiguous in this case, leading to a decrease in the resolution. Refractometer based on total internal reflection and heterodyne interferometry has also been reported. Most of this refractometer have the disadvantage of moving parts and are manually operated and so they cannot be used in the condition of high temperature, radiation hazards etc. For such situation remote sensing of refractive index with optoelectronic type is required. A refractometer sensor using fibre optic transducer has also been reported with high sensitivity. But

this device also has highly fragile structure and sensitive to contamination. Its cleaning cycle is also very cumbersome.

The optoelectronic refractometer described here is free from manually operated limitations and also is able to remote sensing.

Principle of operation

The ratio of intensity of reflected light to that of unpolarised incident beam is given by the equation

$$\frac{I_r}{I_i} = \frac{1}{2}\left[\frac{\sin^2(\theta_i - \theta_t)}{\sin^2(\theta_i + \theta_t)} + \frac{\tan^2(\theta_i - \theta_t)}{\tan^2(\theta_i + \theta_t)}\right]$$

$$\frac{\sin\theta_i}{\sin\theta_t} = \frac{\mu_a}{\mu_g}$$

To illustrate the principle of operation for the refractometer configuration under investigation we plot I_r / I_i against with the help of above equations (Fig.1), for μ_g = 1.5 35 with $\Theta = 68.5^0$ (curve X) and with $\Theta = 45^0$ (curve Y) . It clearly shows that the total internal reflection occurs for all values of μ_a from point a to b and that point b correspond to the critical angle of incidence. If the angle of incidence is now kept fix at this angle $\Theta = 68.5^0$ and r.i. of the ambient μ_a is allowed to increase beyond μ_{ac} then I_r / I_i decreases sharply at first(b to c), slowly afterwards (c to d), going ultimately to zero at $\mu_a = \mu_g$ =1.535(point e). Thereafter I_r / I_i starts increasing as μ_a increases beyond μ_g (e to f).

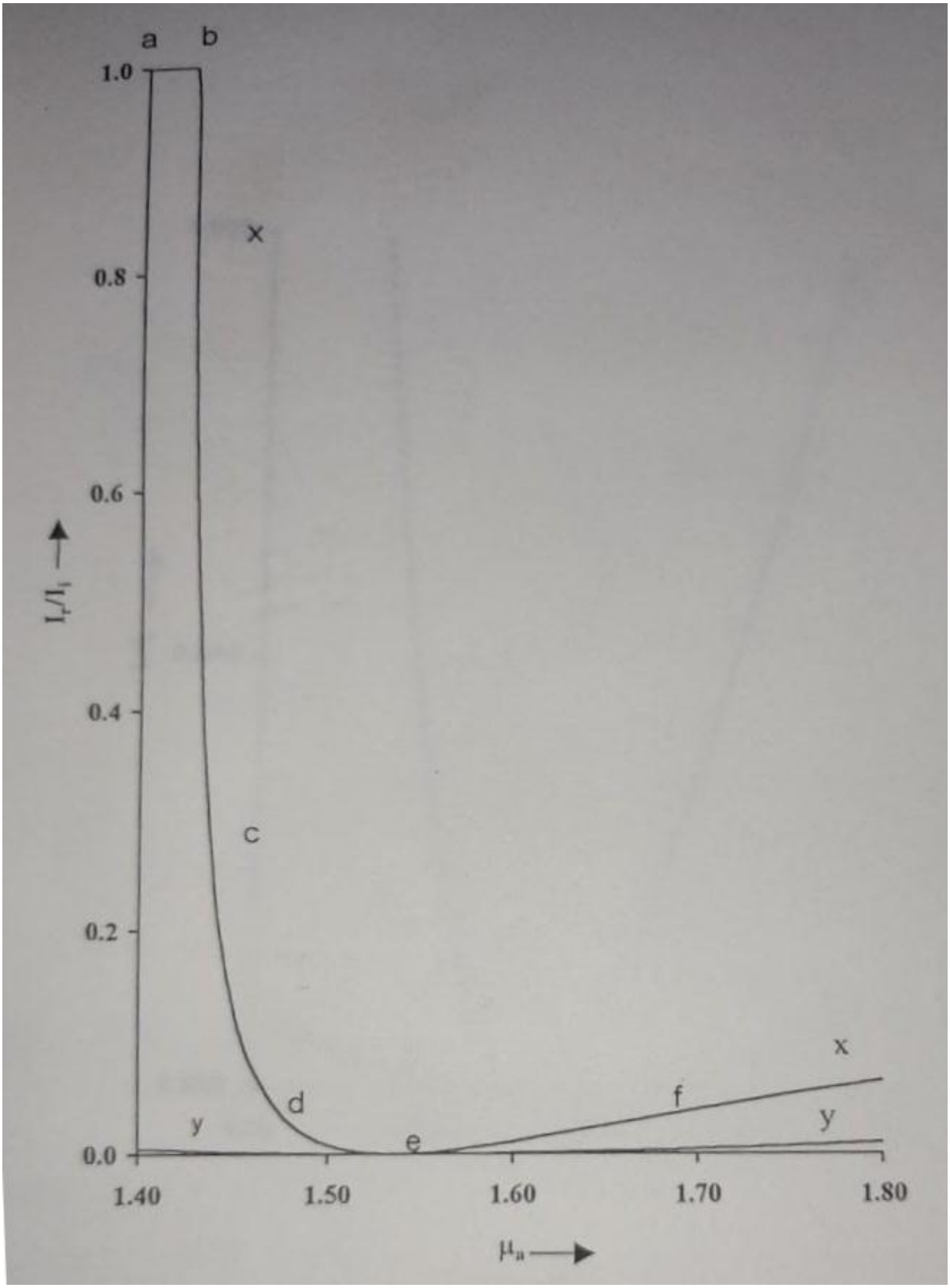

Figure: 1

The curve X plotted for $\Theta = 68.5^0$ is found to show regions of large modulation (b to c), whereas no such large modulation region is coming with $\Theta = 45^0$ in this entire r.i. range (curve Y).

Refractometer can therefore be fabricated using different angles of incidence for a given value of μ_g, to give larger or smaller modulation in intensity for a given range of values of μ_a. The sensitivity S of the refractometer, providing a measure for these modulations may now be defined as the change in I_r / I_i to change in μ_a.

Experimental setup and working

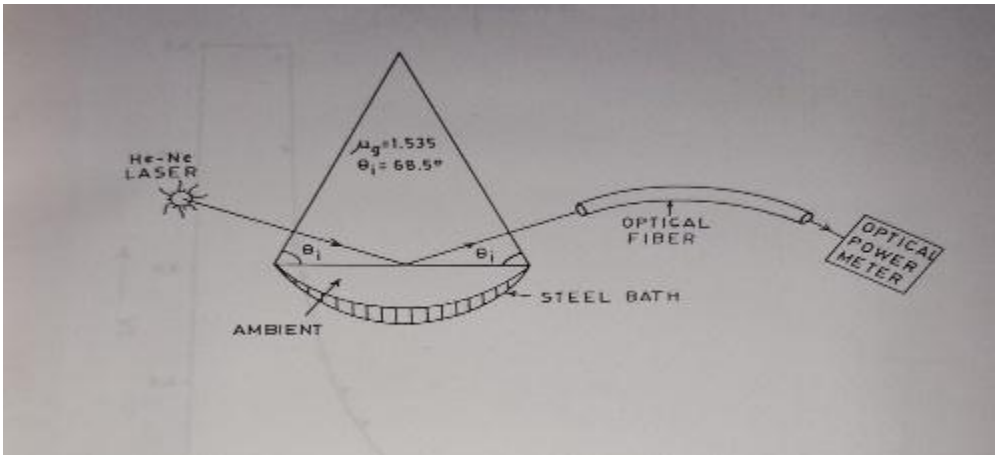

Figure: 2

Figure 2 describe the experimental setup. The experiment was carried out at room temperature. Which was maintained at 29^0C.The beam of light from 5mw He-Ne laser entering normally through one of the isosceles faces of the prism is incident on the μ_g - μ_a interface at the same angle 68.5^0 as its base angle. The reflected light emerging out of the other isosceles face of this prism is collected through an optical fibre and fed into an optical power metre. Reflected light intensity I_r is measured in this experiment as r.i. of the ambient is varied over the limited range of μ_a, a portion corresponding to segment bc of curve x of Fig.1 from 1.426 to 1.467 by mixing glycerol (r.i.= 1.473) in water (r.i.=1.333) is obtained (Fig.3). Glycerol is chosen for this mixing because it is easily soluble in water and does not react with it, and also because it enables the refractive index of the mixture to be continuously varied over the entire refractive index range under investigation. It may be noted that for the configuration under investigation TIR takes place when the ambient is either air or water. For this intensity can therefore be taken to be the

same as the observed value of I_r. The r.i. of the ambient has been determined with the help of Abbe's refractometer.

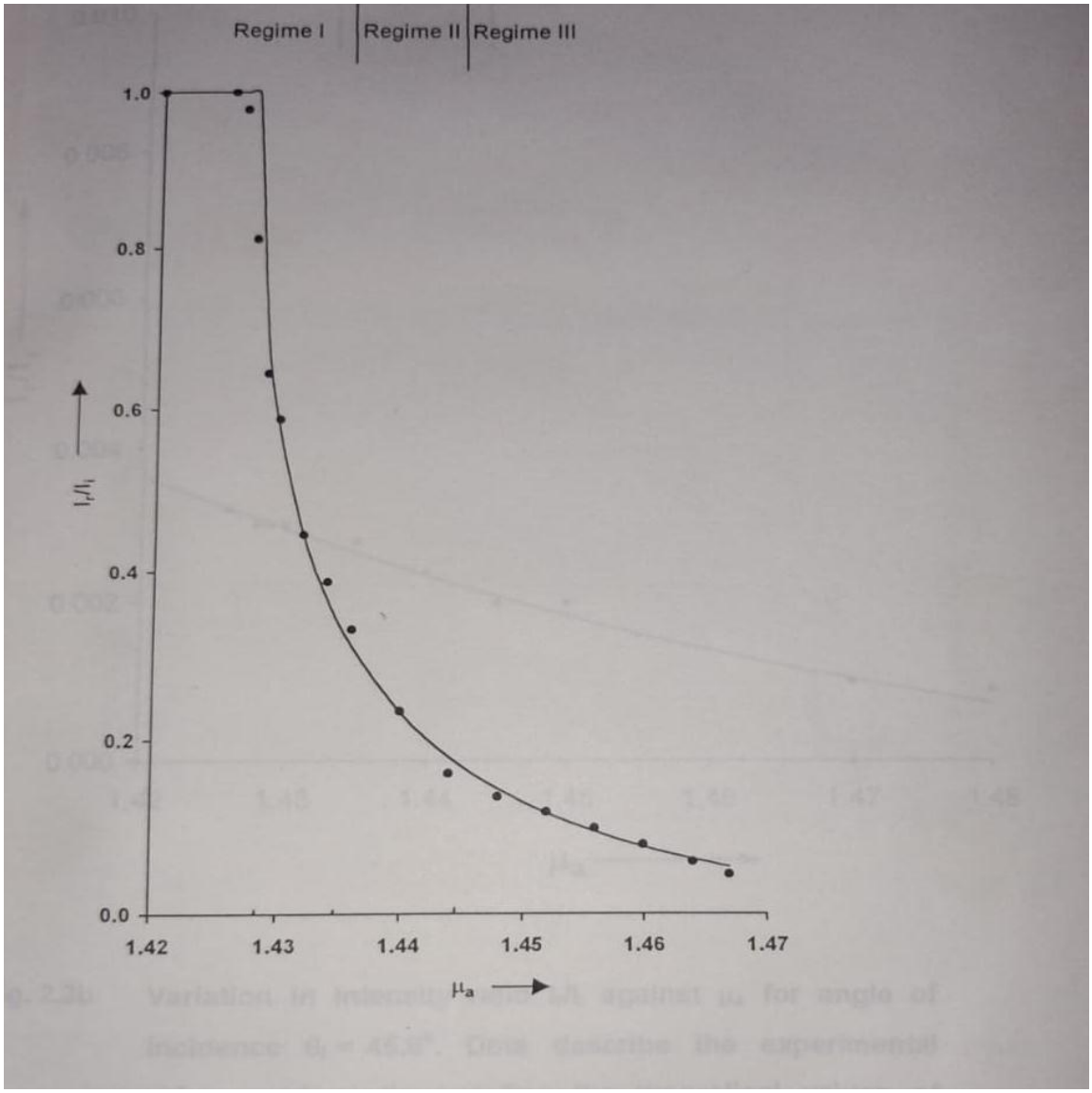

Figure: 3

Conclusion

Therefore, if the angle of incidence of the light rays could be varied in the small steps over a large range of angles, then the range of continuous values of μ_a for which this refractometer continues to remain highly sensitive would be highly enlarged. But, the mechanical precision is required to monitor these small changes in the angles of incidence.

References

1. Max Born and Emil Wolf, Principles of optics. Pergamon Press Ltd.,Oxford, 7th edition (**1999**)
2. L.M.Bali, Atul Srivastava, R.K.Shukla, Anchal Srivastava, Opt.Engg.38, 1715 (**1999**)
3. Atul Srivastava, R.K.Shukla, Anchal Srivastava and L.M.Bali, Optical sensors…,Photonics 98,989-992
4. R.S.Longhurst, Geometrical and physical Optics, 3rd edition (**1973**)

Editors

Prof. R.K. Shukla is Professor in Department of Physics at University of Lucknow, Lucknow. He has published more than 200 research paper in prestigious international journals. His research interests focus on Free Electron Laser, Fiber Optics Sensors and Material Science. He has supervised several Ph.D. Thesis in the field of Material Science and Sensors. Prof. Shukla has earlier authored several books like Mechanics, Optics, Quantum Mechanics, Fiber Optics, Practical Physics etc. Prof. Shukla has two Patents on Refractometer Sensor to his credit. He has established Thin and Thick films laboratory in his Department. He also participated and delivered his talk in number National and International Conferences. He has successfully completed major research Projects funded by DST, Govt. of India and UGC, New Delhi.

Dr. Bhuvan Bhasker Srivastava, Associate Professor & Head, Department of Physics, Shia P.G. College, Lucknow, (An Associated College of University of Lucknow) Sitapur Road, Lucknow, UP, India. He has authored 02 Text Book for UG and PG Students. He is famous for applying various innovative methods of teaching physics. He has published several research papers in prestigious international journals. He has organised many Conference, FDP and Workshop with Collaboration of National and International Institutes. He has delivered several Invited talk and presented his research work in various National and International Conference. Dr. Srivastava is Life Time Member of Indian Science Congress, Indian Association of Physics Teachers (IAPT), Material Research Society of India (MRSI). Dr.Srivastava has got award "Pratibhagita samman" and appreciation letter from Prashikshan evam Sewayojan Nideshalay, Lucknow, UP. He has recognised by various News paper like “Dainik Jagran” published a news on its cover page under the Headlines of “BLACK SE WHITE KI AUR” in connection with his teaching style on 05/09/2011 and I-Next published a news on its cover page under the headlines of “CITY KE RANCHO”&“NAHI BANANA HAI CHATUR” in connection with his Teaching on 17/01/2010.

Dr. Susheel.Kumar Singh obtained his B.Sc. from University of Allahabad, Allahabad. He completed his M.Sc. in Electronics as well as M.Sc. in Physics from University of Lucknow, Lucknow. He awarded his doctorate in Physics from University of Lucknow.Currently he is serving as Assistant Professor, Department of Physics at HLY PG College, Associated to University of Lucknow, Lucknow. He has authored 03 text book for UG and PG Students and 02 Edited Book. He has published more than 20 research paper in prestigious international journals. He has organised more than 20 Conference, FDP and Workshop with Collaboration of National and International Institutes. Dr. Singh is General Secretary of prestigious Educational Society named by MKSES Educational Society Lucknow, UP, India. He has great research passion in the area of Material Science. Dr. Singh participated and presented his research work in many National and International Conferences.

MKSES PUBLICATIONS
LUCKNOW, INDIA

Address: Head office: 1st Floor, Building No-85A,
(Nanak Arcade, Hind Nagar LDA Colony,
Kanpur Road, Lucknow–226012
Mobile No: +919838298016
office Land line No: +91 5223587193
E-mail:mkespublication@gmail.com
Website: mkesublications.com

ISBN-978-93-91248-18-5

PRICE
INR 300/
USD 10/

Available on
Book available at amazon
Flipkart